https://lib.uliege.be https://matheo.uliege.be

Finite Element modeling of geomechanical processes in longwall mining

Auteur : Hanna, Jamil
Promoteur(s) : François, Bertrand
Faculté : Faculté des Sciences appliquées
Diplôme : Master en ingénieur civil des constructions, à finalité spécialisée en "civil engineering"
Année académique : 2024-2025
URI/URL : http://hdl.handle.net/2268.2/22415

Avertissement à l'attention des usagers :

Tous les documents placés en accès ouvert sur le site le site MatheO sont protégés par le droit d'auteur. Conformément aux principes énoncés par la "Budapest Open Access Initiative"(BOAI, 2002), l'utilisateur du site peut lire, télécharger, copier, transmettre, imprimer, chercher ou faire un lien vers le texte intégral de ces documents, les disséquer pour les indexer, s'en servir de données pour un logiciel, ou s'en servir à toute autre fin légale (ou prévue par la réglementation relative au droit d'auteur). Toute utilisation du document à des fins commerciales est strictement interdite.

Par ailleurs, l'utilisateur s'engage à respecter les droits moraux de l'auteur, principalement le droit à l'intégrité de l'oeuvre et le droit de paternité et ce dans toute utilisation que l'utilisateur entreprend. Ainsi, à titre d'exemple, lorsqu'il reproduira un document par extrait ou dans son intégralité, l'utilisateur citera de manière complète les sources telles que mentionnées ci-dessus. Toute utilisation non explicitement autorisée ci-avant (telle que par exemple, la modification du document ou son résumé) nécessite l'autorisation préalable et expresse des auteurs ou de leurs ayants droit.

University of Liège

Faculty of Applied Sciences

Finite Element modeling of geomechanical processes in longwall mining

Master thesis completed by:

Hanna Jamil

In order to obtain the degree of Master of Science in Civil Engineering

Membres du jury

Bertrand FRANCOIS (ULiege, Promoteur)
Frédéric COLLIN (ULiege)
Ioan BOTI (UTCB)
Pascal GODERNIAUX (UMons)

Master Civil Engineering

2024-2025

Abstract

Longwall mining, a method first implemented in the 1920s, has seen significant advancements in recent years with the development of more powerful excavation tools and automated support systems. This research investigates the geomechanical behavior of goafs, the voids created during the longwall mining process, focusing on their potential for repurposing as geothermal energy storage spaces. The study utilizes finite element modeling (FEM) to simulate the displacement, stress distribution of both the goaf and the surrounding intact rock. On that base porosity and permeability evolutions in the goaf are predicted. The modeling approach incorporates elastic and elasto-plastic material properties, with a particular emphasis on plastic compressibility, using the LAGAmine software.

The modeling of reference case provides some insights on the geomechanical behavior of longwall mining including the goaf and the surrounding rock. Then the research builds on a real-world case from the Belgian Mining Basin, focusing on understanding the hydraulic properties of rock environments within and near the exploited areas. Four key parameters (the plastic compressibility factor (β), the lateral boundary conditions, the depth of the goaf, the bulking factor b) are analyzed for their sensitivity in affecting the representation of reality and the results of the simulations. The findings indicate that the geomechanical characteristics of the goaf, such as its porosity and permeability, play a crucial role in determining its suitability for geothermal energy storage applications.

This study offers valuable insights into the behavior of goafs, showing that with proper modeling, previously mined-out areas could be transformed into valuable assets for sustainable energy storage. The results of this research advance the understanding of how geomechanical processes impact the stability and usability of goafs and highlight their potential for integration into renewable energy systems.

Résumé

L'exploitation minière par longue taille, une méthode mise en œuvre pour la première fois dans les années 1920, a connu des avancées significatives ces dernières années avec le développement d'outils d'excavation plus puissants et de systèmes de support automatisés. Cette recherche étudie le comportement géomécanique des zones foudroyées, c'est-à-dire les vides créés pendant le processus d'exploitation minière par longue taille, en se concentrant sur leur potentiel de réutilisation comme espaces de stockage d'énergie géothermique. L'étude utilise la modélisation par éléments finis (FEM) pour simuler le déplacement et la distribution des contraintes à la fois des zones foudroyées et de la roche intacte environnante. Sur cette base, les évolutions de porosité et de perméabilité dans la zone foudroyée sont prédites. L'approche de modélisation intègre les propriétés des matériaux élastiques et élastoplastiques, avec un accent particulier sur la compressibilité plastique, en utilisant le logiciel LAGAmine.

La modélisation du cas de référence fournit des informations sur le comportement géomécanique de l'exploitation minière par longue taille, y compris la zone foudroyée et la roche environnante. Ensuite, la recherche s'appuie sur un cas réel du bassin minier belge, en se concentrant sur la compréhension des propriétés hydrauliques de la roche à l'intérieur et à proximité des zones exploitées. L'effet de quatre paramètres clés (le facteur de compressibilité plastique (β), les conditions aux limites latérales, la profondeur de la zone foudroyée, le facteur de foisonnement b) sont analysés. Les résultats indiquent que les caractéristiques géomécaniques de la zone foudroyée, telles que sa porosité et sa perméabilité, jouent un rôle crucial dans la détermination de son adéquation aux applications de stockage d'énergie géothermique.

Cette étude offre des informations précieuses sur le comportement des zones foudroyées, montrant qu'avec une modélisation appropriée, des zones précédemment exploitées pourraient être transformées en actifs précieux pour le stockage d'énergie durable. Les résultats de cette recherche font progresser la compréhension de la manière dont les processus géomécaniques affectent la stabilité et l'utilisabilité des zones foudroyées et mettent en évidence leur potentiel d'intégration dans les systèmes d'énergie renouvelable.

Acknowledgement

I would like to express my deepest gratitude to my thesis advisor, Professor François Bertrand, for their invaluable guidance, support, and encouragement throughout the course of my research. Their expertise and dedication were essential in helping me navigate the complexities of this thesis, and I truly appreciate their time and effort.

I would also like to extend my heartfelt thanks to all the professors at the University of Liège for their continuous support and for fostering an environment of learning and growth. Their academic contributions and teachings have been fundamental in shaping my understanding of civil engineering principles.

Additionally, I would like to acknowledge the professors at the Technical University of Civil Engineering Bucharest (UTCB) for their insightful advice and constructive feedback during my studies, particularly Professor Ioan Boti, whose help was invaluable throughout my time at UTCB.

A special thank you to the Erasmus office for giving me the opportunity to follow the double degree program, which has been a rewarding and enriching experience.

Lastly, I would like to express special thanks to my mother, who has always been by my side, inspiring me throughout my life and always believing in me; to my father, who has been a constant source of support; and to my sister, who was always there for me. I am also deeply grateful to my friends, especially Rayan and Marwa, and to all my other friends for their unwavering support, encouragement, and belief in me throughout this journey. Their presence has meant the world to me.

Contents

1 Introduction

Longwall mining, though first implemented as early as the 1920s, has become increasingly significant in recent years due to advancements in powerful excavation tools and automated support systems, enhancing its efficiency and ability to maximize resource recovery. Unlike other mining techniques, longwall mining involves the extraction of coal in a continuous, full-face manner, creating large cavities, or goafs, as the mining progresses. The geomechanical behavior of these goafs, including their displacement, stress distribution, porosity, and permeability, plays a critical role in assessing the long-term stability of the mined areas and their potential for secondary uses, such as geothermal energy storage. Understanding these geomechanical processes is essential not only for optimizing mining operations but also for exploring innovative ways to repurpose mined-out spaces for sustainable energy solutions.

The central focus of this research is the finite element modeling of the geomechanical processes involved in longwall mining. Through the use of finite element simulations, this study aims to investigate the displacement and stress distribution within the rock mass during the mining process and analyze the geomechanical properties of the goaf that are essential for energy storage applications. In particular, the study explores the relationship between porosity and permeability and how these factors influence the suitability of the goaf for storing water or gas, which could potentially be used for geothermal energy applications.

This study builds on both theoretical modeling and a real-world case study from a mining site in Belgium. The real case involved a detailed examination of the displacements and stresses experienced by the rock mass, alongside the evaluation of the porosity and permeability of the goaf. At this stage, in the absence of in-situ characterization of the studied longwall mining site, the results are exclusively blind predictions based on the expected properties of the rock. These parameters are crucial for understanding the potential for utilizing the goaf as a storage space for geothermal energy. The finite element modeling approach enables a comprehensive analysis of the geomechanical behavior of the rock mass, allowing for the simulation of various mining conditions and their impact on the stability of the goaf.

The primary research question guiding this work is: How can finite element modeling be used to simulate the geomechanical processes of longwall mining and assess the potential of the goaf for energy storage applications? To answer this question, the study employs a combination of numerical simulations and field data analysis to provide a detailed understanding of the displacement, stress, porosity, and permeability characteristics of the goaf. This research contributes to the growing body of knowledge on longwall mining by demonstrating how geomechanical modeling can be used to evaluate not only the mechanical stability of mined-out areas but also their potential for future use in sustainable energy storage.

2 State of the Art: Geomechanical Challenges in Longwall Mining

2.1 Overview of Coal Mining

2.1.1 Introduction

Coal mining is the procedure of removing coal, an important power supply from the dirt. It has been the foundation of industrial development and energy production for hundreds of years. There are mainly two ways to mine coal: surface mining and underground mining. Surface mining is for relatively shallow deposits where the overburden is removed to expose the coal seam, while underground mining is necessary for deeper deposits, which employs room-and-pillar and longwall mining. Since coal is essential to fuel industries and provide energy for electricity all over the world, an increased need for effective mining processes combined with safe extraction practices have meant that we have set our eyes on proper management based direction. Being the oldest method with implications to land degradation, groundwater contamination and subsidence, coal mining, therefore has Menchian aspects of a geomechanical as well as enviro-geological issue which needs to be encountered strategically in for an intact production landscape.

2.1.2 Mining Technologies: Room-and-Pillar vs. Longwall Mining

Underground mining technologies primarily fall into two categories: room-and-pillar mining and longwall mining. These methods take quite different approaches to resource extraction, support systems, and geomechanical implications.

Room-and-Pillar Mining: One of the oldest mining techniques, room-and-pillar mining involves the creation of ”rooms” in the coal seam, with unmined ”pillars” left behind to support the roof. . This approach is effective for shallow coal resources, but its efficacy decreases with greater mining depths. The need for larger and more robust pillars at greater depths reduces the amount of recoverable coal, making the method less efficient than longwall mining . The pillars are engineered according to geotechnical factors, with their dimensions generally dictated by the seam's depth and the surrounding rock's strength. Room-and-pillar mining is considered a cyclic process, wherein rooms are sequentially mined and the roof is supported using roof bolts. . This approach, historically utilized for millennia, is progressively being supplanted by contemporary procedures like longwall mining, attributable to its worse recovery rates.The mining process in room-and-pillar mining is shown in Figure 1.

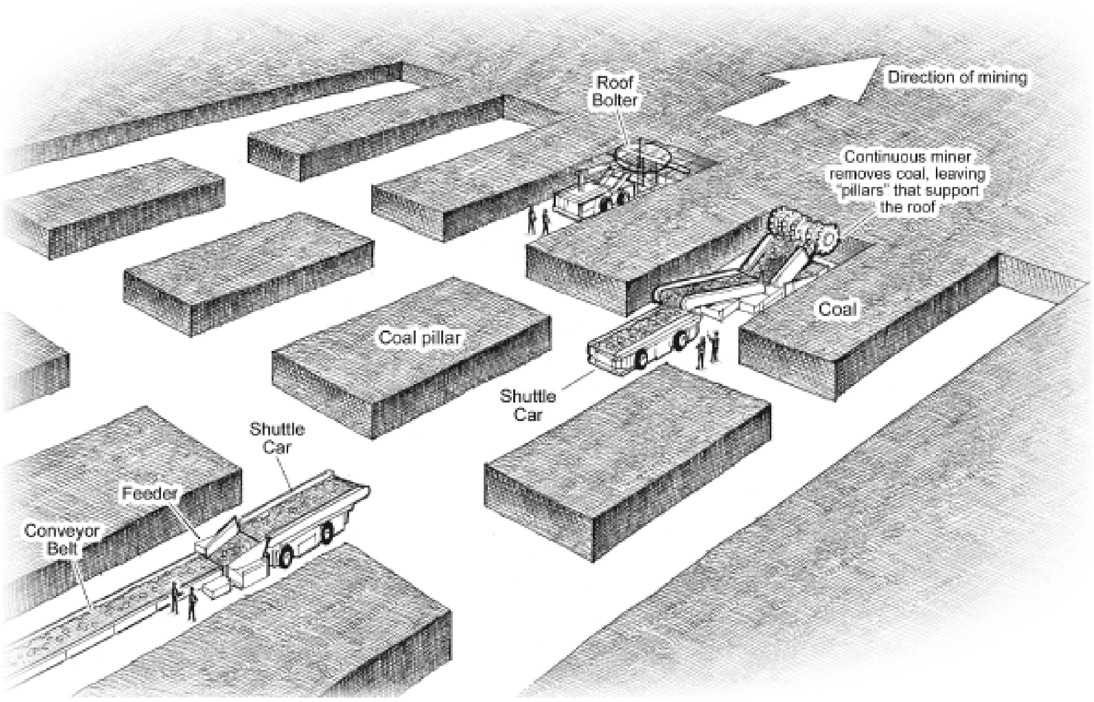

Figure 1: Room and pillar mining (Arch Coal Inc., 2010).[1]

Longwall Mining: In contrast, Longwall mining has become the leading method for efficiently extracting coal from underground seams, using highly mechanized processes and equipment. It allows large and contiguous coal panels, with panel widths up to 260 m, lengths up to 2,000 m, and heights of up to 2.5 m [27]. This approach relies on several key components: roof-support shields, shearers, armored face conveyors, beam stage loaders, and additional service equipment critical to its operation. Along the coal face, hydraulically operated roof-support shields (Figure 2) temporarily hold the roof in place to prevent collapse. As operations progress, a shearer equipped with dual cutting heads mines the coal by moving up and down the coal face, extracting the full height of the seam with a cut width ranging from 0.76 to 1.07 m [25]. The mined coal is loaded onto a conveyor system, which is driven by motorized sprockets at both the main and tail gates, ensuring seamless transport to the surface.

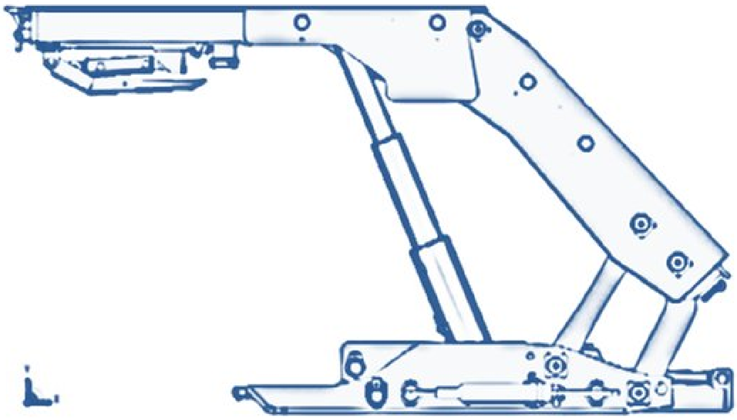

Figure 2: Basic parts of a powered roof support. The image shows a typical lemniscate shield. [15]

As the face advances, the supports move forward, allowing the roof behind to collapse in a controlled manner into the mined-out area, known as the goaf (Figure 3). This technique minimizes the need for pillars, as the roof is systematically allowed to collapse. The systematic collapse and high extraction rates, up to 90%, make longwall mining indispensable for flat-lying seams, particularly in deep mines. In 2013, global coal production exceeded 7,823 million tonnes, with approximately 60% mined underground, and longwall mining played a significant role in achieving this output.

Despite its advantages, such as high productivity and nearly complete coal recovery, longwall mining presents considerable geomechanical challenges, including roof control, ground displacement, and subsidence. Addressing these challenges is crucial to ensuring the safety and efficiency of modern underground coal operations [17].

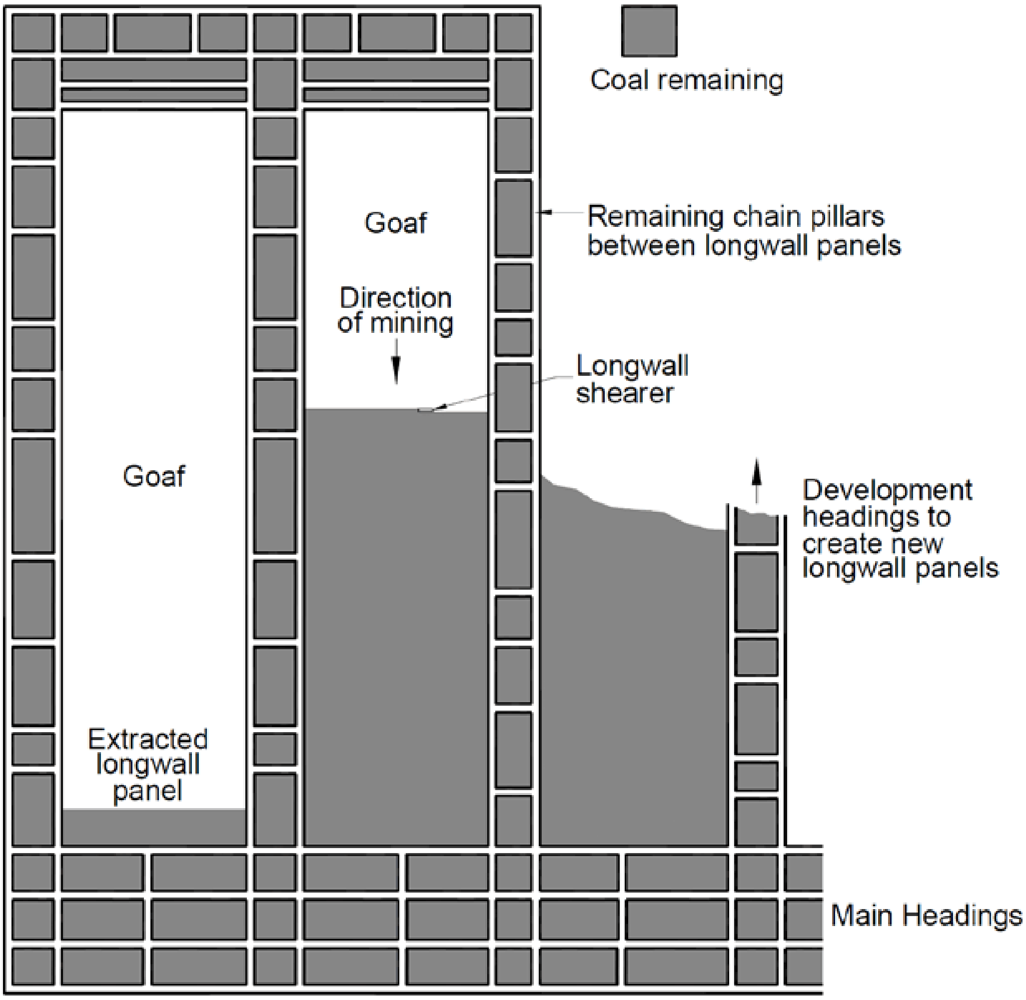

Figure 3: Typical plan view of longwall panels (MSEC, 2007).[19]

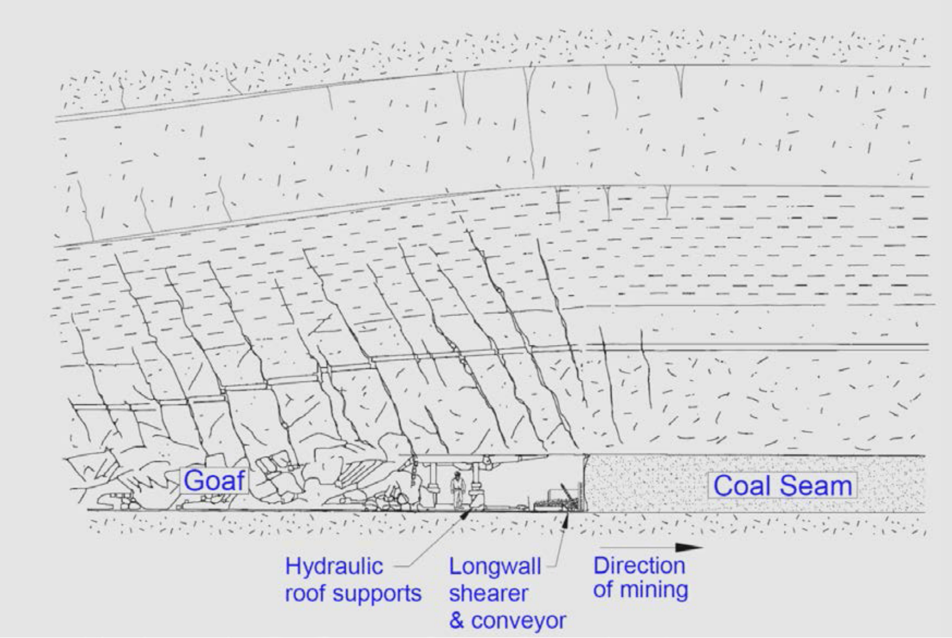

Figure 4: Typical cross section of longwall face (MSEC, 2007).[19]

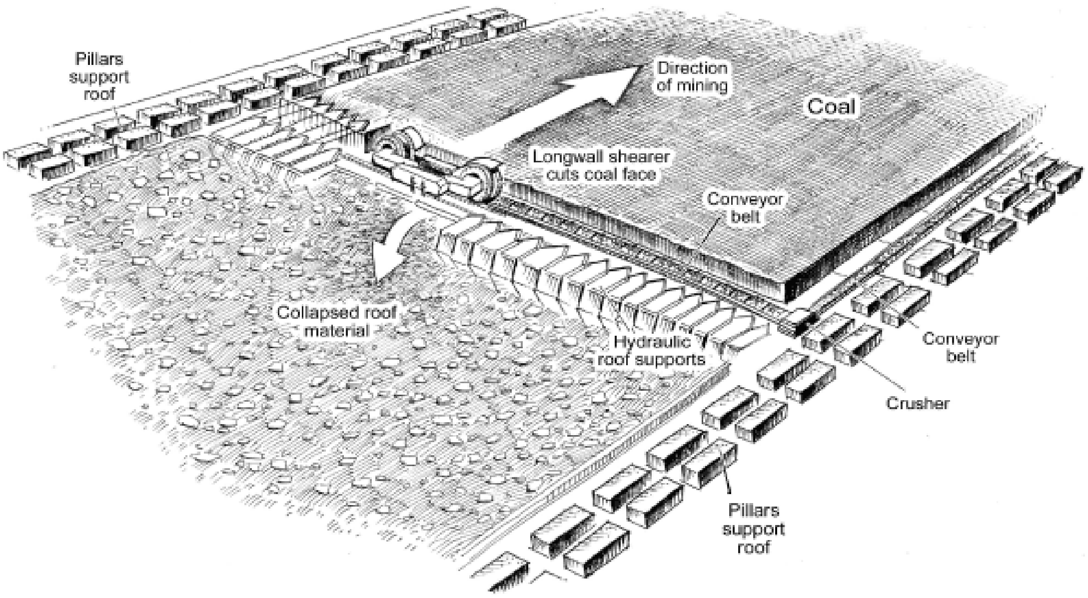

Figure 5: Longwall mining (Arch Coal Inc., 2010).[1]

2.1.3 Geomechanical Challenges in Longwall Mining

Longwall mining introduces dramatic changes to the stress regime of the surrounding rock mass. The extraction of coal causes stress redistribution and roof collapse behind the mining face, resulting in various geomechanical problems. Effective ground control is essential to maintaining the stability of the mine and preventing hazardous conditions such as roof falls, subsidence, and rockbursts.

Stress Redistribution: The most immediate geomechanical challenge in longwall mining is the redistribution of in-situ stresses as coal is removed from the seam. As the mining face advances, the overburden begins to subside, creating significant vertical and horizontal stress concentrations in the surrounding rock [25]. Vertical stress tends to peak just ahead of the mining face, where the abutment pressure builds up as the roof is unsupported (Figures 6, 7). This abutment pressure, or peak stress, can be several times higher than the original in-situ stress, making it a critical consideration in mine design [24]. Horizontal stresses, which are redistributed around the mine, can cause deformation in the gate roads and pillars, further complicating mine stability.

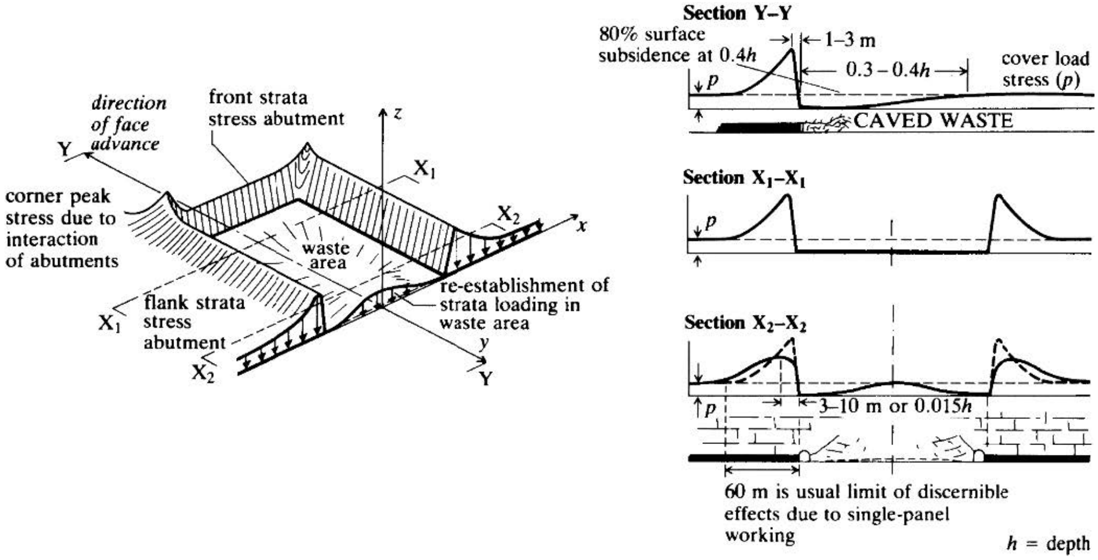

Figure 6: Vertical stress redistribution in the plane of the seam around a longwall coal face (after Whittaker,1974).[3]

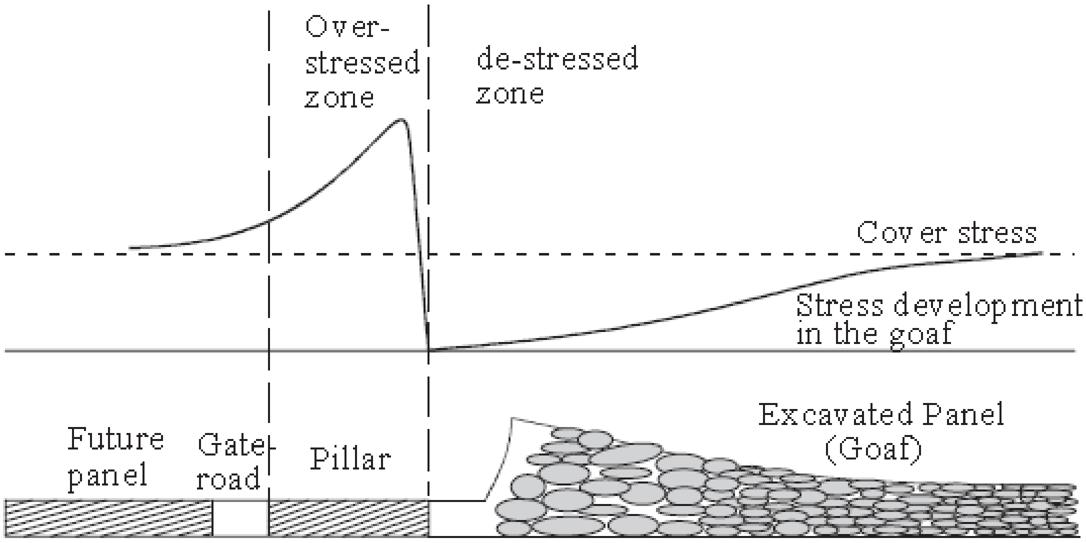

Figure 7: Stress state in the ground after the excavation of a panel.[28]

Underground Rock Deformation: The collapse of the roof behind the longwall face, known as the goaf, leads to significant deformation in the overlying rock layers. This deformation occurs in three distinct zones: the caving zone, the fractured zone, and the continuous deformation zone [24] (Figure 8).

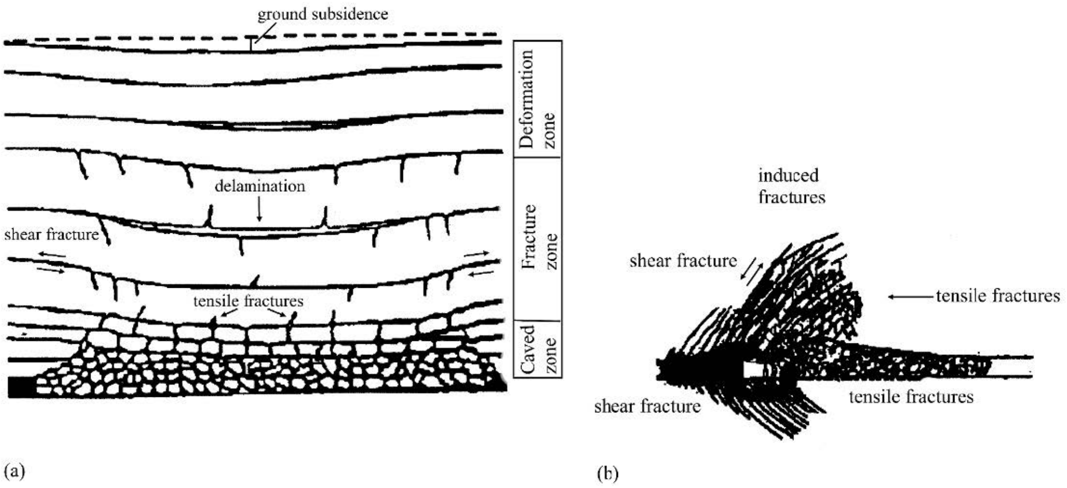

Figure 8: Rock fracture and displacement pattern near the face of a longwall coal mining panel: (a) section transverse to the panel axis; (b) longitudinal section. [24], [18]

In the immediate caving zone, rock layers collapse into the void left by the mined-out coal. This zone can extend to a thickness of two to eight times the mining height, depending on the strength of the overburden. Above the caving zone is the fractured zone, where rock layers are heavily fractured and lose their cohesion due to the removal of support (In this thesis, the goaf is assumed to exhibit an elastoplastic response, while the intact rock is considered to have a purely elastic response.). Finally, the continuous deformation zone, which reaches up to the surface, experiences plastic deformation rather than complete fracturing.

Roof Falls and Control: Roof falls present one of the most significant hazards in longwall mining operations. Rock failure occurs when the stress applied to the roof strata exceeds the strength of the rock mass. Horizontal stress, roof thickness, and material properties play pivotal roles in determining the likelihood of roof falls [25]. Weak roofs, composed of shale or other soft rocks, are particularly prone to failure under stress, while stronger roofs, such as those made of sandstone, are more resistant. Roof control is achieved through the use of powered supports (Figure 2), which temporarily hold up the roof as the face advances [25]. These supports are designed to withstand the dynamic loads created by roof collapses, redistributing the stress to prevent sudden failure. Barczak (1992) [26] distinguished four categories of roof fall mechanisms according to Figure 9

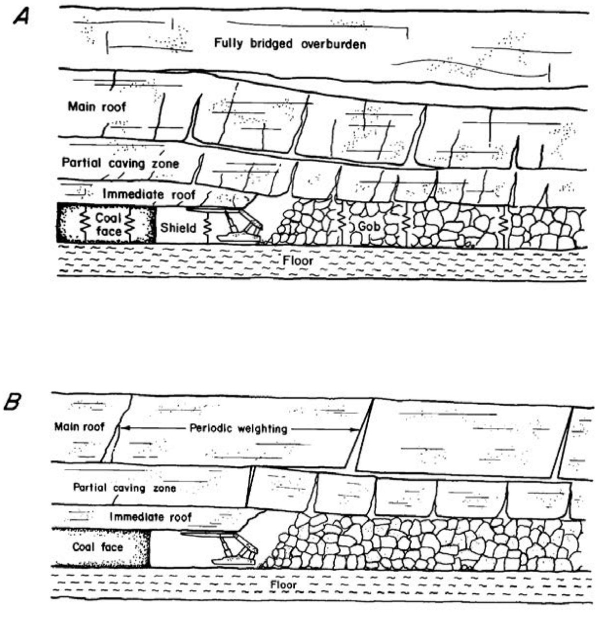

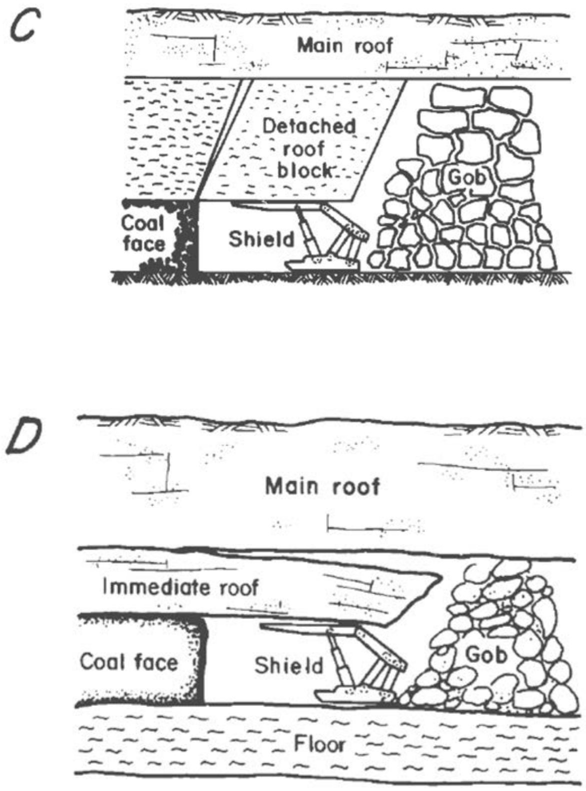

Figure 9: Different types of roof fall. A – Main roof convergence. B – Periodic weighting. C – Detached immediate roof. D – Deflection of immediate roof. [26]

2.1.4 Surface Subsidence and Environmental Impact

A significant effect of longwall mining is surface subsidence, the steady descent of the ground as the above layers fall into the excavated panels. This subsidence can have profound environmental and infrastructural impacts, including the alteration of surface topography, the disruption of groundwater flow, and the formation of sinkholes and cracks . In certain instances, subsidence may lead to significant surface deformations, resulting in troughs above excavated regions.

The magnitude of surface subsidence depends on several factors, including the size of the longwall panels, the depth of mining, and the geotechnical properties of the overburden. Subsidence generally commences soon after mining operations initiate and persists until the overburden achieves stabilization. Numerical models are often used to predict subsidence patterns, allowing for proactive measures to be taken to protect surface infrastructure and water resources [25]. Nonetheless, despite progress in predictive modeling, subsidence continues to be a significant concern in longwall mining, especially in areas with delicate surface ecosystems. The following Figures 10, 11, 12 demonstrate how the deformation process happen.

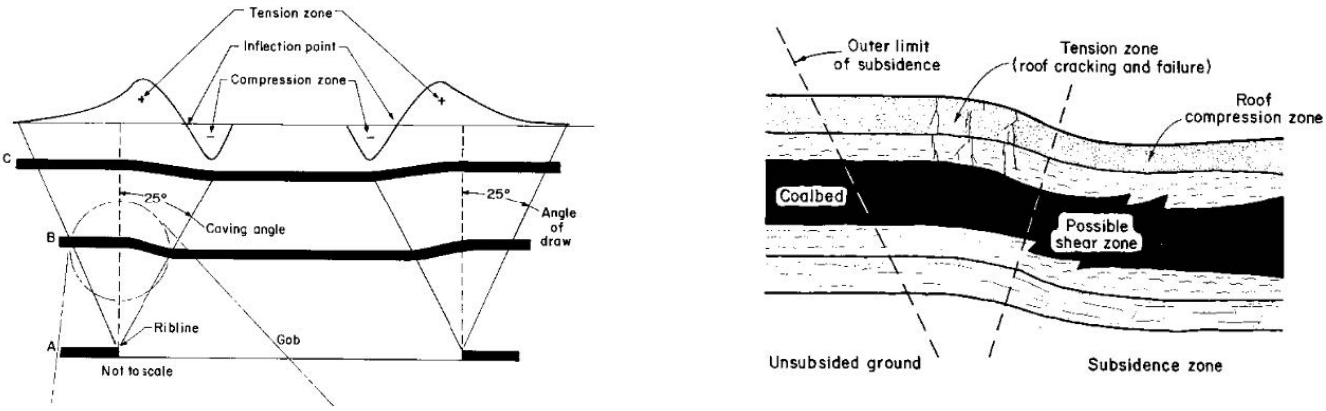

Figure 10: Formation of a subsidence trough above a mined-out panel (Haycocks et al., 1982) [5].

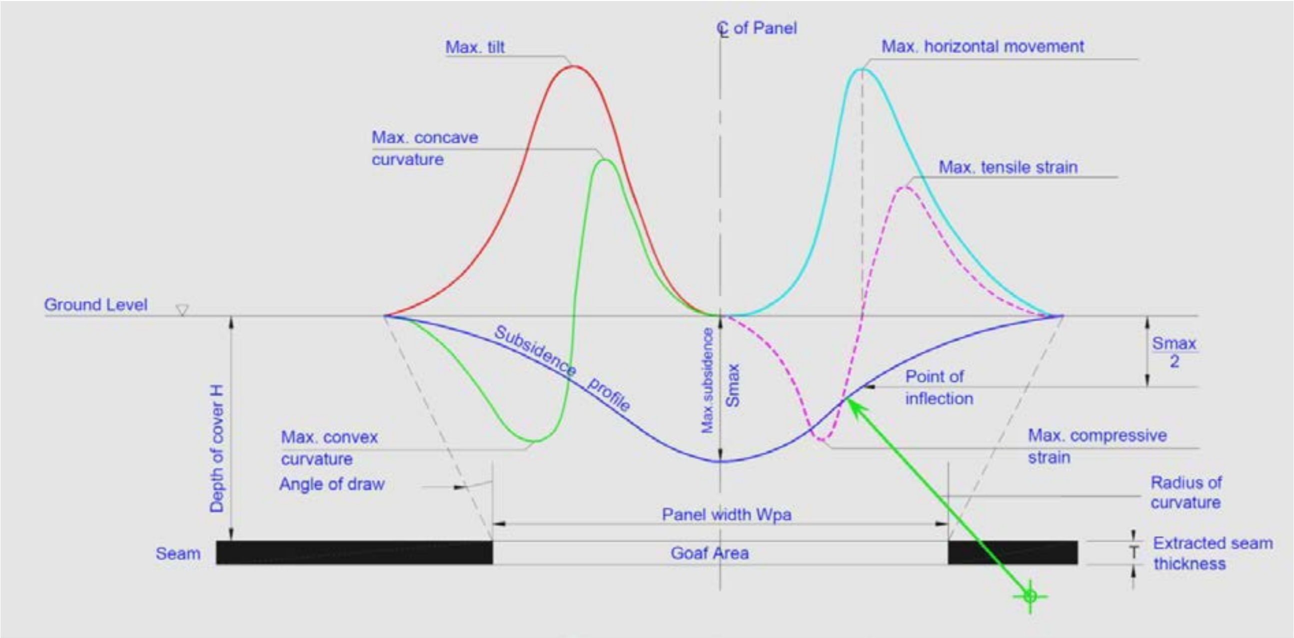

Figure 11: Detailed geodetic characterization of subsidence trough above a mined-out panel (MSEC, 2007) [19]

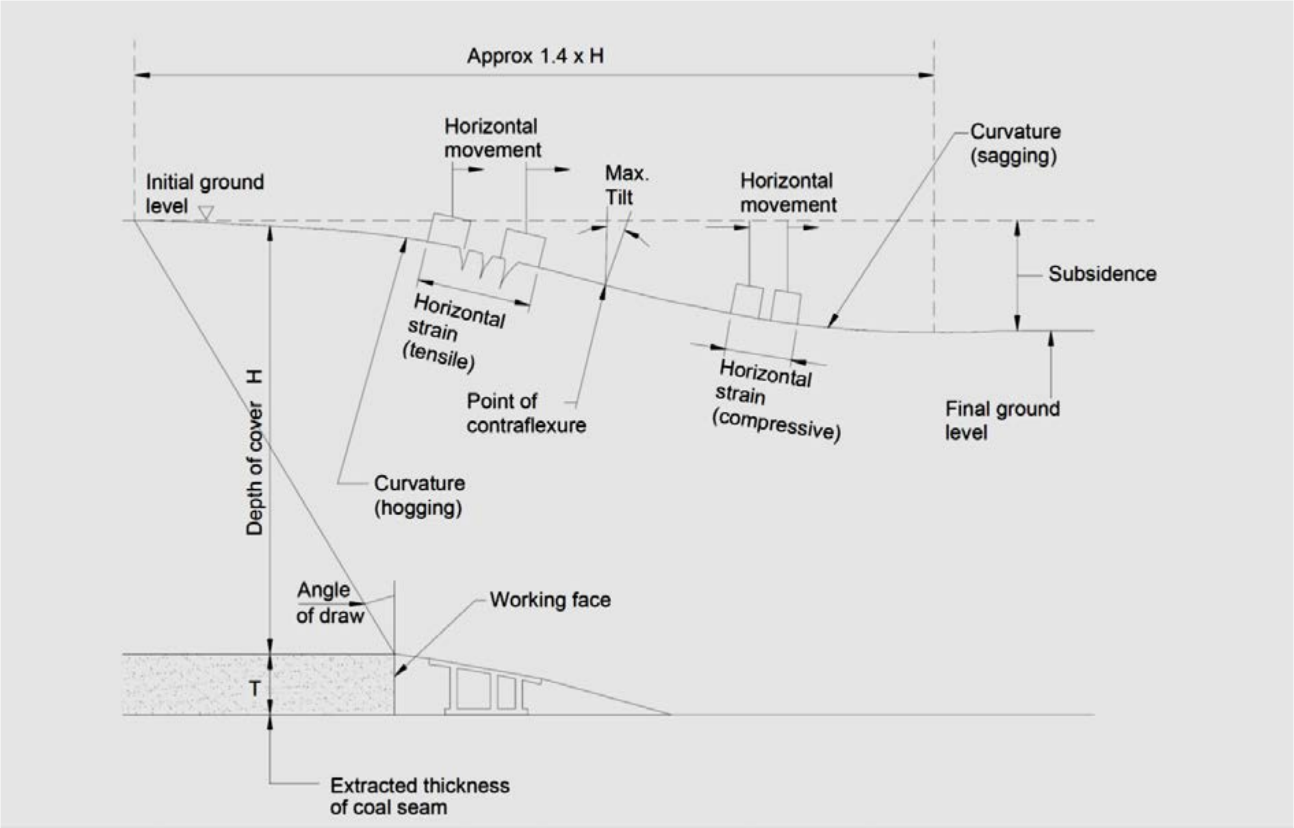

Figure 12: Development of subsidence trough above longwall mining area (MSEC, 2007) [19]

2.1.5 Powered Supports in Longwall Mining

In longwall mining, powered supports are the primary mechanisms of controlling the roof as the face move forward. These supports, also known as shields, play a vital role in preventing roof collapse by holding up the overlying strata until the coal is extracted. Once the coal has been removed, the shields are advanced forward, allowing the roof behind to collapse into the goaf.

Types of Supports: Modern powered supports consist of hydraulic legs, a steel canopy, and a base plate. The canopy bears the load of the roof, while the hydraulic legs provide the pressure needed to maintain this support. The supports are designed to accommodate the dynamic loading conditions present in longwall mining, with pressure adjusted as the face advances [25]. There are several different types of shields, including frame, chock, and lemniscate shields, each with specific design features tailored to different mining conditions. Lemniscate shields are the most common type used today, due to their compact size and high load-bearing capacity [25].

Shield Performance: The performance of powered supports is determined by their ability to resist the forces exerted by the collapsing roof. This is measured in terms of setting load (the initial load applied by the shield) and yield load (the maximum load the shield can withstand before failure). Proper selection and positioning of powered supports are essential to maintaining the stability of the mine and preventing catastrophic roof collapses [24]. Numerical simulations and physical models are often used to assess the interaction between supports and the surrounding rock mass, providing insights into optimal support design and placement [24].

2.1.6 Rockburst Hazards in Longwall Mining

Rockbursts, sudden and violent failures of the rock mass, are a significant hazard in longwall mining, particularly in deep mines with high-stress conditions. These events are caused by the release of strain energy stored in the rock, often triggered by mining operations that alter the stress regime [9]. Rockbursts can cause serious damage to mine infrastructure and pose a major safety risk to miners.

To mitigate the risk of rockbursts, several techniques are employed, including de-stress blasting, water injection, and the mining of safety seams [22]. De-stress blasting involves the controlled explosion of rock to release stored strain energy before it builds up to dangerous levels. Safety seams, mined above or below the main coal seam, act as a buffer, redistributing stress and reducing the likelihood of rockbursts [9].

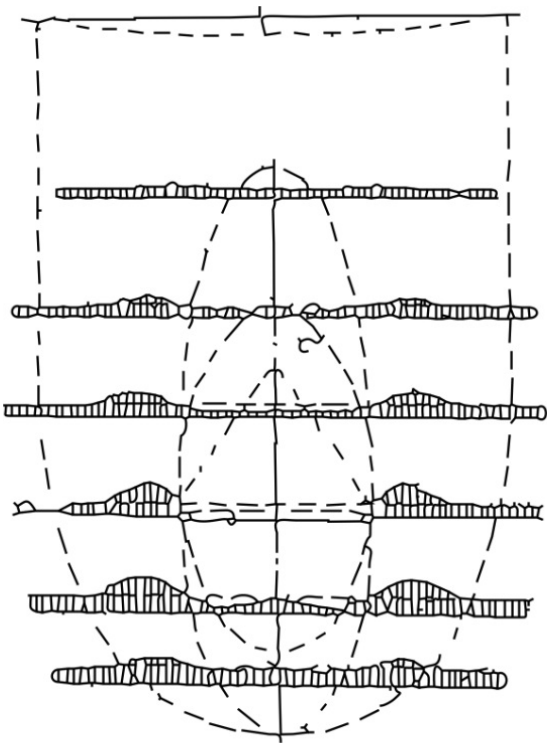

Figure 13: Zone of influence during longwall mining (c – area of reduced stress level suitable to mine rockburst pruned seam) (Bräuner, 1992).[9]

2.2 Elastic Models in Geomechanics

2.2.1 Hooke's Law

The generalized form of Hooke's law establishes a relationship between stress and strain in elastic materials through elastic constants. Initially formulated as a simple proportional relationship between force and elongation for springs [7], it has since been extended to encompass the behavior of three-dimensional elastic solids. These elastic constants, which are material-specific, define the interaction between stress and strain in isotropic materials, providing a foundation for understanding their mechanical responses.

2.2.2 Elastic Constants overview

- **Young's modulus(E) :** It measures materials stiffness in response to uniaxial tension or compression .

$$\sigma_{xx} = E\varepsilon_{xx} \tag{1}$$

The Figure 14 is an example of an elastic bar subjected to tension, and this loading is called uniaxial tension. The lateral surfaces of the bar are traction free, and the ends are subjected to uniform stress σ_{xx} (assuming the x-axis is aligned with the bar). The stress σ_{xx} will cause the bar to elongate, which results in an extensional strain ϵ_{xx}. Observations show (for some materials) that ϵ_{xx} depends linearly on σ_{xx}. [7]

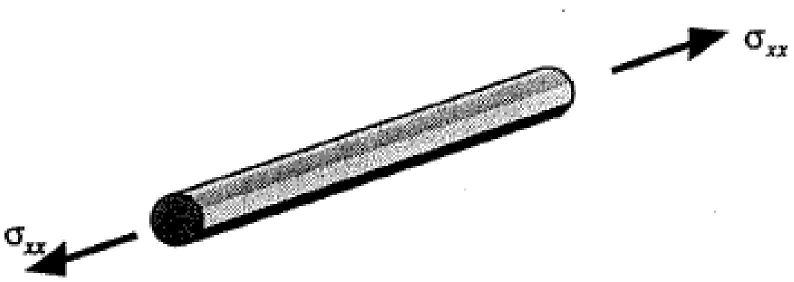

Figure 14: Elastic bar in uniaxial tension[7]

- **Poisson's ratio (ν) :** Describes the lateral contraction strain relative to the longitudinal strain in uniaxial tension.

$$\varepsilon_{yy} = \varepsilon_{zz} = -\nu\varepsilon_{xx} \tag{2}$$

We can also write

$$\varepsilon_{yy} = \varepsilon_{zz} = -\frac{\nu}{E}\sigma_{xx} \tag{3}$$

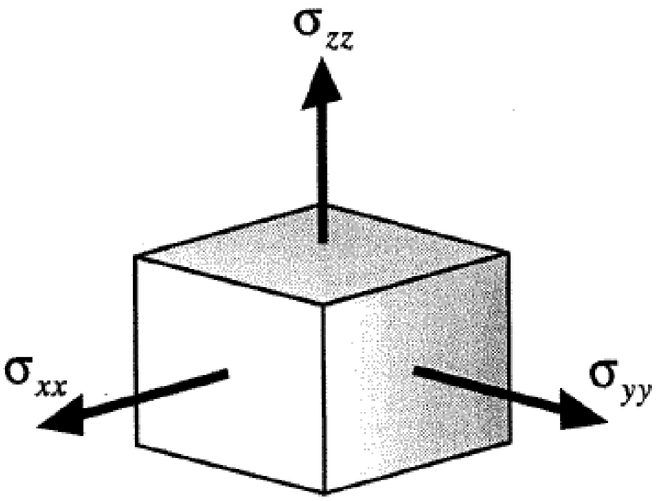

Figure 15: Elastic cube subjected to normal tractions. [7]

We can generalize these results by considering a cube of material subjected to uniform normal stress on all six faces as shown in Figure 15. The extensional strain ε_{xx} will depend on all three stresses. There will be a contribution from σ_{xx} exactly like eq. 1, but there will also be contributions from σ_{yy} and σ_{zz} similar to eq. 3. The resulting expression for ε_{xx}, ε_{yy} and ε_{zz} will be [7]

$$\epsilon_{xx} = \frac{1}{E}\left[\sigma_{xx} - \nu(\sigma_{yy} + \sigma_{zz})\right], \tag{4}$$

$$\epsilon_{yy} = \frac{1}{E}\left[\sigma_{yy} - \nu(\sigma_{xx} + \sigma_{zz})\right], \tag{5}$$

$$\epsilon_{zz} = \frac{1}{E}\left[\sigma_{zz} - \nu(\sigma_{xx} + \sigma_{yy})\right]. \tag{6}$$

- **Shear Modulus (G) :** Relates shear stress to shear strain. More specifically, G relates the off-diagonal terms σ and ε as follows [7]

$$\sigma_{xy} = 2G\epsilon_{xy}, \quad \sigma_{yz} = 2G\epsilon_{yz}, \quad \sigma_{zx} = 2G\epsilon_{zx} \tag{7}$$

The off-diagonal components ε, ε_{xy}, ...etc, represent one-half the actual shear strain. This is why the factor of 2 appears in these equations, making 7 consistent with the definition above. Also, the symmetry of both σ and ε shows us that only the three eqs. 7 are required to relate all the six shear stresses to the corresponding six shear strains. [7]

We need to continually bear in mind the assumption that our body is isotropic. If it were not, such simple relationships as eqs. 7 would not exist.

The relationship between the shear modulus (G), Young's modulus (E), and Poisson's ratio (ν)is given by the following equation :

$$G = \frac{E}{2(1+\nu)} \tag{8}$$

• **Bulk Modulus (K) :** Describes how a material responds to uniform pressure (volumetric strain).

$$K = \frac{E}{3(1-2\nu)} \tag{9}$$

Actually, E, K, and G have dimensions of stress while ν has no dimension.

• **Lamé Constants (λ) :** It has dimensions of stress and it is not based on a simple physical example. Instead, it arises more as a convenience in writing the normal stresses in terms of the normal strains. We can rearrange eqs. 6 and use eq. 8 to ultimatly find [7]

$$\begin{aligned} \sigma_{xx} &= \lambda e + 2G\epsilon_{xx} \\ \sigma_{yy} &= \lambda e + 2G\epsilon_{yy} \\ \sigma_{zz} &= \lambda e + 2G\epsilon_{zz} \end{aligned} \tag{10}$$

Where e is the volumetric strain and is given by the equation :

$$e = \epsilon_{xx} + \epsilon_{yy} + \epsilon_{zz} \tag{11}$$

$$= \frac{3p_0(1-2\nu)}{E} \tag{12}$$

And

$$\lambda = \frac{\nu E}{(1+\nu)(1-2\nu)} \tag{13}$$

Using eqs.7 and 10 we can now write generalized Hooke's law in another form, linking the matrices σ and ε

$$\sigma = \lambda e 1 + 2G\epsilon \tag{14}$$

Here 1 is the identity matrix.

2.3 The Drucker-Prager Plasticity Model

The Drucker-Prager yield criterion, introduced in 1952, is an adaptation of the von Mises criterion that incorporates mean stress sensitivity, making it particularly useful in modeling materials like soil and rock that exhibit both cohesive and frictional properties. Unlike the von Mises model, which assumes a purely cylindrical yield surface, the Drucker-Prager criterion introduces a cone-shaped yield surface. This conical form is obtained by modifying the yield condition to include a dependence on mean stress p, expressed in terms of the deviatoric stress q as:

$$q - \xi p = k \tag{15}$$

where ξ and k are material constants and can be calculated using the following equations :

$$k = \frac{6c\cos\phi}{3-\sin\phi}, \quad \xi = \frac{6\sin\phi}{3-\sin\phi} \tag{16}$$

These constants can be calibrated to approximate the yield behavior similar to that of the Mohr-Coulomb model, which is characterized by a hexagonal yield surface. By setting these parameters appropriately, the Drucker-Prager cone can be adjusted to either encompass or intersect the vertices of the Mohr-Coulomb hexagon [23].

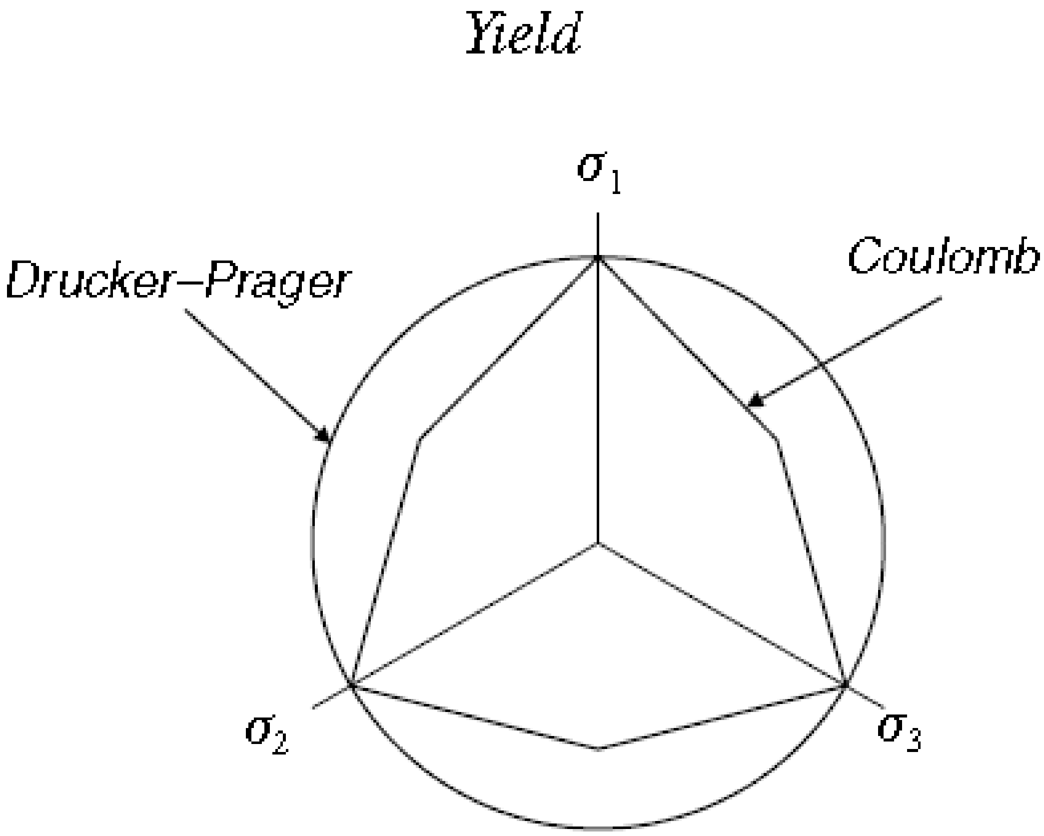

Figure 16: The Drucker–Prager and Coulomb yield surfaces.

The graph of the Drucker-Prager's yield surface in the π-plane is a circle that touches the Coulomb hexagon, as shown in Figure 16.

In practical application, the Drucker-Prager criterion simplifies calculations by avoiding the angular corners of the Mohr-Coulomb model, providing a smoother yield surface. This smoothness facilitates easier computational modeling in numerical simulations. However, one limitation is that it may not represent all soil behaviors with high precision, as experimental tests like triaxial tests often show that soil stress points align more closely with the edges of the Mohr-Coulomb hexagon than with the circular cross-section of the Drucker-Prager cone [23].

Several modifications to the Drucker-Prager model exist to improve its accuracy for specific soil conditions. For instance, smaller cone shapes have been proposed that intersect the Coulomb surface at the minor vertices rather than at the major vertices. This adaptation allows for a more accurate representation of materials that exhibit different failure behaviors under varying principal stress conditions.

The Drucker-Prager criterion is commonly used to define failure based on shearing mechanisms. However, it has limitations when it comes to representing the plastic contraction that occurs due to an increase in mean stress. This shortcoming arises because the criterion is focused solely on shear-induced failure and does not account for volumetric changes under isotropic loading. To overcome this limitation, it is essential to introduce an additional plastic mechanism that can capture the volumetric deformation induced by isotropic stress states as shown in figure 17 where f_{iso} is this additional plastic mechanism, while CSL (the oblique straight line starting for the origin of axis) correspond more or less to the Drucker-Prager criterion [2].

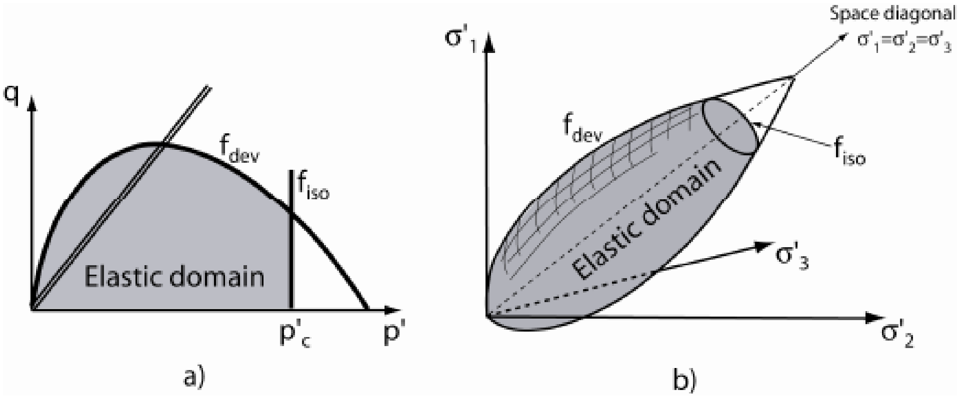

Figure 17: Yield locus of the elasto-plastic model including the plastic compressibility mechanism (f_{iso}) (a) View in the (p' - q) plane and (b) the principal stress space [13], [20], [2].

The volumetric response of soil under isotropic loading can be divided into two main parts: elastic compression and plastic contraction, both of which need to be adequately modeled to capture the soil's behavior accurately (Figure 18).

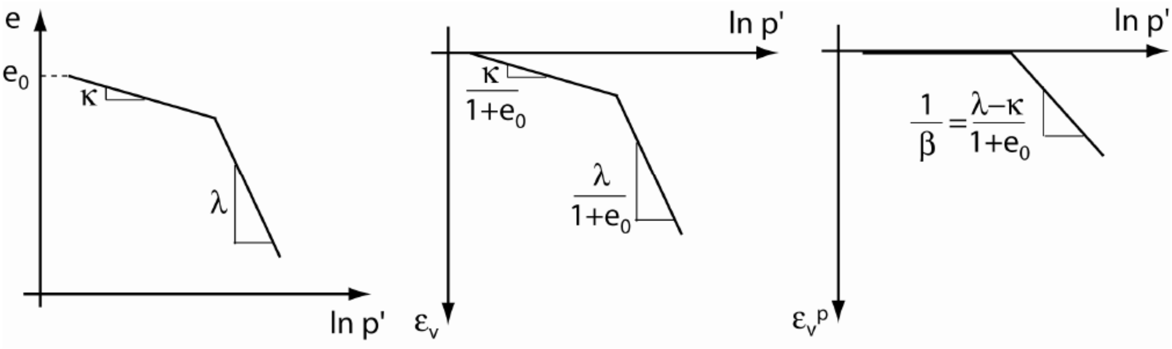

Figure 18: Schematic representation of the Cam-Clay prediction along an isotropic compression path: (a) $e - \ln(p')$; (b) $\epsilon_v - \ln(p')$; (c) $\epsilon_{vp} - \ln(p')$.[2]

(i) The behaviour inside the yield limit is governed by the loading-unloading curve (also called κ curve) which is characteristic of the isotropic elastic behaviour:

$$e = e_0 - \kappa \ln \frac{p'}{p'_0} \tag{17}$$

where e_0 is the initial void ratio, p'_0 is the initial mean effective stress, and κ, the swelling index, is a material parameter (the slope of the κ curve in the $(e - \ln p')$ plane).
(ii) On the isotropic yield criterion, a loading process induces both elastic and plastic evolutions of the void ratio following the normally consolidated line (also called λ curve or virgin compression line):

$$e = e_0 - \lambda \ln \frac{p'}{p'_0} \tag{18}$$

where λ , the compression index, is a material parameter (the slope of the λ curve in the $(e - \ln p')$ plane). The evolution of void ratio can easily be transformed into volumetric strain ϵ_v (contraction being positive):

$$\epsilon_v = \frac{e_0 - e}{1 + e_0} \tag{19}$$

In order to extract the plastic component of the total evolution of void ratio in Equation 18, the swelling index κ must be subtracted from the compression index λ , leading to the definition of the plastic compressibility (a material parameter):

$$\beta = \frac{1 + e_0}{\lambda - \kappa} \tag{20}$$

This parameter is used in the hardening equation, which describes the evolution of the critical pressure p'_{cr} with the generated volumetric plastic strain ϵ_v^e :

$$p'_{\mathrm{c}} = p'_{\mathrm{c0}} \cdot \exp(\beta \cdot \epsilon_v^p) \tag{21}$$

where p'_{c0} is the initial value of the preconsolidation pressure. Equation 18 is another way to express the evolution of the normally consolidation line (Equation 18). [2]

2.4 Porosity and Permeability in the Caving Zone of Longwall Goaf

In longwall mining, when coal is extracted, overburden strata enters into the goaf due to the caving of longwall goaf, it consists of broken coal and rock fragments. The forces from the overburden pressure compress these bits together, changing their porosity and permeability, impacting fluid movement, gas storage, and mining safety. These properties play an important role in hazard reduction and can be separated into four categories: methane emissions control, spontaneous combustion of leftover coal, water runoff, and drainage and mine stability optimization.

Porosity (the volume of voids in a material compared to the total volume) and permeability (the capacity of a porous material to transmit fluids) are interdependent and evolve as a function of the compaction state. Strain-based empirical relationships are commonly used to model permeability K. For example, according to Jozefowicz (1997) [14] proposed the following equation to describe permeability changes with volumetric strain.

$$K_g = -4 \times 10^{-16} \varepsilon_{\mathrm{vol}}^3 - 6 \times 10^{-15} \varepsilon_{\mathrm{vol}}^2 - 7 \times 10^{-14} \varepsilon_{\mathrm{vol}} + 10^{-11} \tag{22}$$

Where ε_{vol} is the volumetric strain and can be calculated as eq 23

$$\varepsilon_{vol} = \frac{\Delta\eta}{1 - \eta_0} \tag{23}$$

We calculate the change in porosity $\Delta\eta$

$$\Delta\eta = \epsilon_{vol}(1 - \eta_0) \tag{24}$$

And finial porosity eta_f is :

$$\eta_f = \eta_0 - \Delta_n \tag{25}$$

The formula 22, is based on experimental results, and has no supporting theoretical model. In addition, physical and mechanical properties of the coal and rock mass are not considered, so the scope for its application is limited.

Strain increases and permeability decreases non-linearly with compaction. An alternative well-known model of porous media is the Carman-Kozeny model equation that relates permeability with porosityη :

$$k = \frac{k_0}{Coeff} \left(\frac{\eta^3}{(1 - \eta)^2} \right) \tag{26}$$

with K_0 being the base permeability at maximum porosity and the Coeff is calculated as the following equation :

$$Coeff = \frac{\eta_0^3}{(1 - \eta_0)^2} \tag{27}$$

And η_o is initial priority and it equals the ratio between the voids volume and the total volume. The caving zone permeability reduction is often modeled using this equation as compaction progresses (Esterhuizen and Karacan, 2005) [8].

Directional variations in permeability due to an isotropic compaction can be expressed through fracture porosity and strain increments. Guo et al. (2009) [10] presented a permeability model:

$$k_{ii} = k_{ini}\left[1 + \beta_i \Delta\varepsilon_{jj} + \beta_k \Delta\varepsilon_{kk}\right] \tag{28}$$

where k_{ii} represents permeability in the i-direction, k_{ini} is the initial permeability, $\Delta\varepsilon$ are strain increments, and β coefficients are determined by material properties.

Laboratory experiments validate theoretical models and offer insights into how stress and material properties influence permeability. Permeability decreases exponentially with increasing stress σ, as represented by:

$$k = k_0 e^{-\alpha\sigma}, \tag{29}$$

where k_0 is the initial permeability, and α is a coefficient that depends on the material properties (Chen et al., 2015b) [6]. Additionally, the compaction of larger particles tends to retain higher permeability compared to smaller particles due to the larger voids they create.

The bulking factor, which measures the ratio of total volume to solid material volume, also plays a significant role. Experiments suggest that bulking varies with the fall height-to-block width ratio $h : b$, transitioning from fully caved rock with large voids to partially caved rock with reduced voids. Pappas and Mark (1993) [21] found the maximum bulking factor to be 1.85. This bulking directly affects porosity and, consequently, permeability, as described in:

$$b = \frac{V_r + V_v}{V_r}, \tag{30}$$

where b is the bulking factor, V_r is the rock volume, and V_v is the void volume.

The evolving properties of porosity and permeability in the caving zone are of significant importance for mining safety and efficiency. In the initial compaction stages, high permeability is favorable for the fluid, while vulnerable to introducing methane into the mining district. In contrast, decreased permeability in fully consolidated horizons may hinder the movement of gas and water, making drainage difficult. When theoretical models and their experimental counterparts, along with equations such as the Carman-Kozeny relationship are combined, accurate prediction of these properties is possible to guide the creation of appropriate drainage schemes and methane control methods.

2.5 Applications of Numerical Models in Longwall Mining

Longwall mining relies on numerical models, which are essential tools enabling engineers to model, analyze and optimize the mining. Here are some important applications of numerical models in longwall mining.

- **Ground Control and Stress Distribution Analysis**

Purpose: The initial analysis of the stress distribution within the rock mass surrounding excavation and mining's effect on stability roof and floor.

Application: Numerical models can be used to simulate the impact of stress propagation due to mining-induced stress on surrounding rock layers allowing engineers to predict possible failure zones, determine ground support system performance (e.g., tensioning) and design more reliable ground control strategies.

- **Subsidence Induced by Longwall Coal Mining**

Purpose: When longwall mining extracts coal, the strata above collapse into the mined area and

this is known as surface subsidence. It can impact infrastructure, water courses and ecosystems overlying the mine.
Application: Numerical models predicting the magnitude and extent of subsidence based on simulations of progressive collapse of overburden and redistributions of stresses. This enables engineers to counteract it, for instance, by changing the method or order of mining.

- **Reservoir Capacity Estimation**

Problem: Establishing the limit of gas that can be stored beneath ground level in a geological structure.
Numerical Modeling Use: Reservoir models derive the physical behavior of a reservoir such as porosity, permeability and pressure to estimate its storage capacity and isolate optimum injection and withdrawal cycles.

3 Methodology

3.1 Overview of LAGAmine Software

LAGAMINE is a finite element code born at the University of Liege at the end of the seventies. The code has been developed along with innovations and science for the last forty years. The continuous work of researchers around the world — in universities as well as in the industry — has maintained it at the leading edge of technology and research. More specifically, LAGAMINE is able to deal with complex nonlinear constitutive models, multi physical coupling, strain localization and multiscale approaches for applications in the fields of environmental geotechnics, engineering geology, reservoir engineering and metal forming[16].

3.2 Model Setup and Parameters

The problem studied is a rectangular model 106*100m , Due to the assumption that the goaf is very long in the direction perpendicular to the plane, the problem is treated as a two-dimensional plane strain problem. In this case, a 2D section in the middle of the goaf is isolated for analysis. Additionally, the left boundary can be considered as a symmetry axis, which implies that the modeled goaf represents half of the total length, with the other half mirrored on the other side of the symmetry. And for the modelling the fractured zone is not really considered because we have gone from caving zone to elastic zone. The goaf dimensions were 50*6m (as shown in the Figure 19),the 6-meter thickness of the goaf was based on the bulking factor b taken as 1.5. The relationship between the goaf thickness and the seam thickness is given by the equation:

$$H_{\text{goaf}} = \frac{H_{\text{seam}} \cdot b}{b-1} \tag{31}$$

In this case, 4 meters of intact rock (calculated as 6 meters minus 2 meters (the coal seam height)) collapse into 6 meters of goaf. Therefore, the bulking factor is calculated as:

$$b = \frac{6}{4} = 1.5$$

The points and the segments were defined in the software and the geometry is ready. The coal seam had the same properties of the rock.

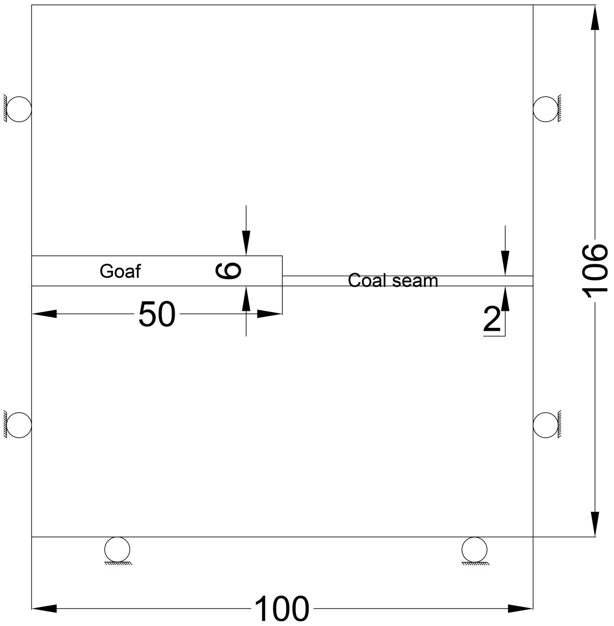

Figure 19: Constitutive models and boundary conditions of numerical goaf models.

The boundary conditions and the loads were defined, then the mesh was generated (Figure 20). The sub-program LAGALAW was used to define the constitutive laws and their associated parameters for the simulation. The numbers of the laws have been previously assigned while defining the contour. For all the cases we had 3 laws, the first one was to define the parameters of the rock, the second one was for the parameters of the goaf and the last one was for the parameters of the load (A detailed description of each law for all cases is provided in Section 3.3).

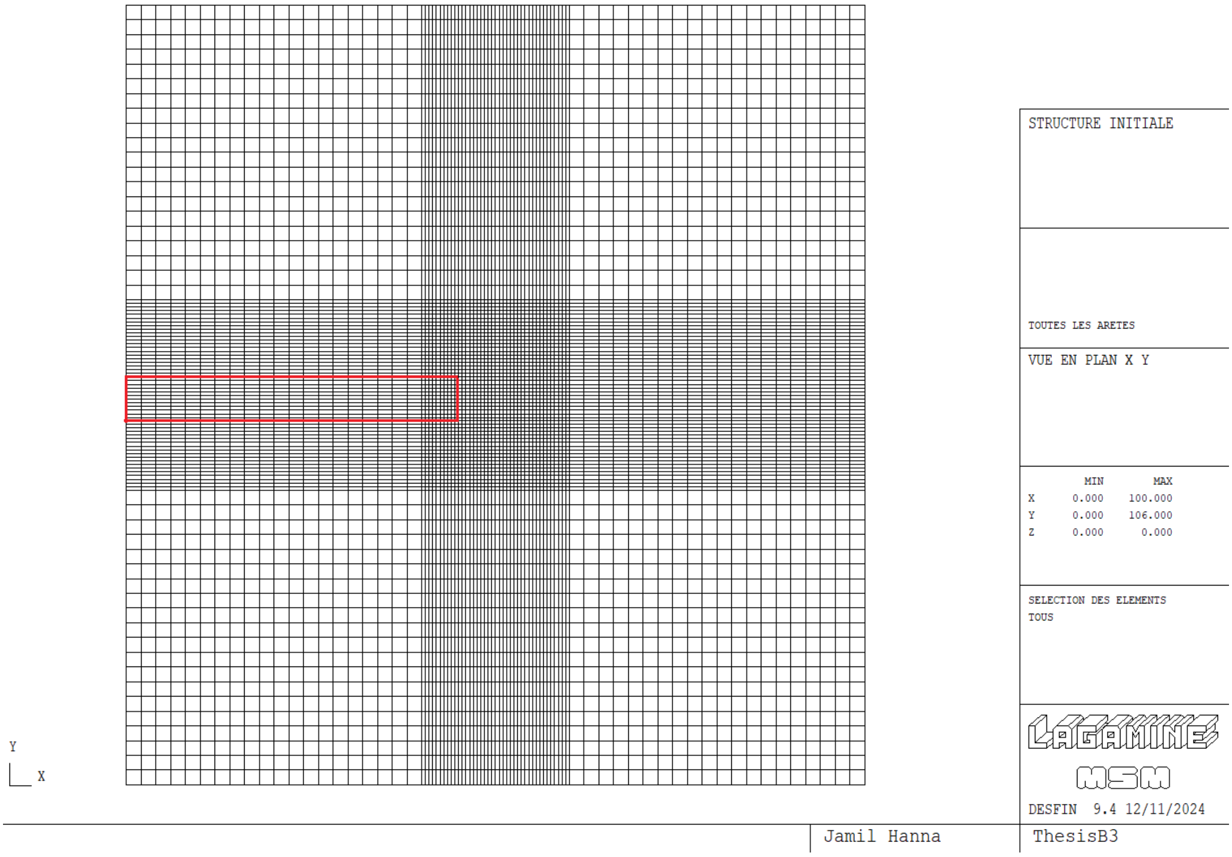

Figure 20: The mesh, the red rectangle represents the goaf

3.3 Different Cases Studies : Parameters and Setup

- **Case 1 :** In this case, we assumed simply supported boundary conditions and did not consider gravity in the model. Instead, gravity was replaced by a linearly distributed force of 1.24 MPa, which corresponds to the stress induced by the self-weight at the level of the goaf. This force was applied at the top of the model, as shown in Figure21.

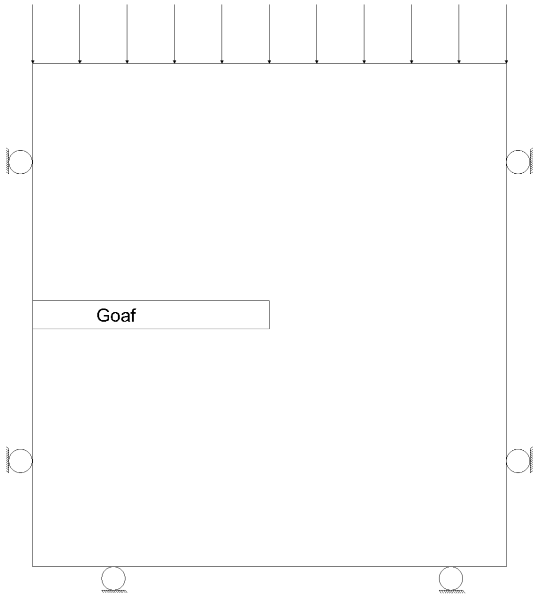

Figure 21: Boundary conditions and the distributed load

The initial tangent modulus of the rock E_0, depends largely on the bulking factor and the strength of rock fragments. It was calculated using the following equation:

$$E_0 = \frac{10.39 \cdot \sigma_c^{1.042}}{b^{7.7}} [28] \tag{32}$$

In this equation, b is the bulking factor of the caved rock, and σ_c is the compressive strength of the rock pieces. According to this equation, an increase in the strength of rock fragments and/or a decrease in the bulking factor leads to a significant increase in the initial tangent modulus of the goaf material.

Taking into consideration that K = 13.88 MPa following the paper of Yavuz, H. [28], and using the following equation we have calculated the Shear modulus,:

$$G = \frac{3KE}{9K - E} \tag{33}$$

Also, to calculate the Poisson ratio ν, we have used the following equation:

$$\nu = \frac{3K - 2G}{2(3K + G)} \tag{34}$$

The bulking factor b was used = 1 for the rock and b = 1.5 for the goaf and the compressive strength σ_c = 30 MPa in accordance with Yavuz, H. [28] paper .
Following the previous description, in Law 1 (intact rock properties), the model was defined as a mechanical model with the material exhibiting elastic behavior, where E = 359.56 MPa. For Law 2 (the goaf properties), the material also exhibited elastic behavior with E = 15.84 MPa and the unit weight in both laws (1 & 2) it was used as 0.024 MN/m^3. Law 3 was used to define the distributed load 1.24 MPa (LICHA).

- **Case 2:** In this case, we have used the same properties as in Case 1, but we have considered ELASTO-PLASTIC behavior of the goaf material, Therefore, for Law 2, we have taken the cohesion ($c = 1\,\mathrm{KPa}$ a very low value was selected for cohesion, as the goaf, consisting of an assembly of blocks, exhibits negligible cohesion and behaves as a granular material) and the angle of friction ($\phi = 5°$ it is a 1st trial considering a very low friction angle) into consideration and the yield surface is following Drucker-Prager criterion):.

- **Case 3:** For this case, it was similar to the case 2, with a change in the angle of friction ($\phi = 30°$).

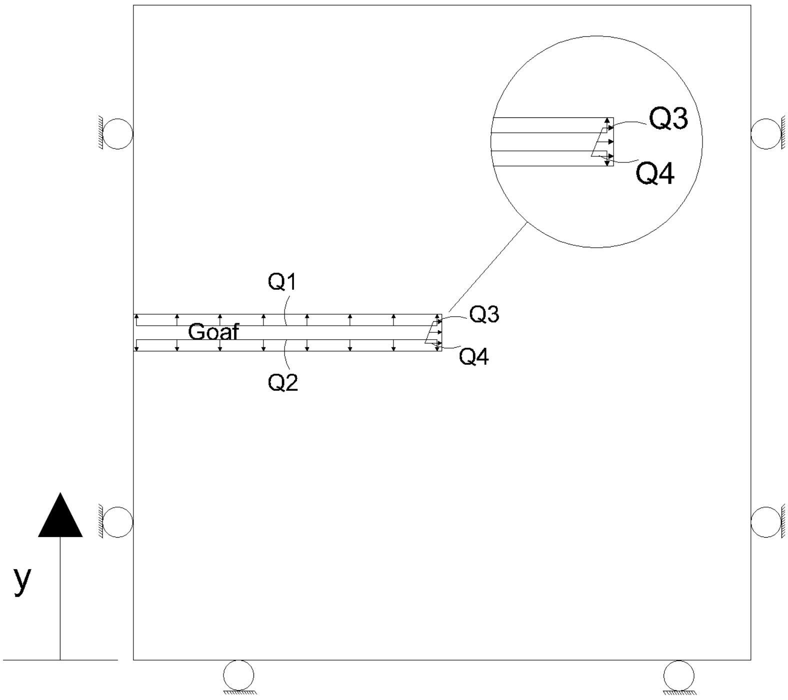

Figure 22: The applied loads on the edges on the goaf

- **Case 4:** In this case, we followed the same procedure as in previous cases, but we also considered gravity in all the calculations, using $g = 9.81\,\mathrm{m/s}^2$ and $\rho = 2400\,\mathrm{kg/m}^3$. For Law 2, we applied the Drucker-Prager criterion, using the same parameters as in Case 2. Additionally, we removed the distributed load from the top of the model (Law 3) and applied various loads along the edges of the goaf, as shown in Figure 22. These edge loads were then gradually removed to allow the goaf edges to collapse, simulating real-world conditions. The applied forces were calculated using the following equations:

$$Q_1 = \rho \cdot g \cdot h = 2400 \times 9.81 \times 50 = 1,177,200\,\mathrm{Pa} = 1.17\,\mathrm{MPa} \tag{35}$$

$$Q_2 = \rho \cdot g \cdot h = 2400 \times 9.81 \times 56 = 1,317,600\,\mathrm{Pa} = 1.31\,\mathrm{MPa} \tag{36}$$

$$K_0 = \frac{\nu}{1-\nu} = \frac{0.31}{1-0.31} = \frac{0.31}{0.69} = 0.449 \tag{37}$$

$$Q_3 = Q_1 \cdot K_0 = 1.17 \times 0.449 = 0.525\,\mathrm{MPa} \tag{38}$$

$$Q_4 = Q_2 \cdot K_0 = 1.31 \times 0.449 = 0.588\,\mathrm{MPa} \tag{39}$$

Taking into the consideration that the initial stress in the goaf was calculated using the following equations :

$$\sigma_v = H \cdot g \cdot \rho - g \cdot \rho \cdot y \tag{40}$$

$$\sigma_H = \sigma_v \cdot K_0 \tag{41}$$

Where H is the total height of the model = 106 m, and y is variable starting from the bottom of the model as shown in Figure 22.

- **Case 5:** This case was the same of Case 4, but with a change in the angle of friction following the same change done in Case 3.

- **Case 6:** This case was similar to case 5 but we have added the factor of plastic compressibility β using the equation 42 :

$$\beta = \frac{1 + e_0}{\lambda - \kappa} \tag{42}$$

While e_0 represents the void ratio, *lambda* is the compression index and κ is the swelling index [2]. κ can be neglected because it is too small,

$$e_0 = \frac{\eta_0}{1 - \eta_0} \tag{43}$$

Where η_0 is the porosity and can be calculated using Figure 23 and the following equation, taking into consideration the 4 m of intact rock is transformed into 6 m of goaf :

$$\eta_0 = \frac{V_{voids}}{V_{tot}} = \frac{2}{6} = \frac{1}{3} \tag{44}$$

and $\lambda = 0.003$ using a mean value from the data available in the paper of (H. Arasteh, G. Saeedi, M. A. Ebrahimi Farsangi, K. Esmaeili (2020)) [12].
Leading to $\beta = 500$.

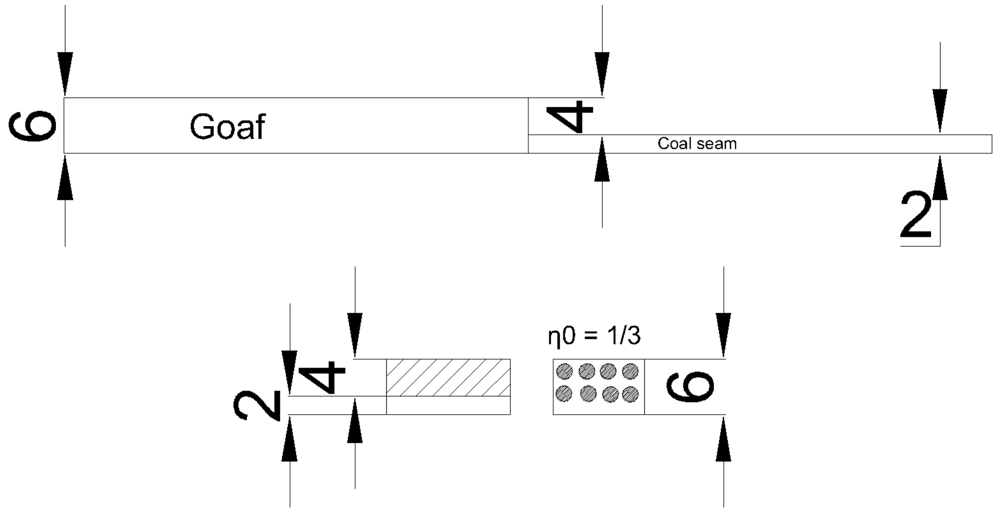

Figure 23: Calculation of η_0

The following table summarize all parameters used in all of the cases :

	σ_c (MPa)	E_{rock} (MPa)	E_{goaf} (MPa)	ν	K (MPa)	G (MPa)	ρ (kg/m^3)	c (kPa)	ϕ (deg)	β
Case 1	30	359.56	15.84	0.31	13.88	6.04	2400	-	-	-
Case 2	30	359.56	15.84	0.31	13.88	6.04	2400	1	5	-
Case 3	30	359.56	15.84	0.31	13.88	6.04	2400	1	30	-
Case 4	30	359.56	15.84	0.31	13.88	6.04	2400	1	5	-
Case 5	30	359.56	15.84	0.31	13.88	6.04	2400	1	30	-
Case 6	30	359.56	15.84	0.31	13.88	6.04	2400	-	30	500

Table 1: Parameters used for the modeled cases

3.4 Validation of the Model

To validate the model we have considered that the goaf and the rock have the same parameters (elastic parameters), and we have considered that a distributed load 1.24 MPa loads the top of the model, while the elastic modulus was equal to 100 MPa and Poisson ratio was equal to 0.2 . The following Figure 24 shows a comparison between the analytical study and the LAGAmine results and we can see that they were identical.

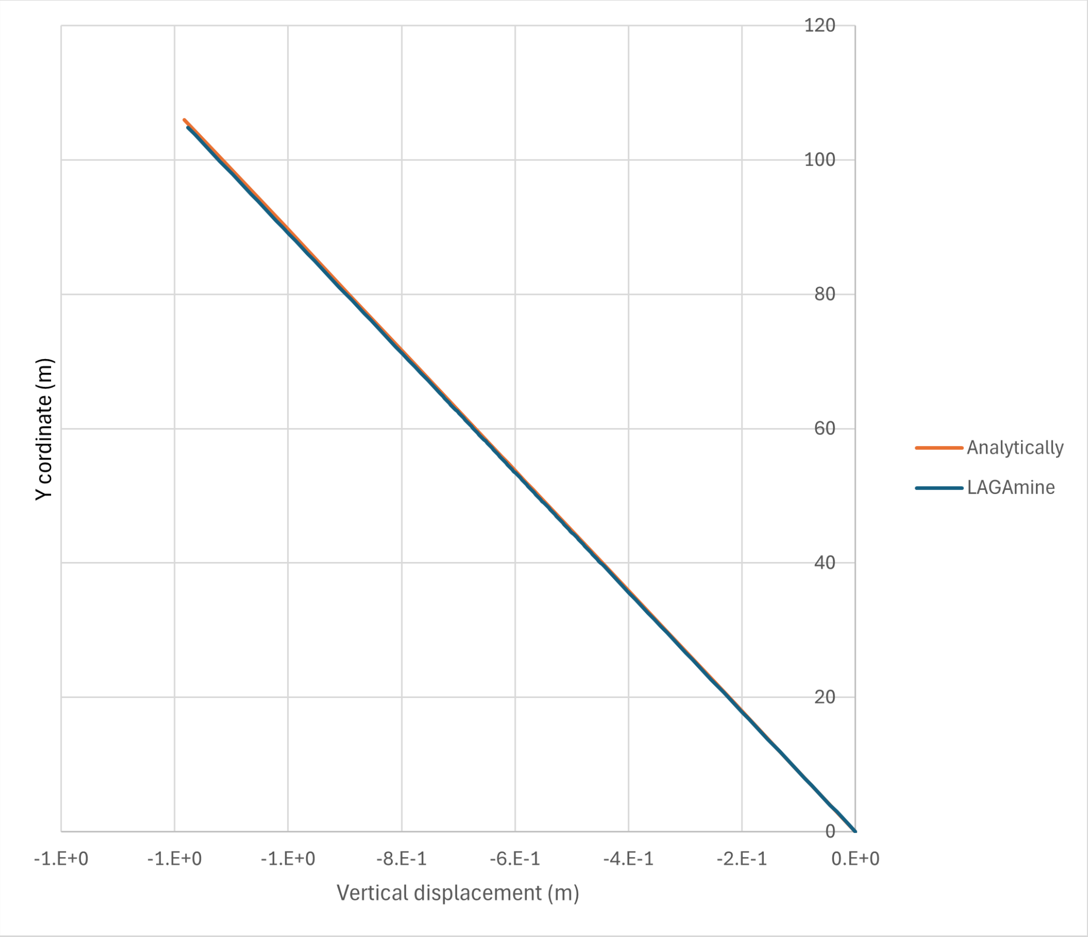

Figure 24: Comparison between the analytical study and LAGAmine

4 Results and Discussion

4.1 Analytical vs. Numerical Results

The analytical study models a 1D column of ground, ignoring the lateral influence of surrounding materials, particularly the goaf. The oedometric modulus, calculated as

$$E_{\text{oed}} = E\frac{(1-\nu)}{(1+\nu)(1-2\nu)} \tag{45}$$

While E1 = 359.56 MPa for rock and E2 =15.84MPa for goaf, assumes a Poisson's ratio of ν = 0.31. This simplification treats the ground as a single axis of deformation, without any lateral constraints or support. For Case 1, a simply supported boundary conditions have been applied with a linearly distributed load of 1.24 MPa at the top. Here, the initial tangent modulus E_0 is influenced by the strength of the rock fragments and the bulking factor, calculated using b=1 for rock and b=1.5 for goaf. The properties of the goaf, particularly its lower shear modulus G = 6.04 MPa and the bulk modulus K = 13.888 MPa, lead to softer behavior compared to the more rigid rock, So we have plotted the strain = stress/oedometric modulus to the Y coordinates.

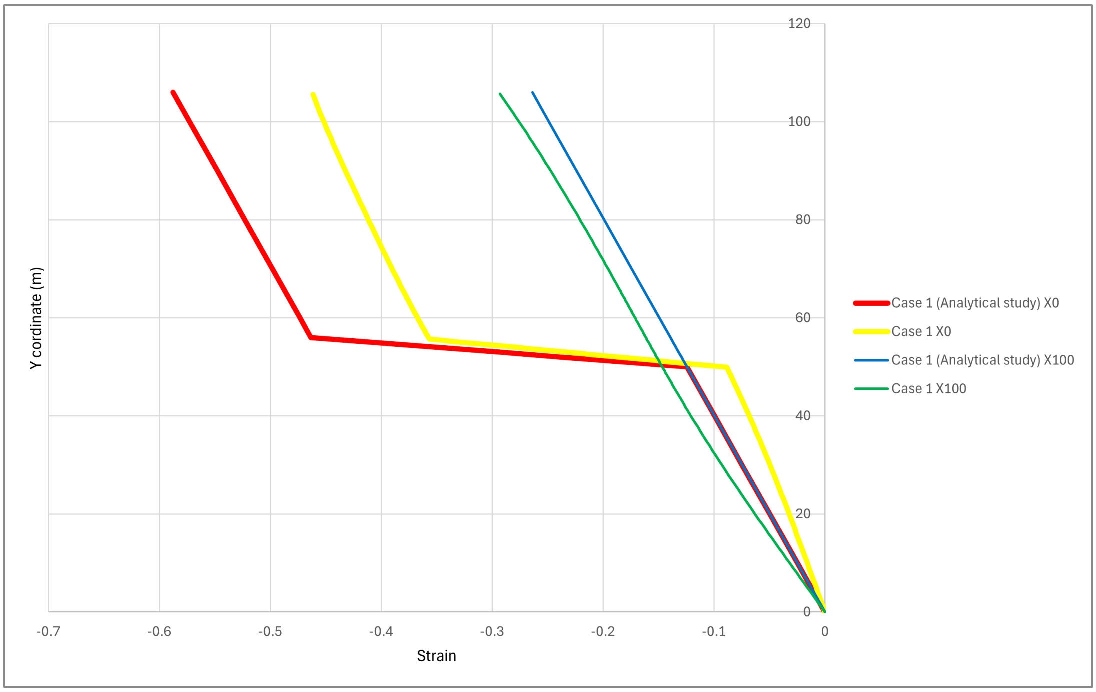

Figure 25: Comparison between the analytical study and LAGAmine Case 1 (Section X0 and Section X100)

The figure illustrates the comparison. At section X0 (red and yellow curves), the model exhibits greater stiffness than the analytical solution. This is not solely due to the lateral constraints from surrounding materials but rather the combined effect of the goaf's limited horizontal extension and the intact rock. In the model, the goaf is partially supported by the intact rock in the unexcavated zone, which reduces the stress transmitted through the goaf and results in less deformation. The analytical solution, being 1D, does not account for this interaction or the limited horizontal extent of the goaf, leading to a less stiff response.

At section X100 (blue and green curves), the model shows softer behavior due to the influence of the goaf. The goaf's lower modulus allows for greater deformation, and the limited extent of the goaf still plays a role by modifying the settlement compared to a case with infinite horizontal extension. This highlights how the simplified 1D analytical model underestimates the complexities of a 2D reality, especially in regions affected by interactions between fractured and intact materials, such as the goaf and surrounding rock.

4.2 Comparative Analysis of Results

The sections taken to extract results where as the following Figure 26

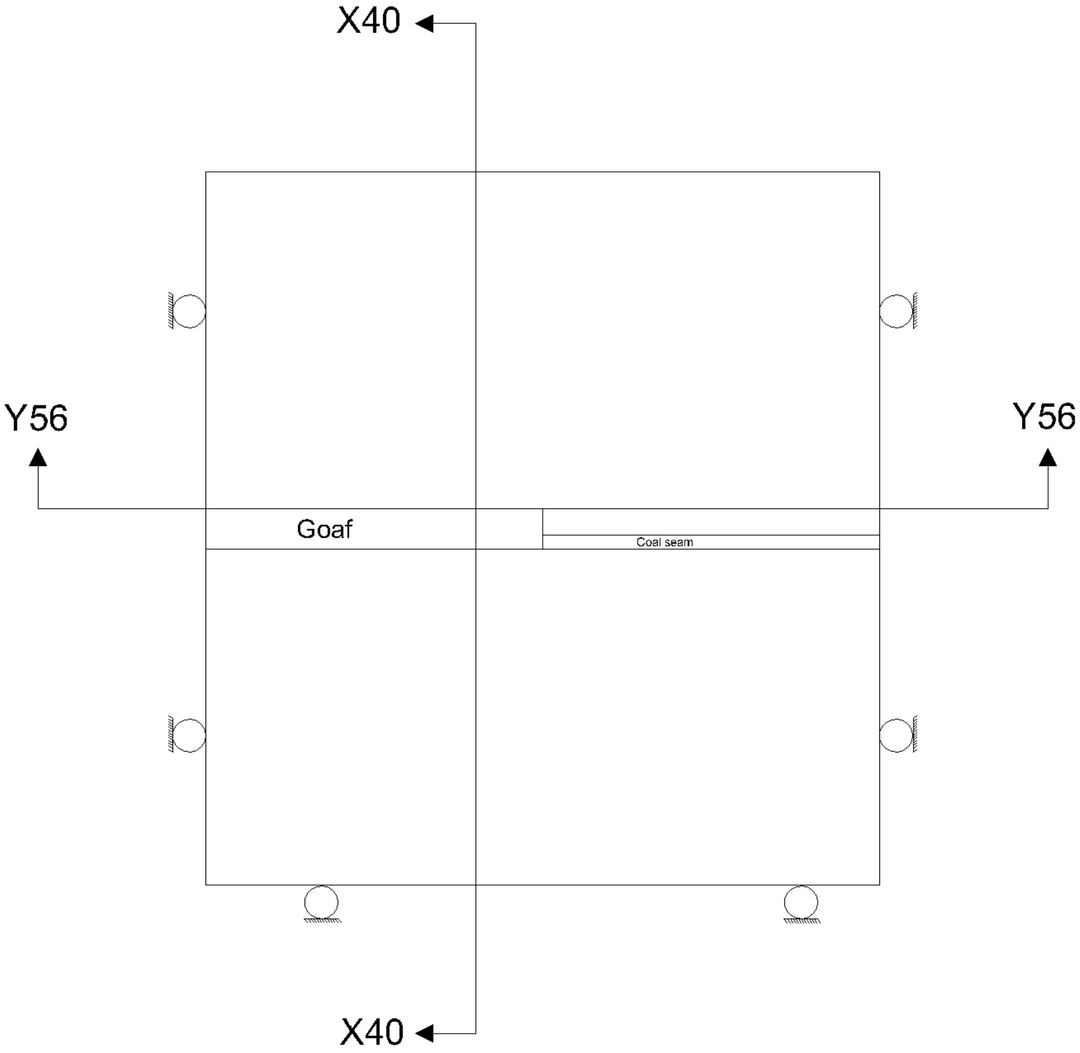

Figure 26: Sections used to extract results

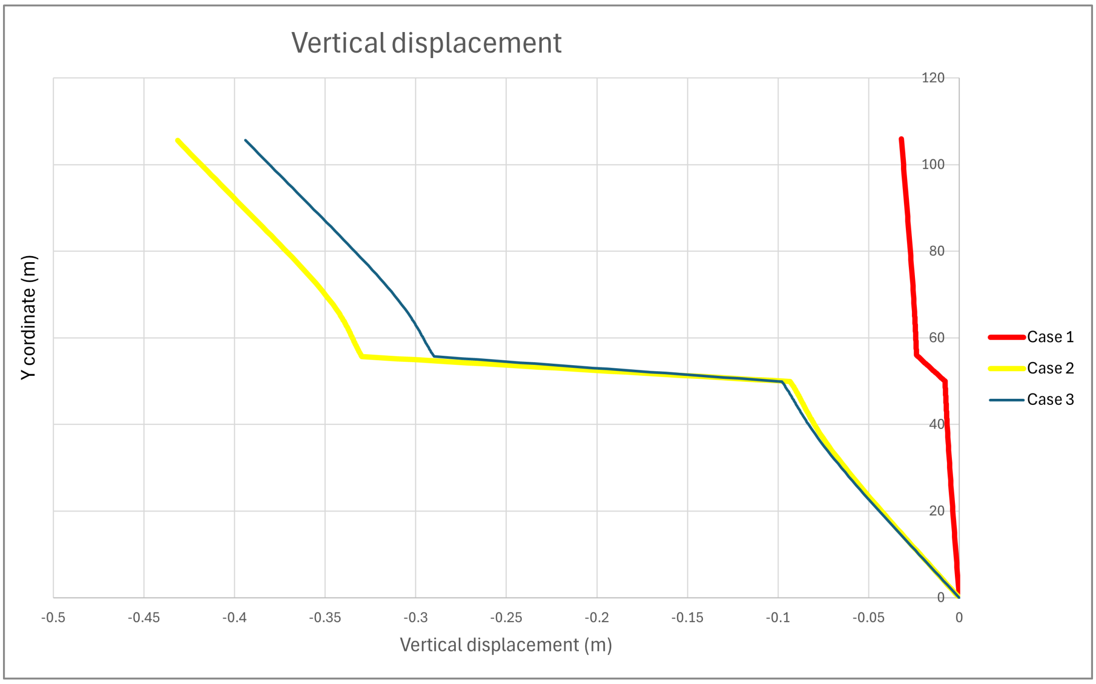

Figure 27: Effect of parameters (Section X40)

The slope of the curve (gradient of displacement) correspond to the vertical strain (deformation). Here you can see that the vertical deformation is purely in compression (because the slope is always positive). This is due to the fact that all the part (the intact rock and the goaf) are compressed due to the top load. Also, the magnitude of compression (magnitude of the slope of the curve) depends on the stiffness. This is why the goaf develop more compressive deformation than the intact rock.

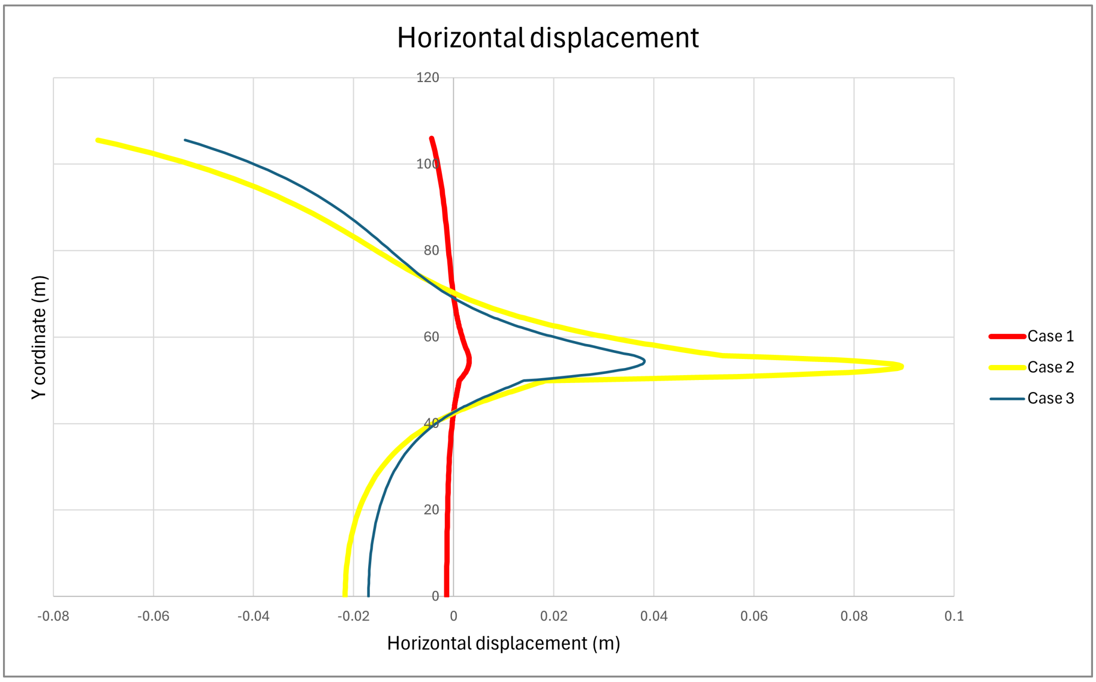

Figure 28: Effect of parameters (Section X40)

The vertical compression of the goaf induces an horizontal extension. This is due to Poisson effect. Consequently, a vertical section of the goaf is pushed to the right (due to extension). The comparison indicates that the amount of displacement goes up considerably when passing from elastic (Case 1) to elasto-plastic behavior (Case 2), emphasizing the contribution of plasticity to the deformation of the material. Nonetheless raising the friction angle under Case 3 reduced the displacement, showcasing the counterproductive effect of increased shear resistance, where higher shear resistance leads to reduced plasticity and consequently less deformation.

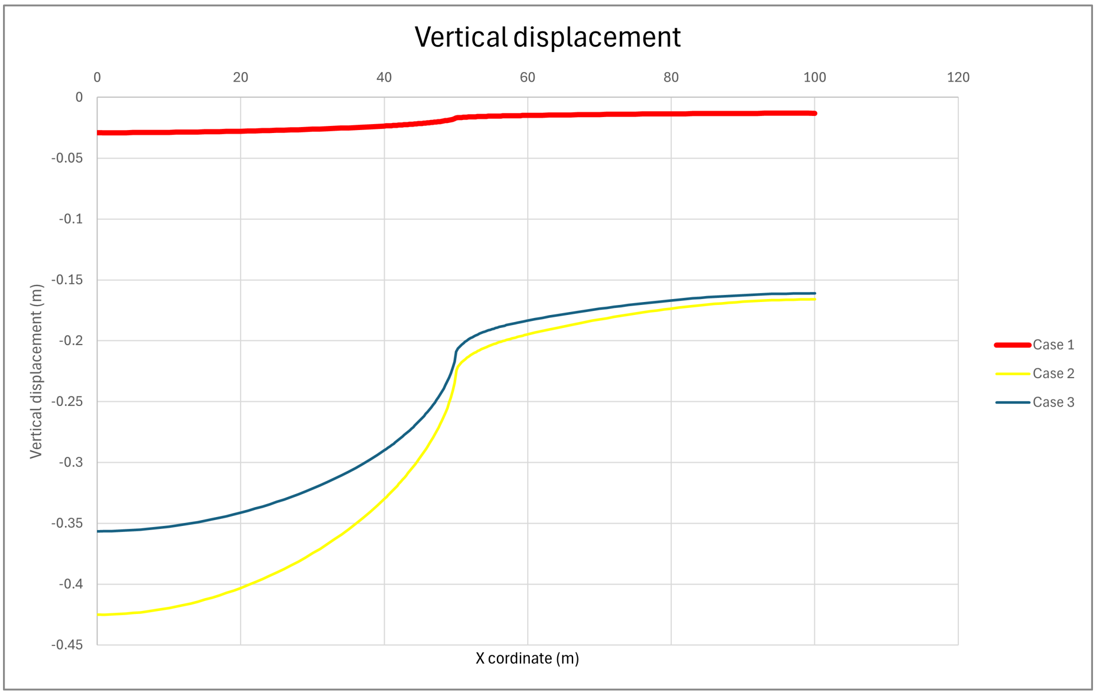

Figure 29: Effect of parameters (Section Y56)

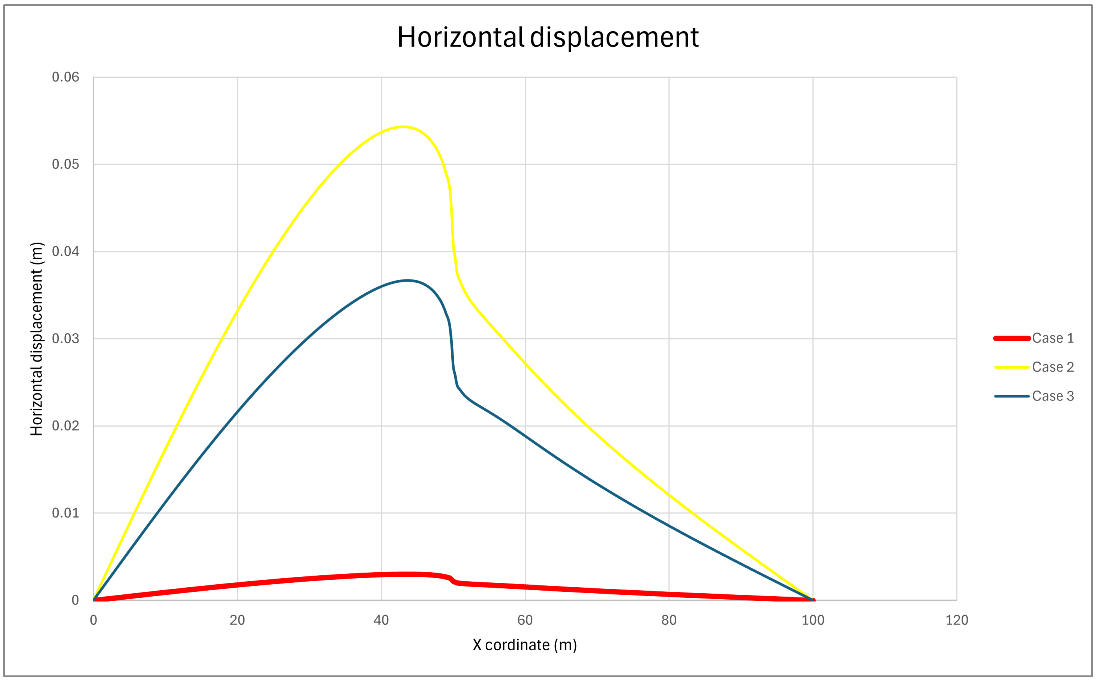

Figure 30: Effect of parameters (Section Y56)

As shown in Figures 27, 28, 29, 30, the shift from elastic to elasto-plastic behavior (Case 1 to Cases 2 and 3) considerably influences the horizontal displacement by enabling the material to accommodate more strain. Increasing the friction angle from 5° to 30° significantly enhances horizontal displacement, and it is logical, because it means that the material is stronger and it will deform less (less plasticity = more strength). The difference in displacement magnitudes illustrates the impact of material properties, including friction and cohesion, as well as the behavioral model (elastic versus elasto-plastic) on the deformation characteristics of the goaf.

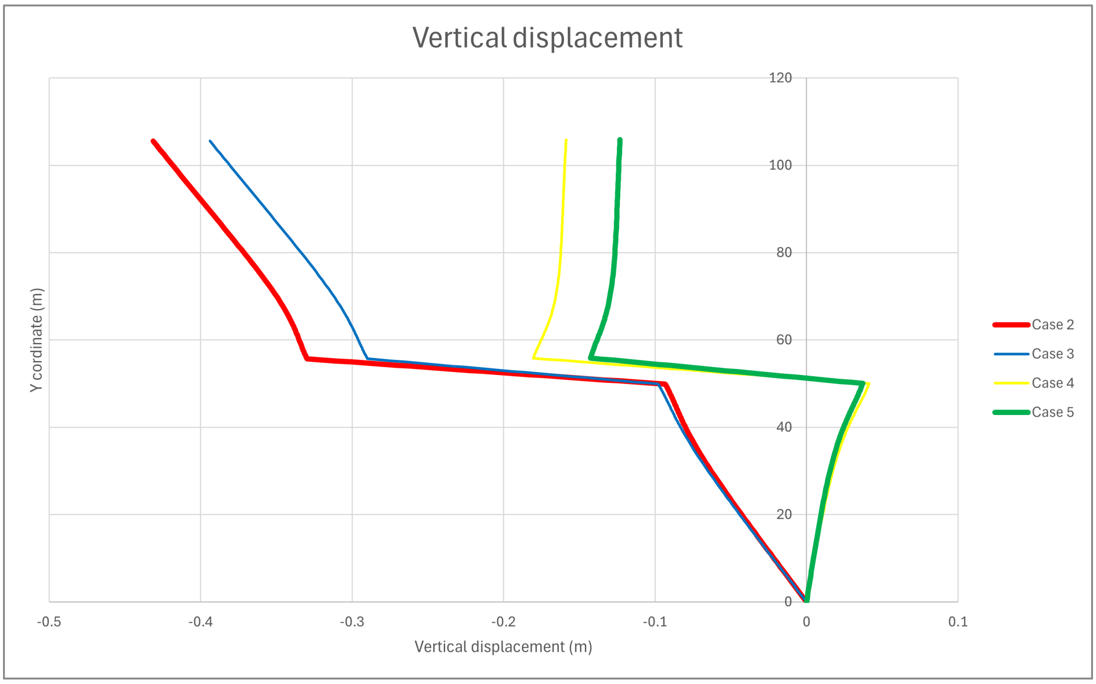

Figure 31: Effect of type of boundary conditions (Section X40)

Actually in figure 31, we see that the strain of the goaf is relatively similar between the two modes of loading because the loading of the goaf is more or less 1.24 MPa in both modes (surface load and gravity effect). However, the difference is much more significant in the intact rock. For the surface load, the intact rock is loaded by a stress of 1.24 MPa, whereas in the case of gravity (Cases 4 and 5), the intact rock is partially unloaded. The goaf is under compressive strain, while the intact rock is under extension.

At the initial state, the intact rock is loaded by the stress applied at the edges of the goaf (see Figure 22), meaning the goaf does not support any load. Then, as the stress is removed, the intact rock undergoes unloading, and a progressive mobilisation of stress occurs in the goaf. Consequently, stress is partially released in the intact rock, while the goaf is loaded.

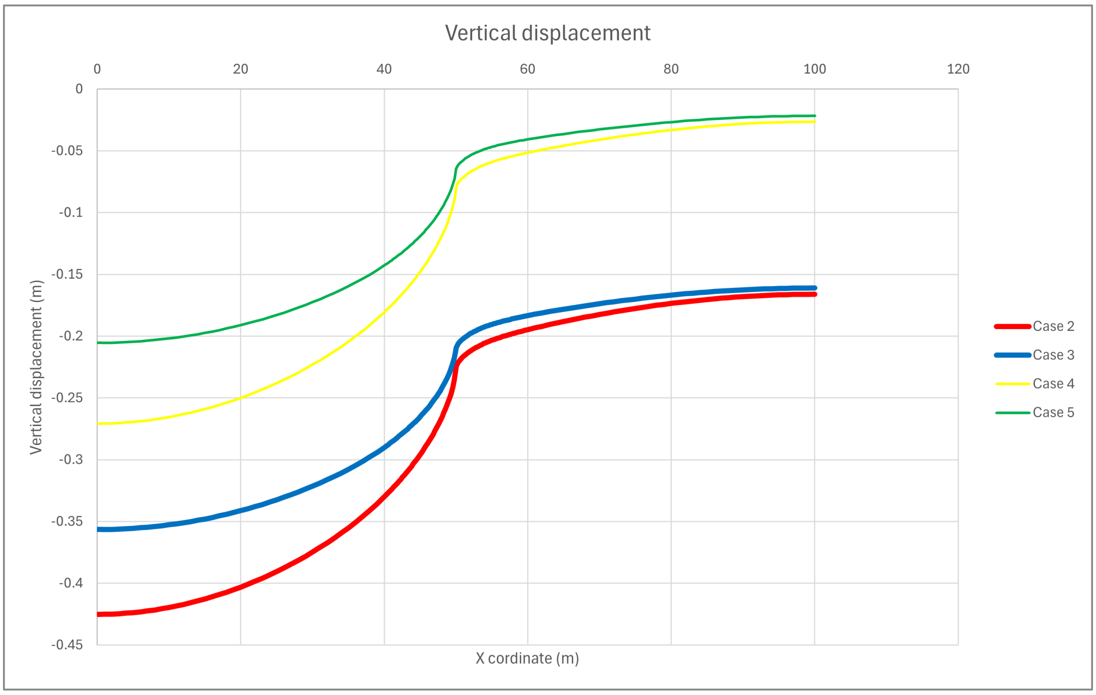

Figure 32: Effect of type of boundary conditions (Section Y56)

As we can see in figure 32, cases 2 and 3 develop more settlement than cases 4 and 5 because case 2 and 3 the intact rock is loaded (by the surface loading) while in case 4 and 5 the intact rock is unloaded.

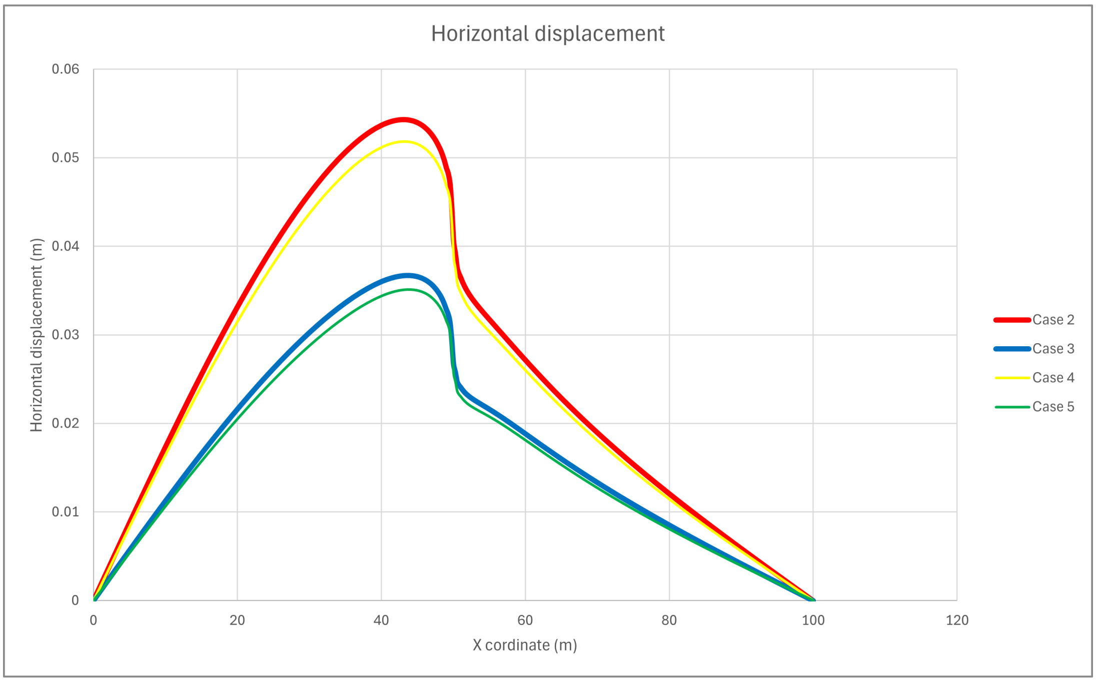

Figure 33: Effect of type of boundary conditions (Section Y56)

Simply supported boundaries with linearly distributed loads fix the horizontal displacements, stabilizing the structure. When gravity and edge loading are introduced, the model allows for greater displacement, simulating realistic settlement and collapse. The comparison demonstrates that boundary conditions, especially the incorporation of gravity and the elimination of top loads, significantly influence displacement behavior, producing a more realistic response in the model.

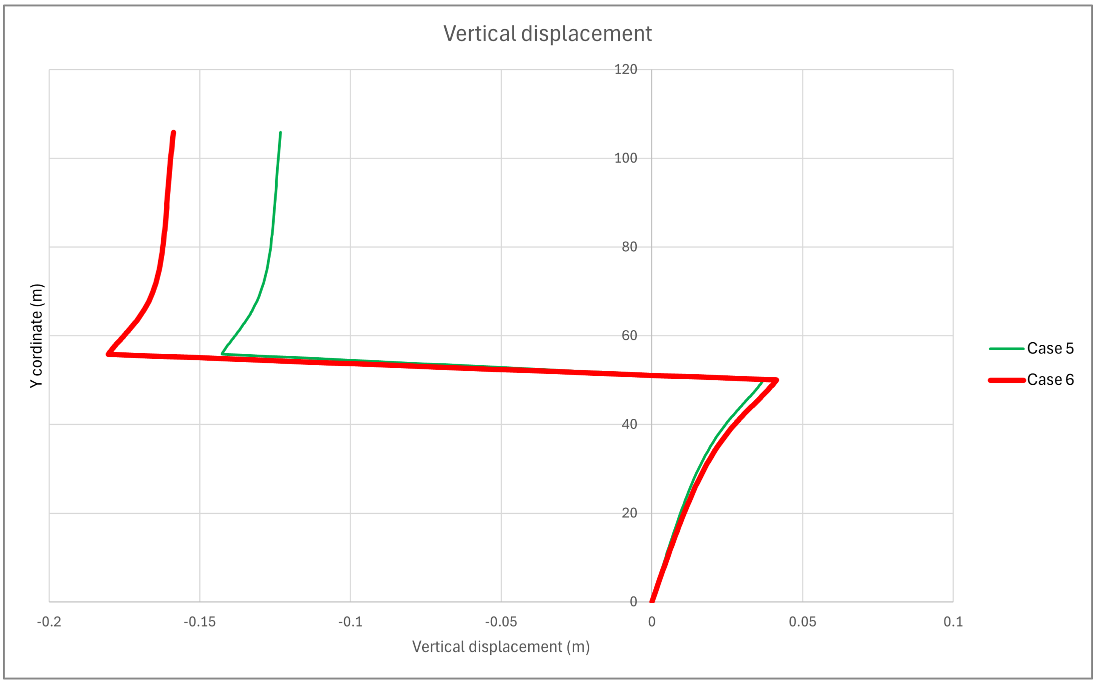

Figure 34: Effect of changing the factor β (Section X40)

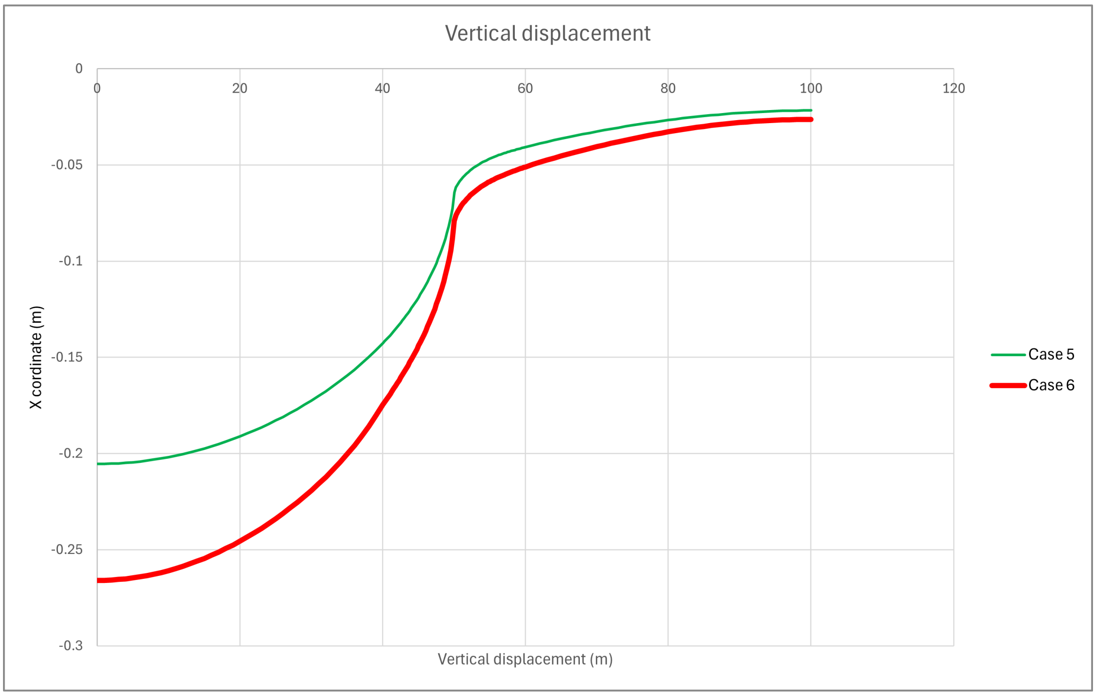

Figure 35: Effect of plastic compressibility factor β (Section Y56)

In a comparison of Case 5 with Case 6 (figure 35), we show that plastic compressibility β is one key reason over to the deformation characteristics of goaf material. Case 5 illustrates the elasto-plastic respons using Drucker-Praguer model with plastic compressibility mechanism, while case 6 accounts for the compressibility of material and is thus likely to have much higher and probably more distributed displacements. Findings from this study are critical to understanding collapse behaviour in longwall mining and also the controlling effects of material properties on deformation.

4.3 Displacement and Stress of shear and collapse model

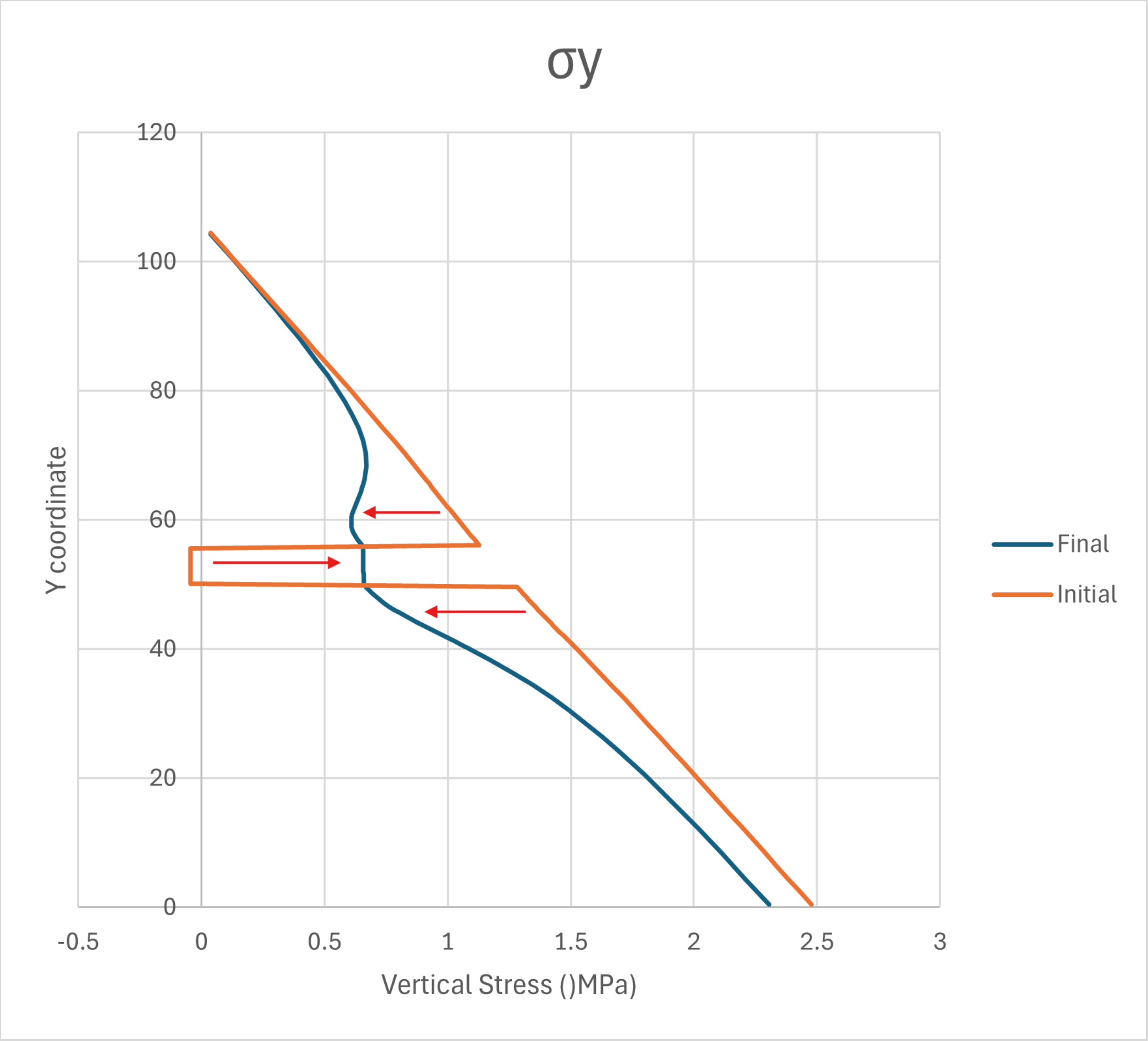

Figure 36: Vertical Stresses Case 6 Section X40

As illustrated in figure 36, the initial stress profile shows that the stress is partially released in the intact rock and is increased in the goaf. That explain the reason of goaf contraction and intact rock extension.

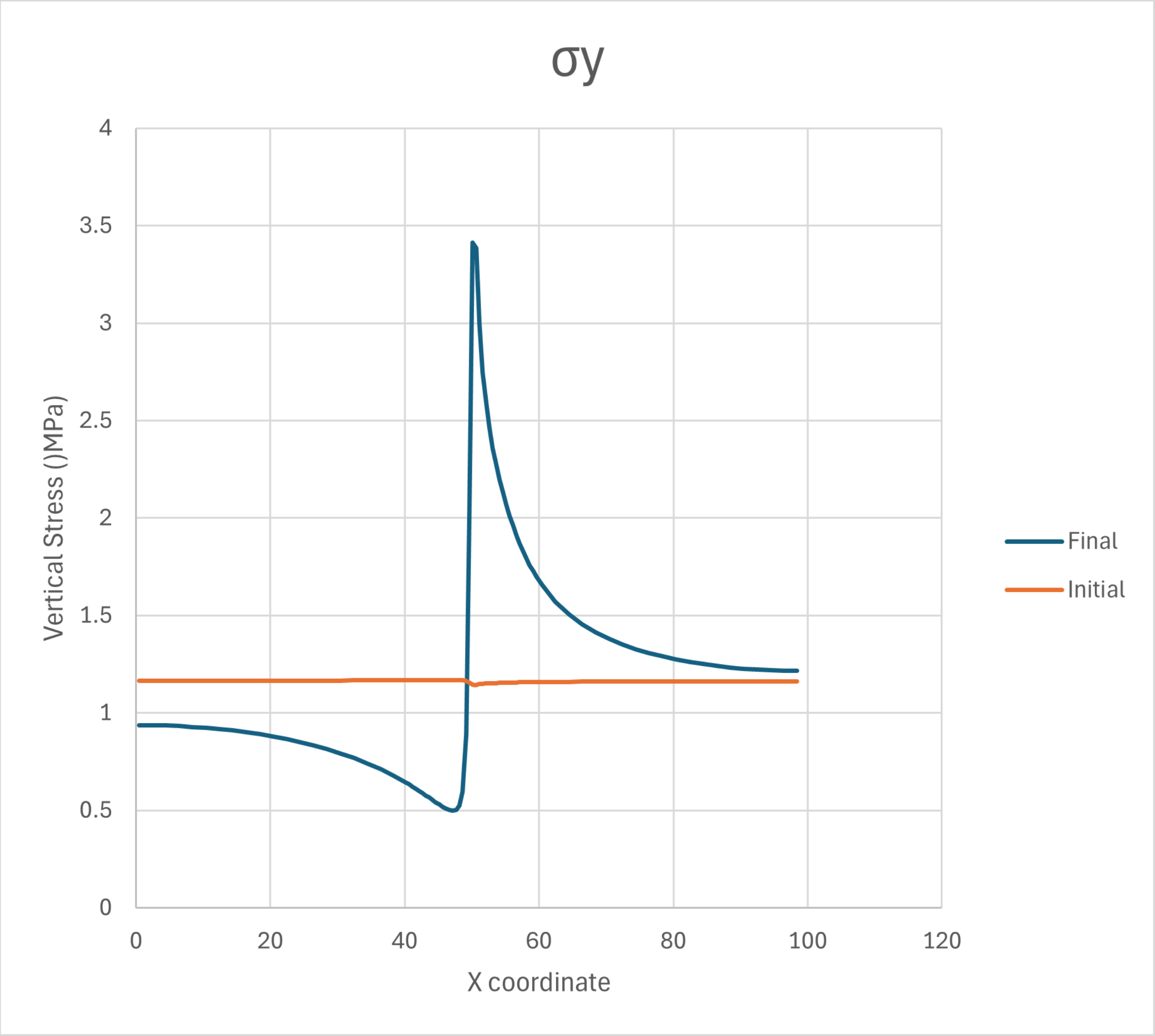

Figure 37: Stresses Case 6 Section Y56

We can see in figure 37, that the initial stress was almost perfectly horizontal, because at the beginning we have the pressure applied at the goaf edge, which compensates exactly the self-weight. So we should have a uniform distribution stress as if the goaf was not there (as if we have the intact rock everywhere). In comparison with figure 7, it is clear that we can reproduce the peak of the vertical stress at the end of the goaf, where a stress concentration occurs at the face of the goaf due to the contrast in stiffness. The intact rock is much more rigid than the goaf material, causing the vertical stress induced by the self-weight of the rock to be 'attracted' by the more rigid material.

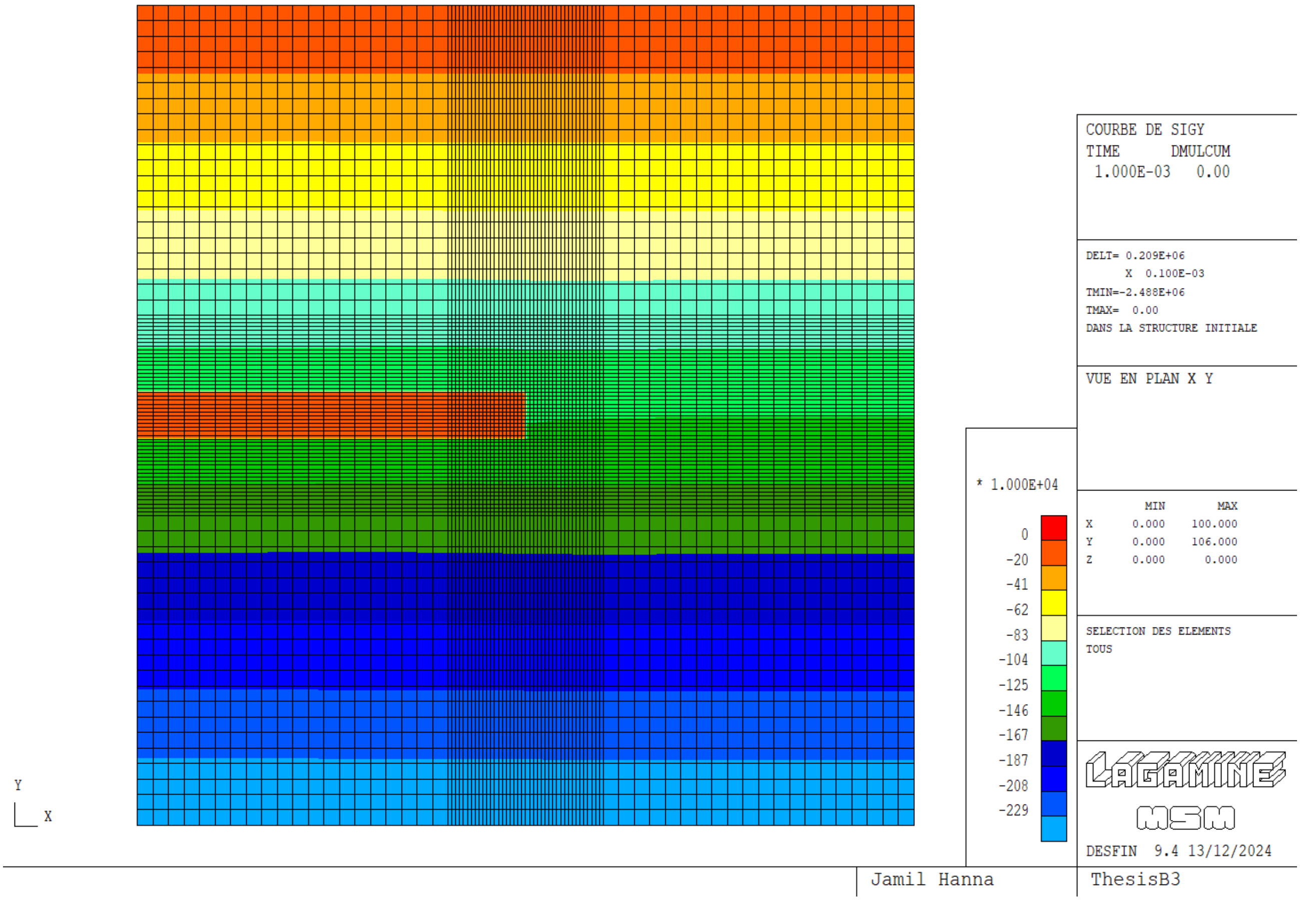

Figure 38: Initial stress σ_y, the red rectangle represents the goaf zone

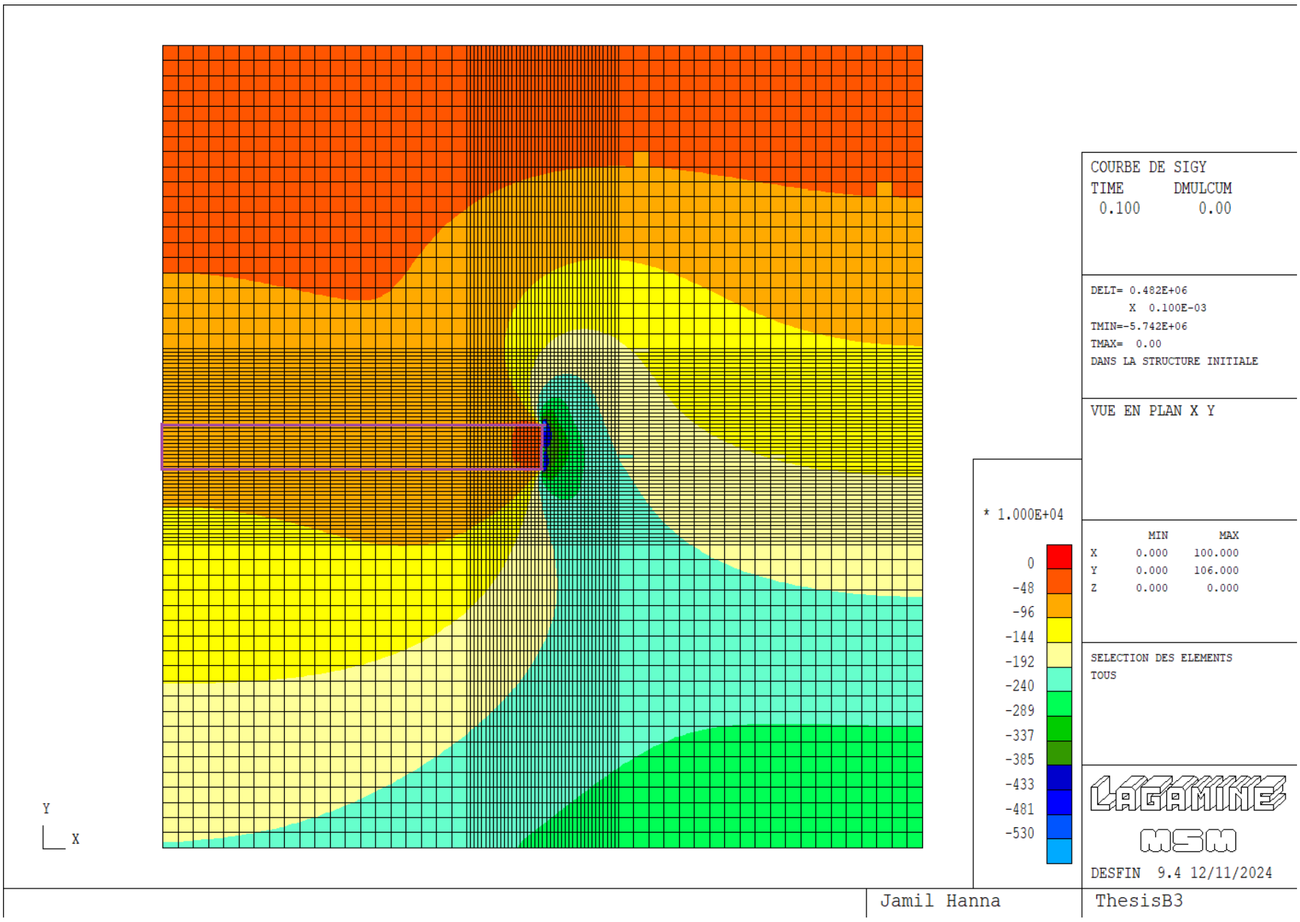

Figure 39: Stress σ_y, the purple rectangle represents the goaf zone

As shown in Figure 39, there is a strong stress redistribution at the edge of the goaf. Initially, the stress exhibits a linear distribution (horizontal color) as shown in figue 38, but at the edge of the goaf, it becomes significantly disturbed. This is due to the stark contrast between the low stiffness of the goaf and the high stiffness of the intact rock. Consequently, stress concentrates in the stiffer material, resulting in an intense blue color in the intact rock and a low-intensity orange color in the goaf. The stiffer material attracts the stress, leading to stress concentration at the edge of the goaf. Progressively farther away from the goaf, the stress transitions from orange to green, and at the edges of the model, the distribution appears more or less linear.

5 Parametric Study

5.1 Introduction

After establishing a reference model, a parametric study is now made. In particular, based on the latter, that is to say keeping the same loading, the same numerical materials properties model (except if the contrary is specified), the same kind of parameters , four other models were created. For each of these models, one (and only one) parameter is modified in order to study the influence of the latter on the behaviour of the model. Therefore, to begin this chapter, the first section is dedicated to a representation and a description of the different studied models but also to an explanation of why those ones have been studied and their sensitivity on the results because some of the parameters have been assumed and others we have calculated them. Then, an analysis of the numerical results of the different models is made. Furthermore, results of each models are compared to the one of the reference model. It has to be noticed that only main (and most interesting) results are presented here in order not to be too repetitive.

5.2 Description of the different studied models

5.2.1 Effect of changing the plastic compressibility factor (β)

In this first model, we have changed the plastic compressibility factor (β), in the reference case (case 6) it was equal to 500, and we have studied it starting from high compressibility factor when β=100 to a low compressibility factor when β=2000 by changing the value of λ to see if the vertical displacements might be smaller or bigger.

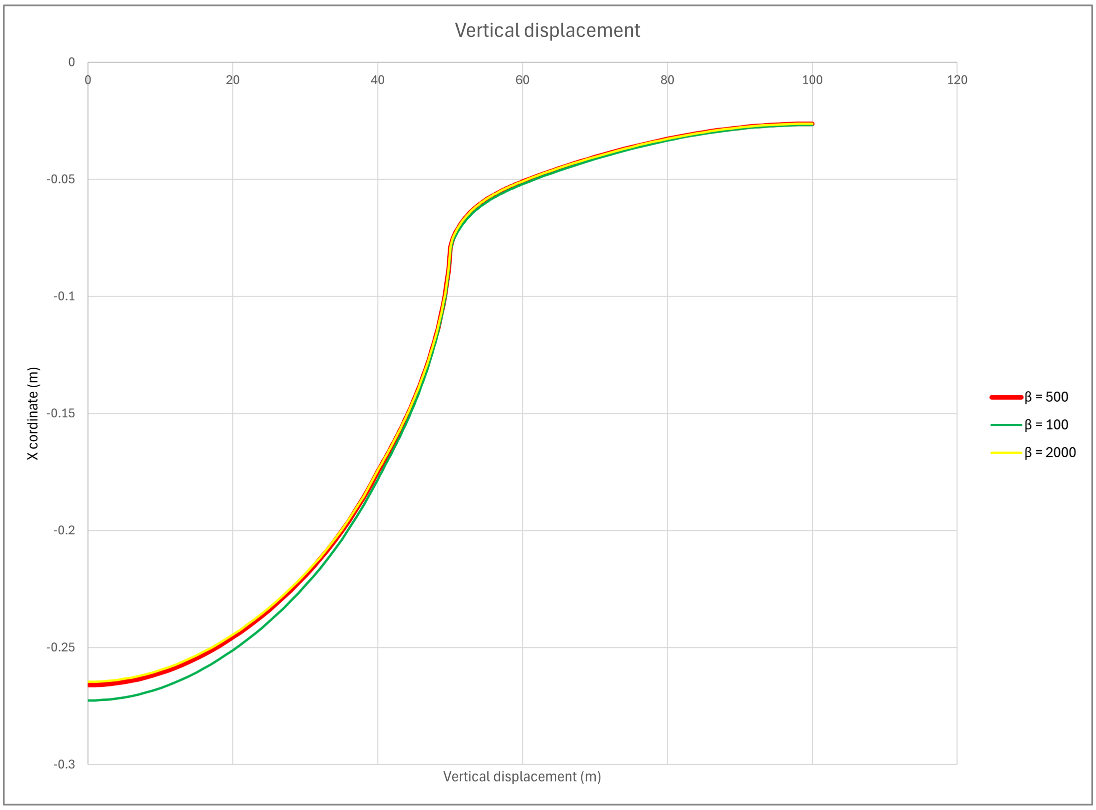

Figure 40: Effect of changing the factor β (Section Y56)

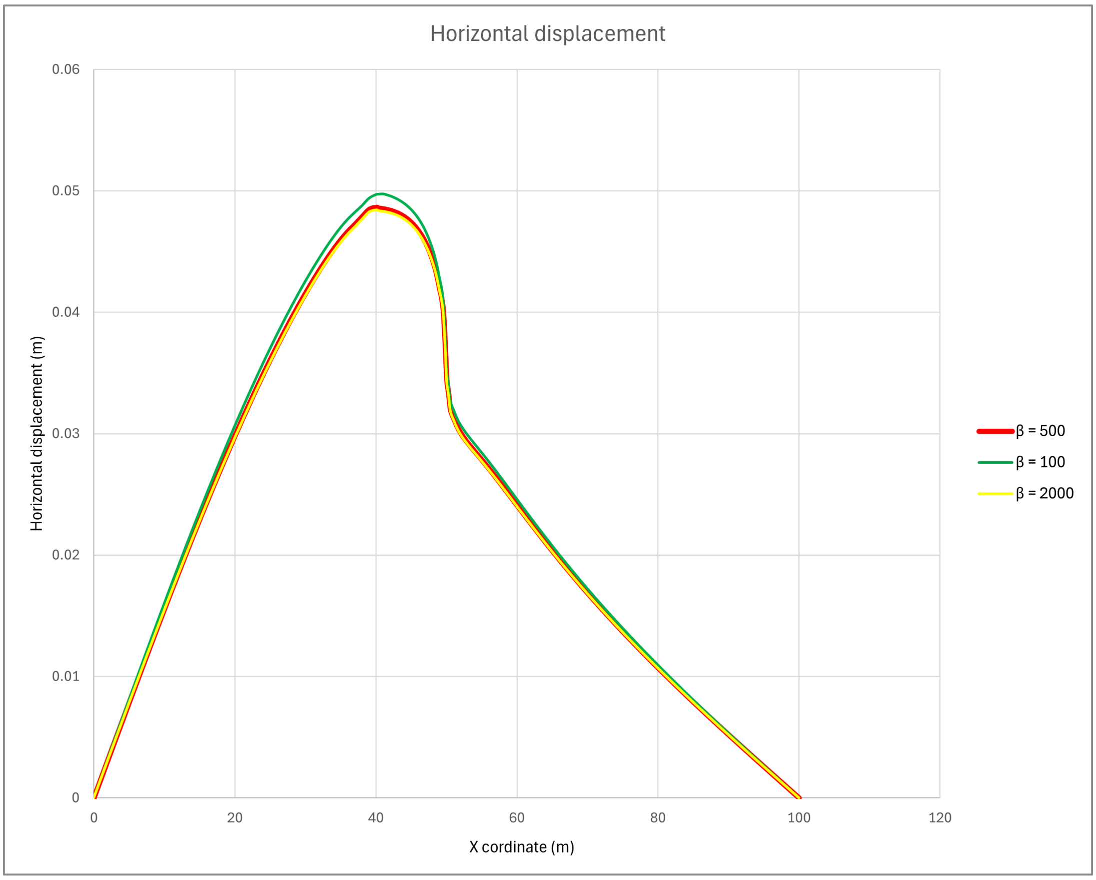

Figure 41: Effect of changing the factor β (Section Y56)

As shown in the previous Figures 48, 49 the slight differences in vertical displacements between different plastic compressibility factors (100, 500, 2000) implies the deformation in this model is not significantly based on any volumetric plastic strain, rather, shear deformation or elastic properties govern this model. This likely results in limited sensitivity due to the boundary conditions and material behavior in the simulation, since volumetric constraints seem to cover up minor influences from changes in the plastic compressibility factor.

5.2.2 Effect of changing the lateral boundary conditions

After changing the plastic compressibility factor we have thought of investigating the effect of changing the lateral boundary conditions, because we have assumed that the goaf and the intact rock have the same width and which might not be realistic in real life so, four scenarios with different geometric dimensions were studied: Initially, both the goaf and coal seam widths were 50 metres. Then we looked at scenarios with (1) a 50 m goaf and a 100 m coal seam (Figure 42a), (2) a 100 m goaf and a 50 m coal seam (Figure 42b), and (3) both widths of 100 m (Figure 43b).

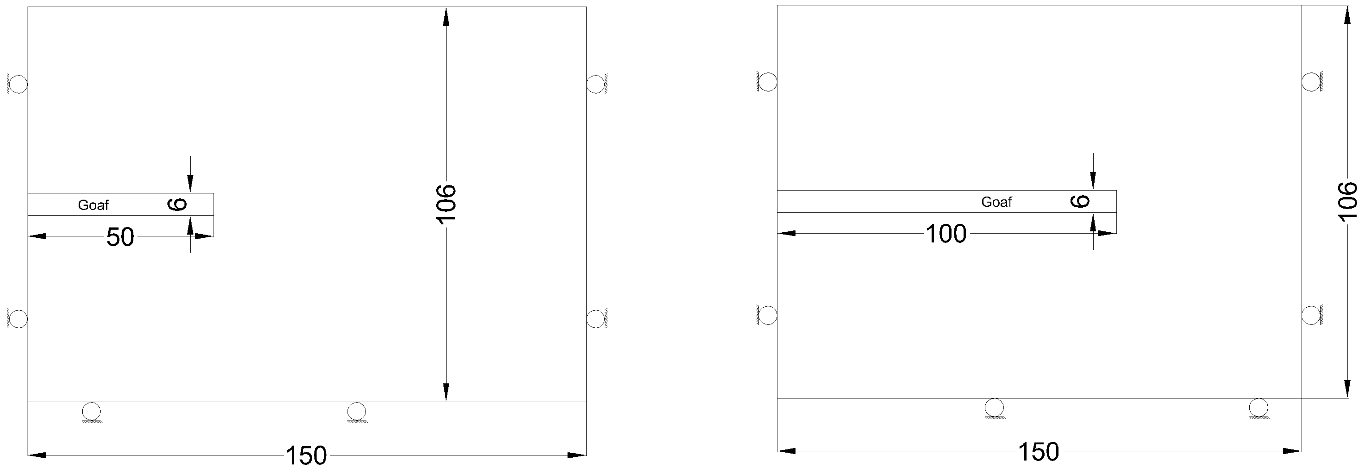

(a) A 50 m goaf and a 100 m coal seam.

(b) A 100 m goaf and a 50 m coal seam.

Figure 42: Representation of the second parametric model.

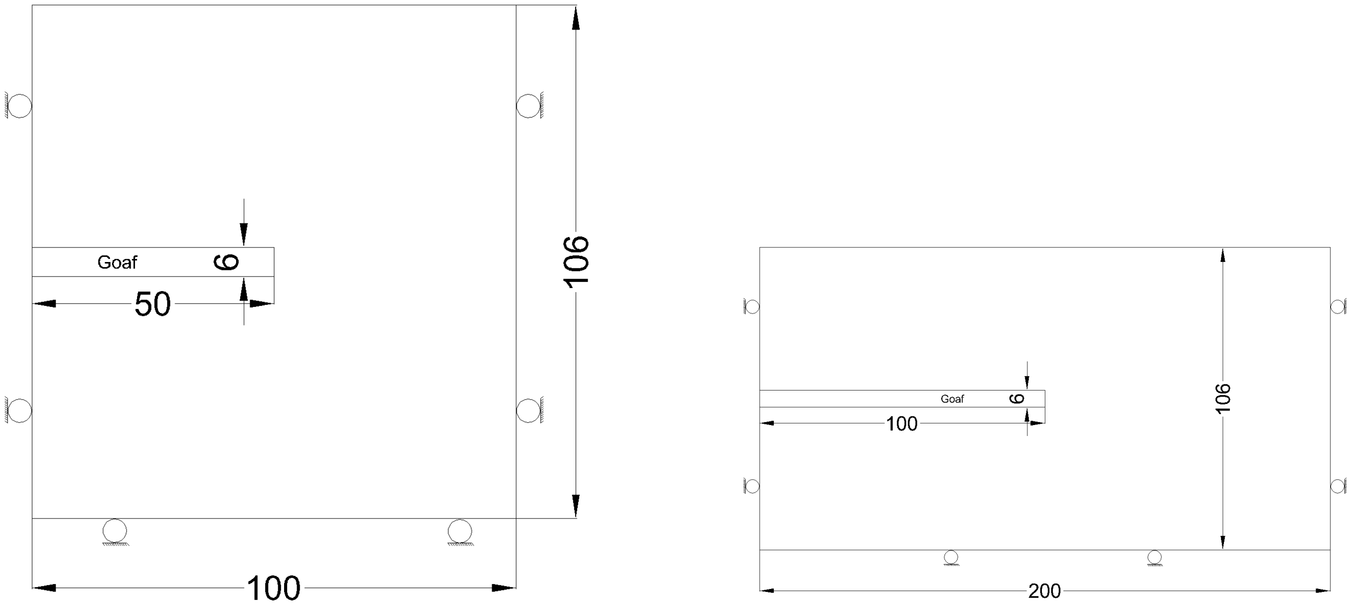

(a) Both widths of 50 m.

(b) Both widths of 100 m.

Figure 43: Representation of the second parametric model.

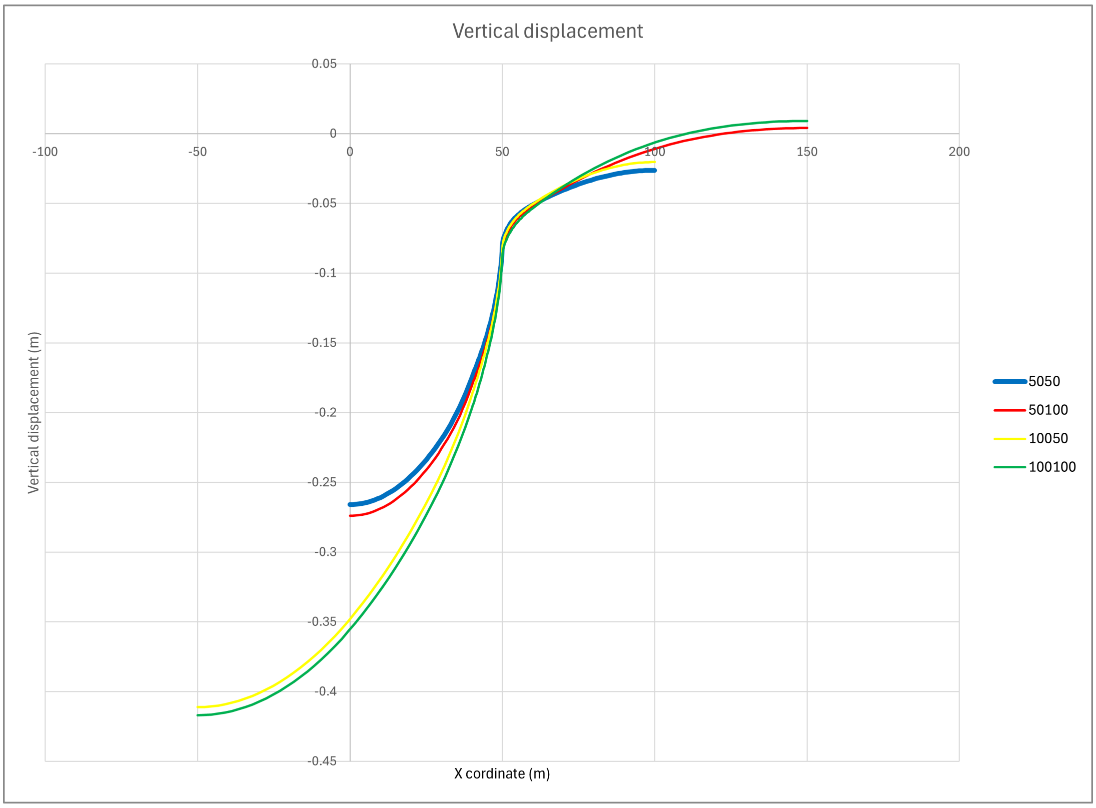

Figure 44: Effect of changing the lateral boundary conditions (Section Y56)

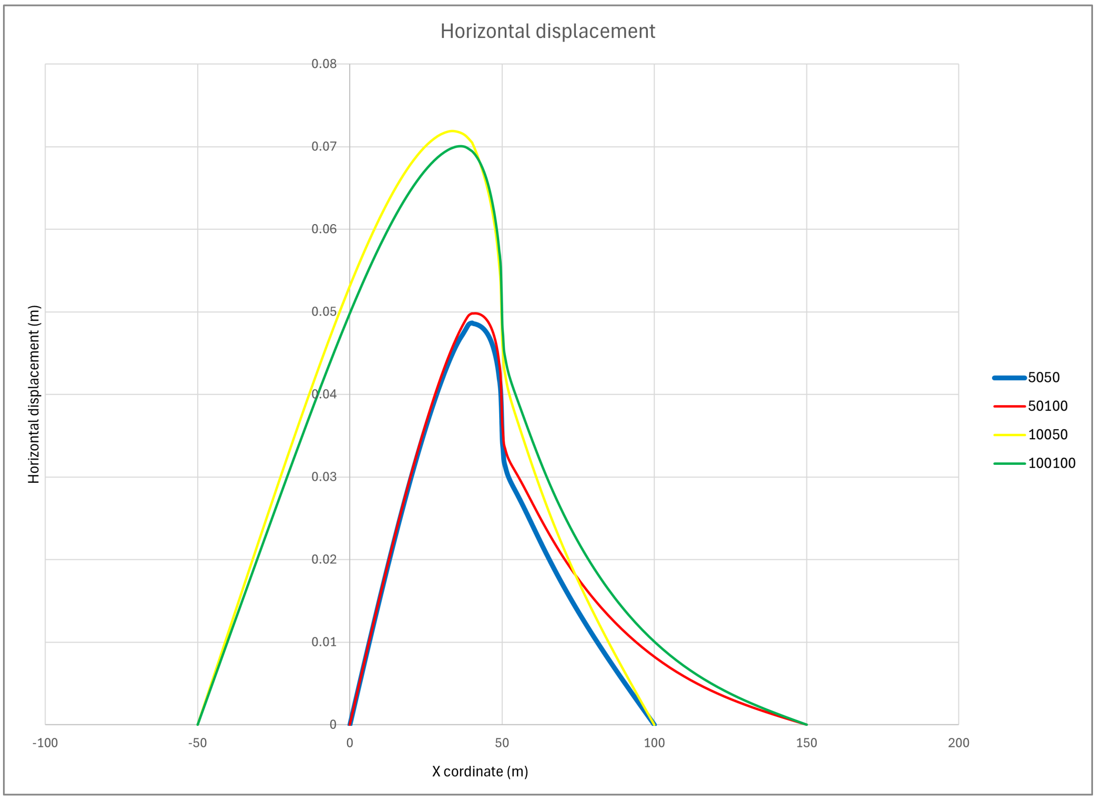

Figure 45: Effect of changing the lateral boundary conditions (Section Y56)

The results illustrated in Figures 44, 45 followed the same pattern but when the width is increased either for the goaf or the seam coal or both of them, we had more displacements in the extended part but in the part studied in the reference model there was not a huge difference.

5.2.3 Effect of changing the depth of the goaf

In this third studied model, we have thought about the effect of having a varied depth of the goaf so, we have considered 3 scenarios, the first one was the reference model depth 50 m which is shallow depth, the second one was 150 m as moderate depth and the last one was a deep goaf with 400 m depth. Taking into the account that the change in the depth affects the stress applied on the top of the goaf too which means having a higher final stress.

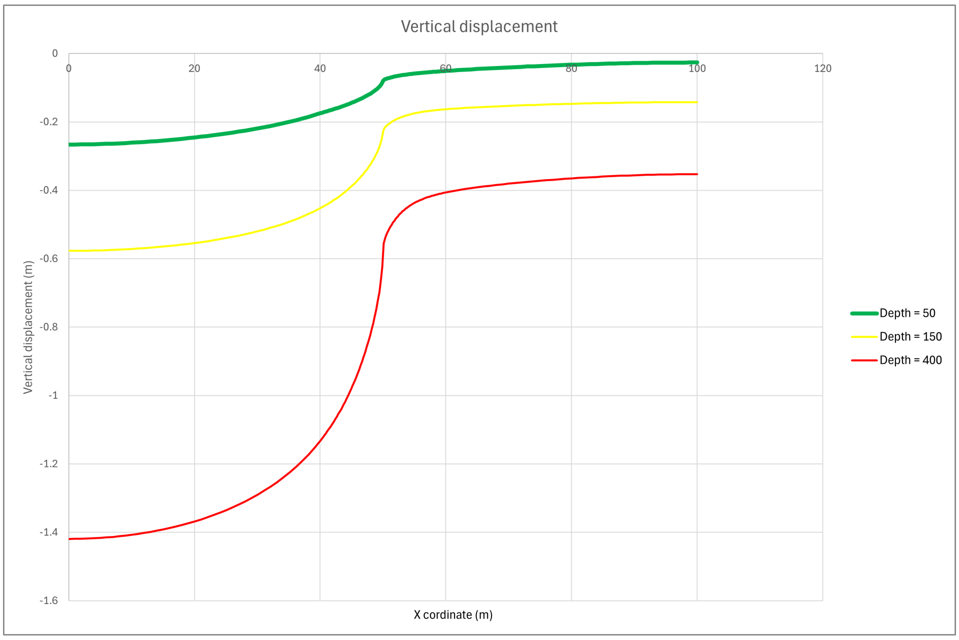

Figure 46: Effect of changing the depths of the goaf (Section Y56)

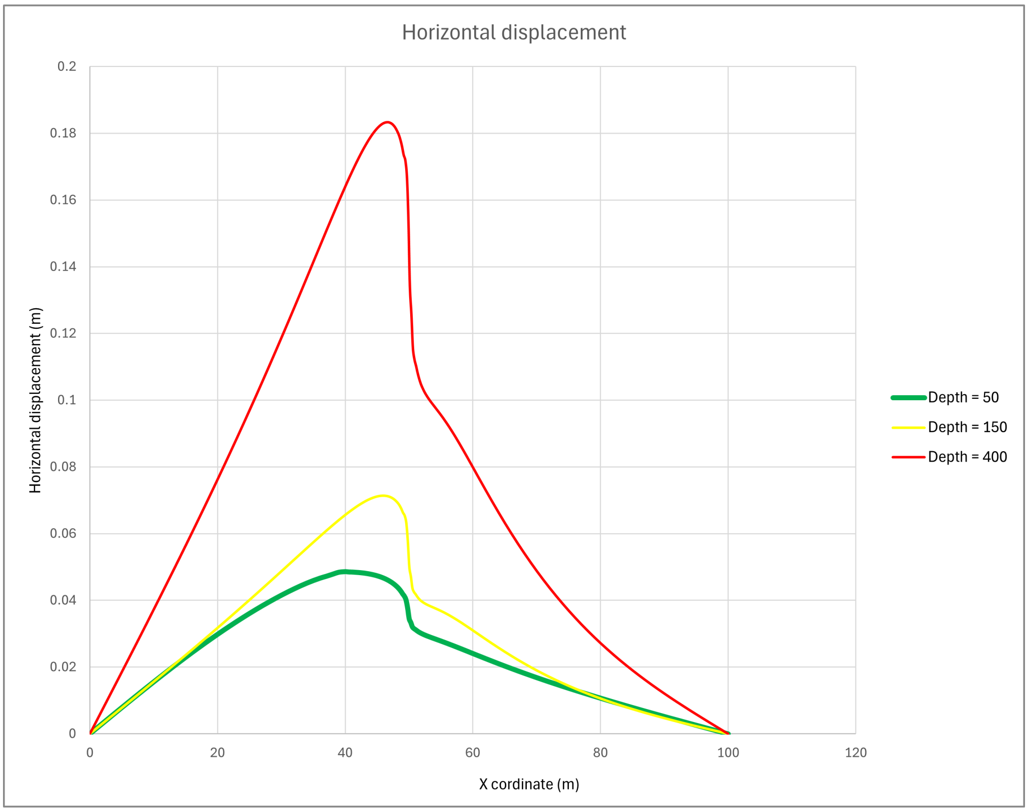

Figure 47: Effect of changing the depths of the goaf (Section Y56)

The outcomes point out in Figures 46, 47 confirms that when the goaf is deeper there will be more compression, which means more displacements and more settlement leading to a significant subsidence, the shallow depth of 50 m exhibit more localized deformation with sharp transitions while for deeper goaf of 400 m it will result a broader subsidence.

5.2.4 Effect of changing the bulking factor b

The bulking factor (b) is a crucial parameter in geomechanical models used for mining or excavation. In the longwall mining method, it plays a key role in how the goaf material compacts and interacts with the overburden. The bulking factor helps determine how much the volume of the material increases after it is displaced, which affects the goaf's interaction with the surrounding strata. Essentially, the bulking factor is used to compare the volume of the goaf material in its displaced state to its original in-situ volume, providing insight into the in-situ density of the material after excavation. We varied the bulking factor b from a low value 1.3 to high value 1.7, which affected the goaf height, as well as the Young's modulus (eq 32), shear modulus, and bulk modulus of the goaf, while keeping the Poisson's ratio constant at $\nu = 0.31$.

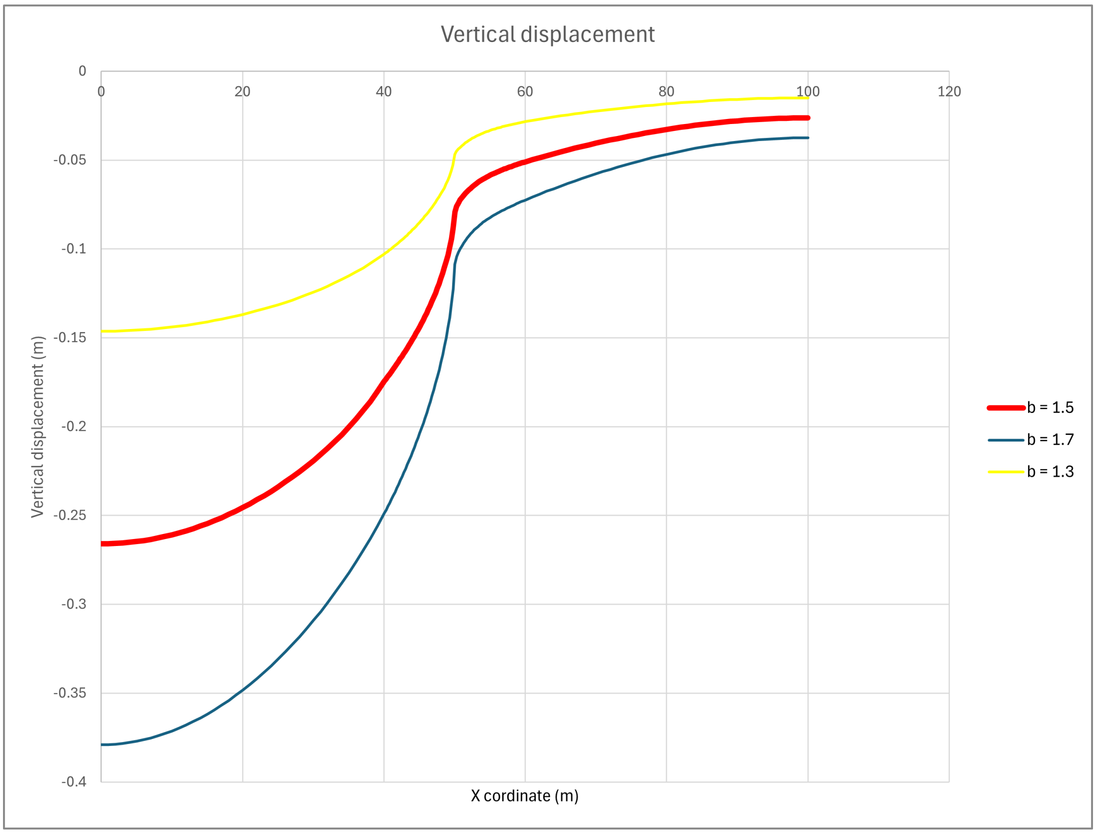

Figure 48: Effect of changing the bulking factor b (Section Y56)

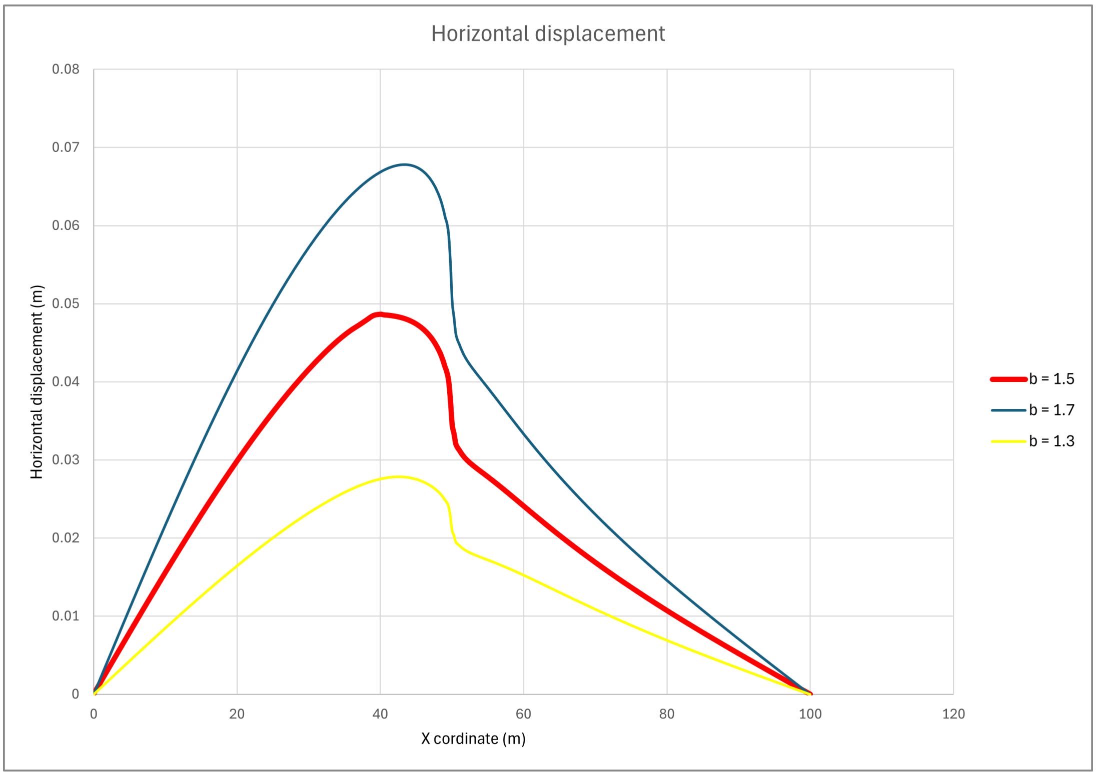

Figure 49: Effect of changing the bulking factor b (Section Y56)

With an increase in the bulking factor b, the vertical displacements generally decrease, and the surface subsidence expands. This behavior is linked to the dual influence of b on the goaf: as b increases, the thickness of the goaf decreases (eq 31), which tends to reduce settlement, while the stiffness of the goaf (E) also decreases due to the inverse relationship with b (Equation 32), which would promote greater settlement. These opposing effects suggest that the decrease in stiffness plays a more dominant role, resulting in a more important subsidence profile, for higher value of b. The results, shown in Figures 48 and 49, reveal bigger displacements and an expansion of the affected subsidence area with increasing values of b, reflecting the predominance of the stiffness effect over the thickness effect.

6 Real case study

6.1 Introduction

This experimental site will be developed in Farciennes, Belgium. The objective of this experiment is to characterize the blasted zones in the coal mines in order to study their function in a geothermal storage system, so we will study the mechanical and geotechnical behavior of materials (displacements, stresses) and we will focus on the hydraulic properties (permeability and porosity). The Figures 50, 51 illustrate where the goafs have been excavated.

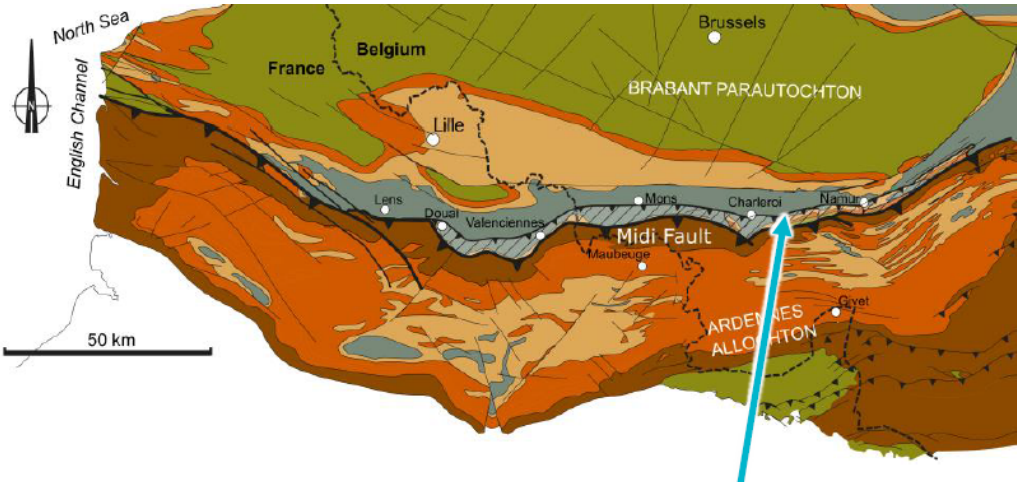

Figure 50: Real case place

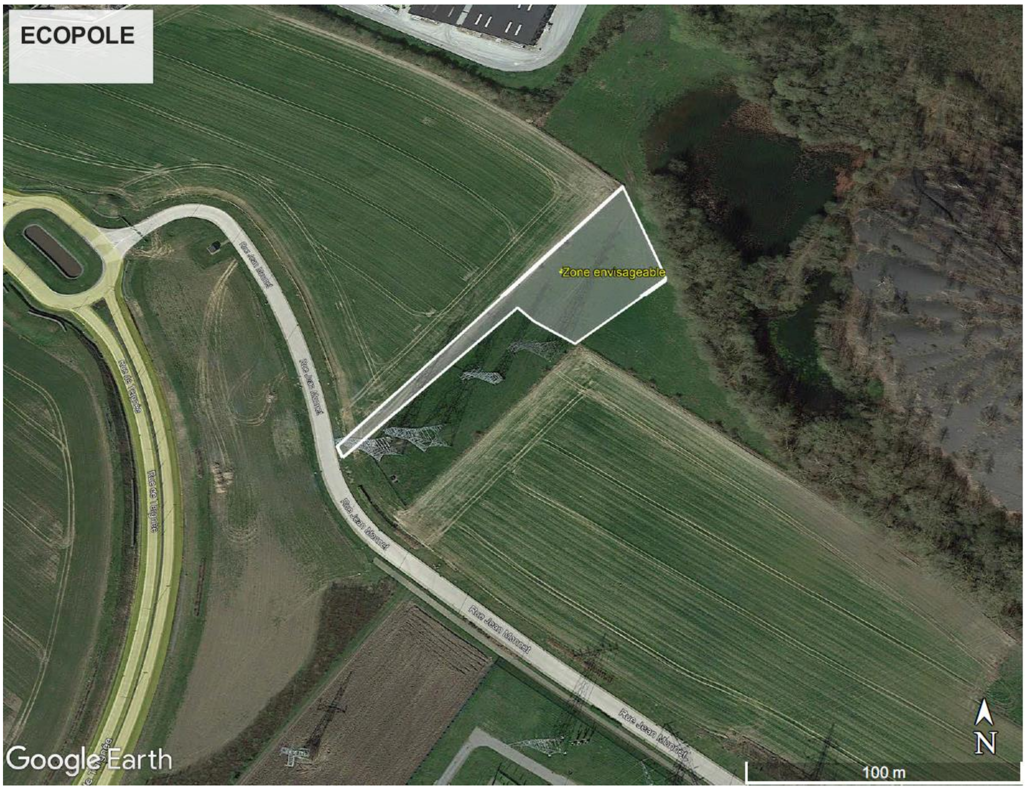

Figure 51: Real case Google Earth view

The site has 3 goafs, which they were excavated at different times. Each of the goafs was at a different depth too.
The figure 52 is a cross-section in the area that shows where is the studied case located and show their depths.

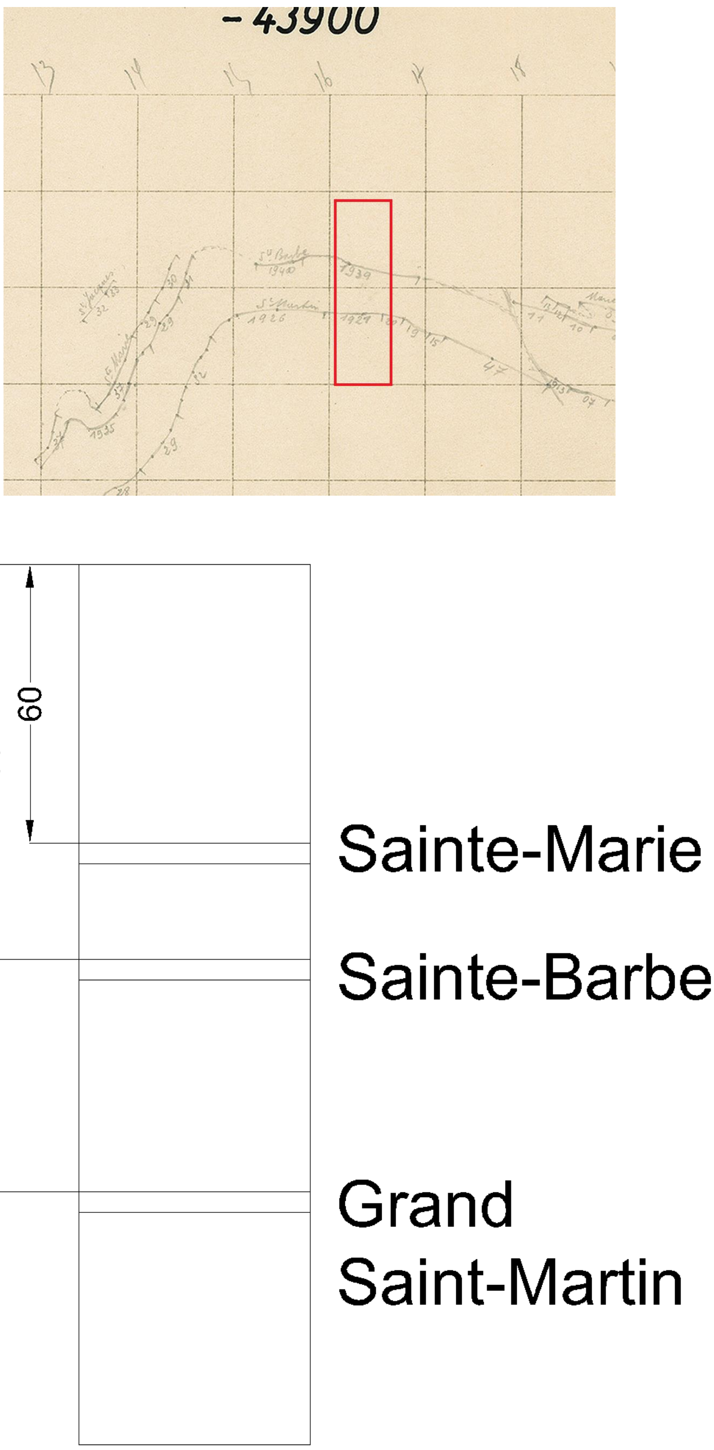

Figure 52: A cross-section in the goafs area

The figures 53a, 53b, 53c represent the layers the 3 goafs that have been excavated.

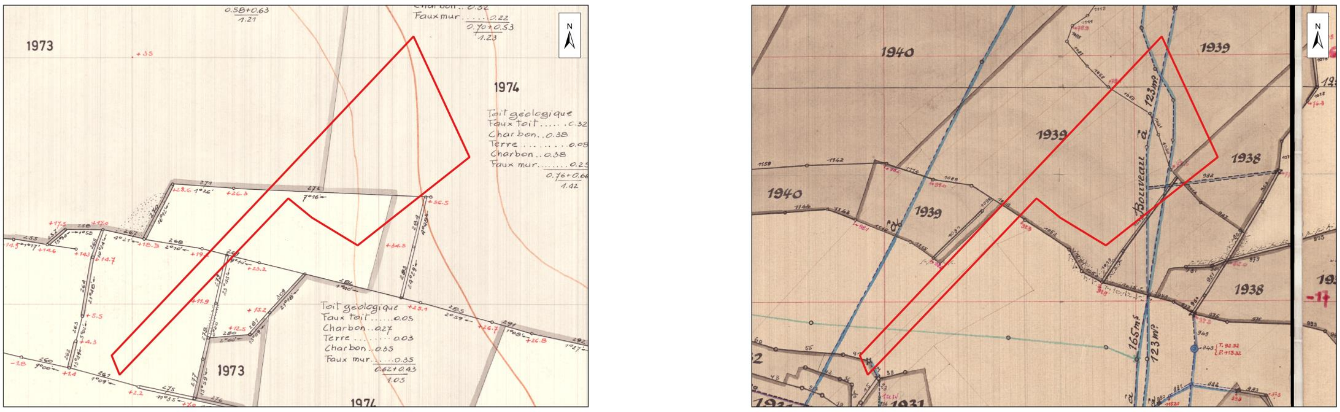

(a) Sainte-Marie layer

(b) Sainte-Barbe layer

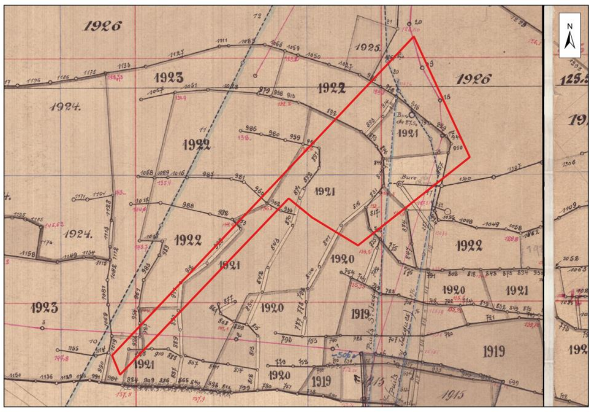

(c) Grand-Saint-Martin layer

Figure 53: The layers of each goaf

6.2 Numerical analysis

6.2.1 Model setup and parameters

The modelisation of this real case was done using LAGAmine software, and following the same procedure previously used. The case was modeled as a 1D rectangular problem 189.5*1 m (as shown in figure 54) because we assume that the horizontal extension of the goaf is very large. Consequently, since we are in the middle of a goaf panel, we can assume that the behaviour is not affected by the goaf edge. So, it is such as if the horizontal extension of the goaf is infinite, the 3 goafs were considered to have the same material properties, and the intact rock between them has the same properties. We have considered that the 3 goafs have the same height, to calculate it, we have used the eq.31, assuming that the bulking factor (b) = 1.5 and the height of coal seam H_{seam} = 1.5, leading to H_{goaf} = 4.5 m.

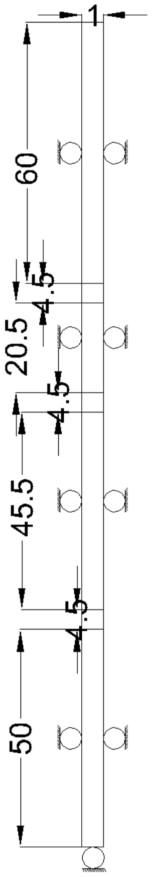

Figure 54: Real case cross section

The initial tangent modulus E_0 for the rock and the goaf was calculated using Eq. 32, with (b) set to 1 for the rock and 1.5 for the goaf as previously mentioned. Since no data for the compressive strength σ_c is available for Farciennes and as we are in the same geological formation of Liège. This formation is called "Houiller" that is a succession of shale, coal and sandstone. We have used the values provided in the geotechnical card of Jupille [4] (Table 4). Assuming the rock was humid, we considered three scenarios: (1) the rock is Schistes argileux, à nodules carbonatés et à radicelles (SRC), (2) the rock is Schsites sableaux homogènes et straticulés (SS), and (3) the rock is Grès schisteux et Schistes très gréseux (Grès, G). We used the Drucker-Prager criterion including the mechanism of plastic compressibility as in Case 6, where Law 1 represents the intact rock properties, and Law 2 represents the goaf properties. Laws 3 to 8 define the loads applied to the edges of the goaf, calculated in the same way mentioned before in Case 4. To determine the bulk modulus (K), we used Eq. 9, and for the shear modulus (G), we used Eq. 7. The Poisson ratio (ν) was assumed to be 0.31, and the plastic compressibility factor (β) was set to 500.
The following table shows the properties used for each case :

	σ_c (MPa)	E_{rock} (MPa)	E_{goaf} (MPa)	ν	K (MPa)	G (MPa)	ρ (kg/m^3)	c (kPa)	ϕ (deg)	β
Case 1 (SRC)	6.8	76.58	3.37	0.31	2.96	1.29	2400	-	30	500
Case 2 (SS)	27.2	324.67	14.31	0.31	12.55	5.46	2400	-	30	500
Case 3 (G)	99.8	1258.08	55.44	0.31	48.63	21.16	2400	-	30	500

Table 2: Parameters used for the real case

6.2.2 Results and discussion

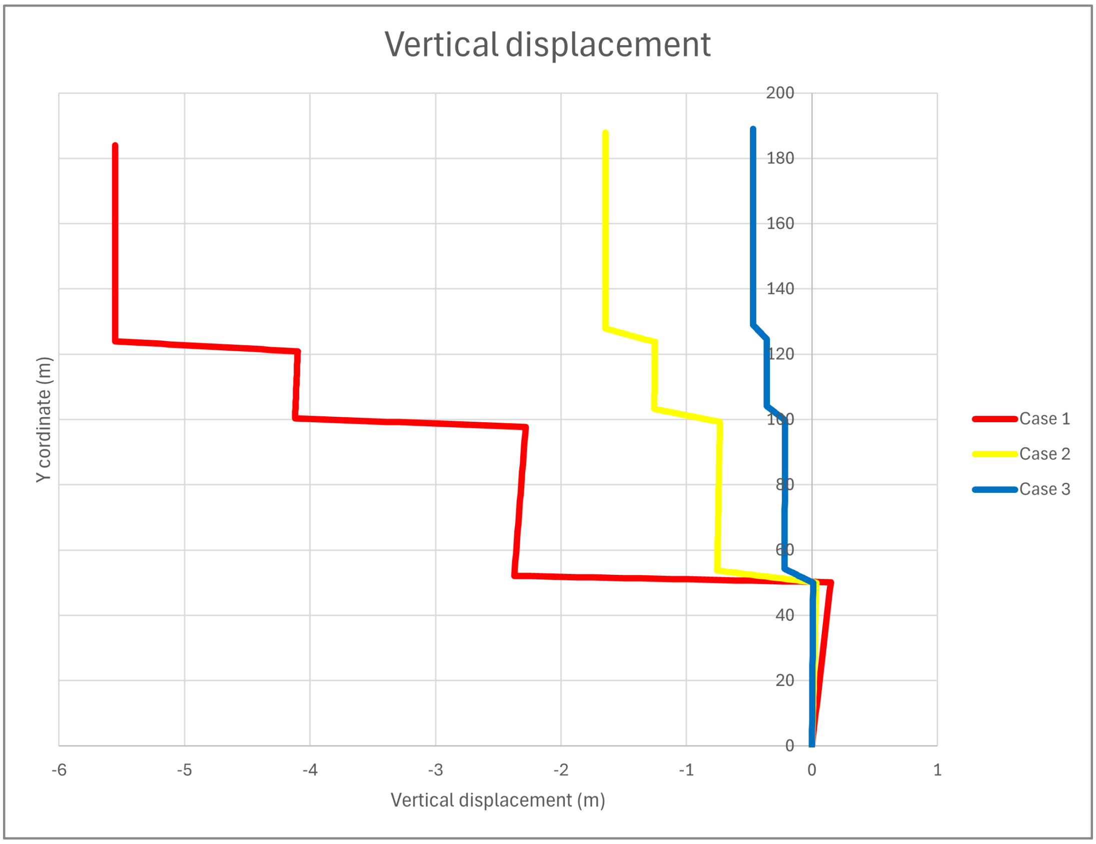

Figure 55: Vertical displacements of real case

As illustrated in Figure 55, it is evident that increasing the compressive strength leads to a reduction in vertical displacements throughout the model. This trend is observed across three different rock types, each displaying distinct behaviors in terms of vertical displacement. The first case, with Schistes argileux, à nodules carbonatés et à radicelles (SRC), exhibits the highest vertical displacements, indicating its lower compressive strength and greater susceptibility to vertical deformation. In contrast, the second case, Schsites sableaux homogènes et straticulés (SS), shows moderate vertical displacements, reflecting its intermediate compressive strength. The third case, with Grès schisteux et Schistes très gréseux (Grès, G), exhibits the lowest vertical displacements, suggesting that it has the highest compressive strength and thus the least vertical deformation. Additionally, closer examination reveals that at the bottom of the model, the intact rock experiences vertical extension under tensile forces, while the goaf region undergoes vertical compressive strain. This contrast emphasizes the varying vertical stress responses of the different rock types, with SRC experiencing the most vertical deformation, and Grès the least, with SS exhibiting intermediate behavior.

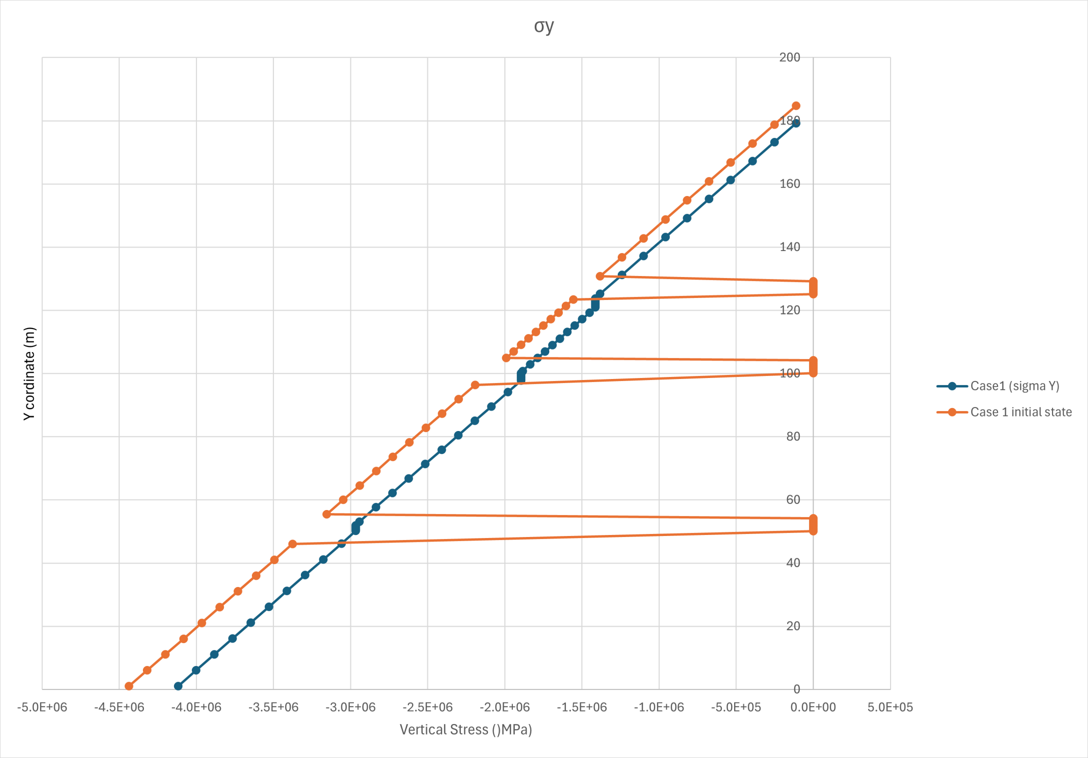

Figure 56: Stresses case 1

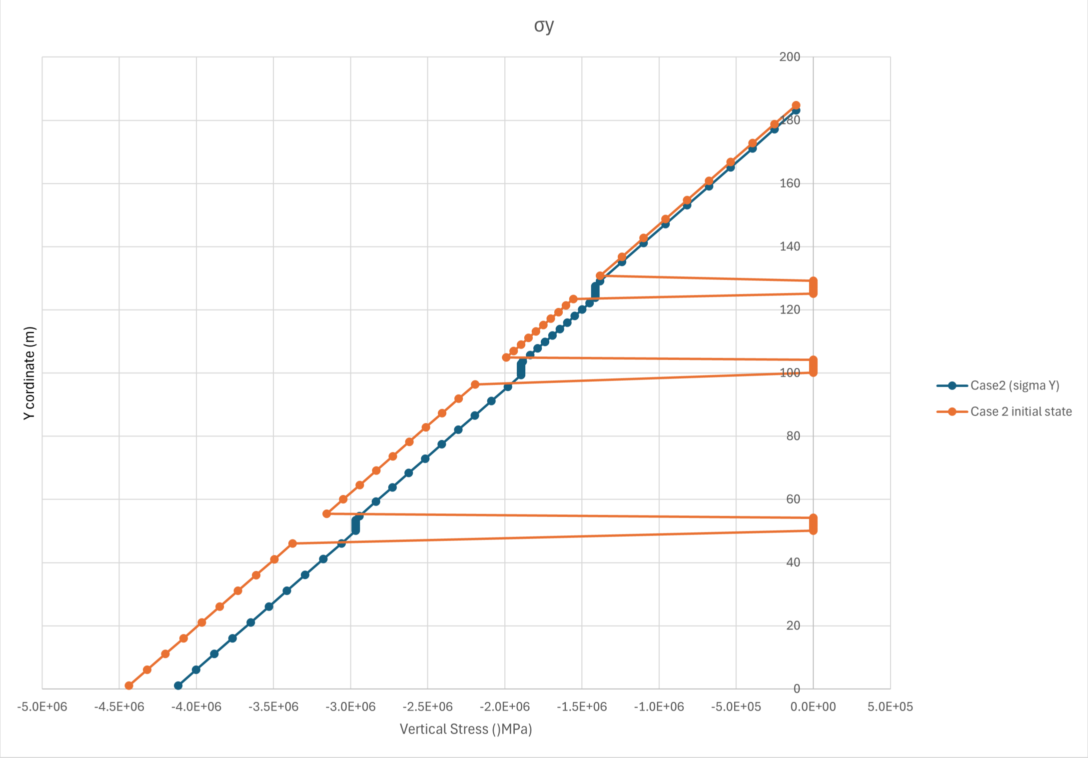

Figure 57: Stresses case 2

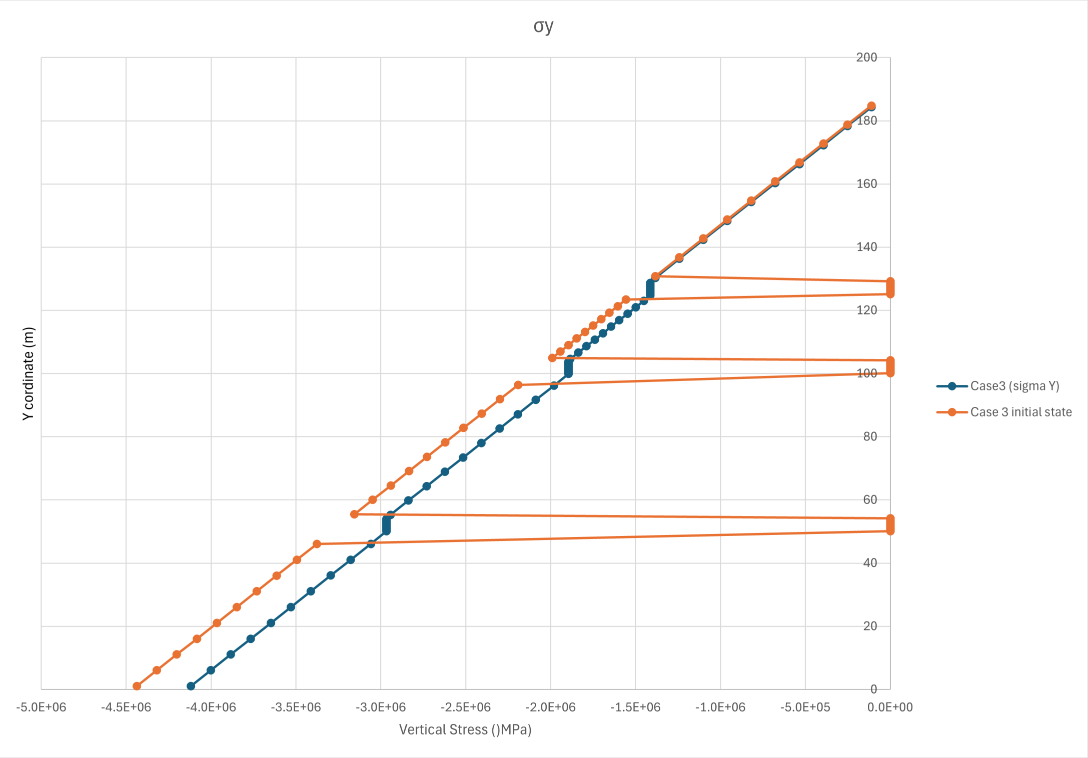

Figure 58: Stresses case 3

As shown in figures 56, 57, 58 the initial stress profile indicates a partial release of stress in the intact rock, while stress increases in the goaf. This explains the observed contraction in the goaf and the extension in the intact rock.

6.3 Studying the permeability and porosity

At the begining we have calculated the porosity :

$$\eta_0 = \frac{V_{voids}}{V_{tot}} = \frac{1.5}{4.5} = \frac{1}{3} \tag{46}$$

Then we have calculated the volumetric strain ε_{vol}

$$\epsilon_{vol} = \frac{\Delta V}{V_0} \tag{47}$$

And

$$\epsilon_{vol} = \frac{\Delta \eta}{1 - \eta_0} \tag{48}$$

From eq 48 we calculate the change in porosity $\Delta\eta$

$$\Delta\eta = \epsilon_{vol}(1 - \eta_0) \tag{49}$$

And finial porosity η_f is :

$$\eta_f = \eta_0 - \Delta_n \tag{50}$$

Where ΔV is the change in the volume, V_0 is the initial volume. And as the model is fixed in the x direction and as well out of plane no stain at all, so the relative volume change ΔV is equal to the thickness change. Then linking between k and η we can derive the permeability following Carman-Kozeny model equation (eq 26).

The following table shows the values calculated :

	η_0	ϵ_{vol}	Δ_η	η_f	Coeff	K
Case 1 (lowest goaf)	$\frac{1}{3}$	0.56	0.373	-	0.083	-
Case 1 (middle goaf)	$\frac{1}{3}$	0.4067	0.271	0.062	0.083	$2.7 \times 10^{-4} K_0$
Case 1 (highest goaf)	$\frac{1}{3}$	0.322	0.215	0.118	0.083	$2.11 \times 10^{-3} K_0$
Case 2 (lowest goaf)	$\frac{1}{3}$	0.1752	0.1168	0.217	0.083	$1.6 \times 10^{-2} K_0$
Case 2 (middle goaf)	$\frac{1}{3}$	0.1178	0.0785	0.255	0.083	$2.9 \times 10^{-2} K_0$
Case 2 (highest goaf)	$\frac{1}{3}$	0.0889	0.0592	0.274	0.083	$3.9 \times 10^{-2} K_0$
Case 3 (lowest goaf)	$\frac{1}{3}$	0.0507	0.0338	0.299	0.083	$5.4 \times 10^{-2} K_0$
Case 3 (middle goaf)	$\frac{1}{3}$	0.0329	0.0219	0.311	0.083	$6.3 \times 10^{-2} K_0$
Case 3 (highest goaf)	$\frac{1}{3}$	0.0244	0.0163	0.317	0.083	$6.8 \times 10^{-2} K_0$

Table 3: Parameters of permeability and porosity

For the fisrst case in the lowest goaf, the change in porosity $Delta\eta$ provides negative value of the final porosity η_f and so it is not realistic because probably that the β coefficient is not constant. Actually, the compressibility decrease with depth and in this case we took a constant to compressibility. And the following figure 59 shows a comparison between the permeability of the 3 cases

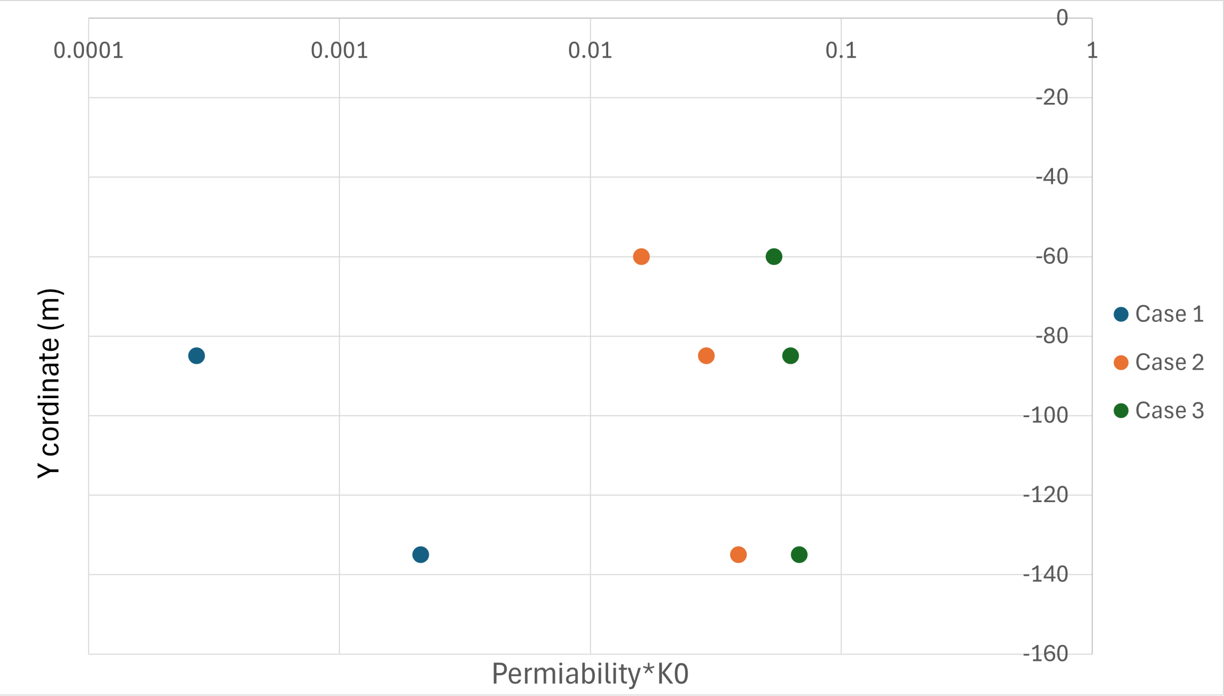

Figure 59: Comparison of the permeability between the 3 cases

As we can see in figure 59, the graph shows that deeper goaf regions exhibit lower permeability (stronger reduction of permeability), which can be attributed to the increased stress and deformation at greater depths, leading to more stress, greater contraction, and closure of the voids, resulting in a reduction of permeability.. Additionally, the permeability also increases with higher compressive strength of the rock, as stronger rocks tend to form more interconnected and stable fracture networks under stress, further facilitating fluid movement.

6.4 Conclusion

After studying this case, we can say that depending on the rock type the vertical displacements can vary from high displacements when we have a ductile material like Schistes argileux, à nodules carbonatés et à radicelles (SRC) to low displacements when we have a brittle material like Grès schisteux et Schistes très gréseux.
Also for porosity and permeability, the ductility of the rock induces more contraction leading to a reduction of porosity and permeability.

7 General conclusion

In conclusion, this study has provided an in-depth exploration of the geomechanical processes that occur during longwall mining, utilizing finite element modeling to simulate the displacement and stress distributions within the rock mass. The findings from these simulations have offered valuable insights into the behavior of the goaf, specifically in terms of its stability and its potential for repurposing as a storage space for geothermal energy. The analysis has shown that the porosity and permeability of the goaf are critical factors that determine its suitability for storing water or gas, which could be used for sustainable energy applications. By integrating these geomechanical factors into the finite element models, this study has significantly advanced our understanding of how the mining process affects the physical properties of the goaf and its potential for secondary use.

The case study conducted at a real mining site in Belgium further validated the findings from the modeling work, providing empirical evidence to support the simulation results. This allowed for a more accurate representation of how geomechanical processes play out in actual mining conditions, offering real-world context to the theoretical models. The research has demonstrated that, with proper understanding and modeling, mined-out areas (goafs) can potentially be transformed into valuable resources for geothermal energy storage, thereby contributing to the sustainability of mining operations and the energy sector as a whole. This innovative approach could play a crucial role in mitigating the environmental impacts of mining by turning the challenges of waste material and void spaces into opportunities for clean energy storage.

The contributions of this work are multifaceted. First, this research has pioneered the application of finite element modeling to assess the geomechanical processes involved in longwall mining, providing a detailed understanding of how displacement, stress, and the physical properties of the goaf interact during mining. Second, it has advanced the concept of utilizing mined-out areas for geothermal energy storage, offering new possibilities for integrating mining operations with renewable energy systems. The ability to predict the behavior of the goaf with precision using finite element models opens the door for utilizing previously mined areas, excavated a long time ago, for future energy storage or extraction. This approach enhances the potential for post-mining land reuse in the context of sustainable energy.

Despite the significant contributions of this study, several limitations remain that should be addressed in future research. The modeling approach, while effective, is based on a simplified set of assumptions that may not fully capture the complexities of real-world mining operations. For instance, the study assumes that all three goaf areas are excavated simultaneously, but future work could explore how the behavior of one goaf may be influenced by the presence of previously excavated goafs. Furthermore, the rock surrounding the goaf, modeled here with an elastic law, may not remain 'intact' as assumed. In reality, this rock likely undergoes fracturing, damage, or at least plastic deformation, and these processes should be incorporated into future models. Additionally, while the goaf was artificially generated based on a bulking factor, a more integrated approach should consider the full transitional behavior between intact rock and the goaf as it develops over time.

Future studies should also expand the range of case studies to include different geological settings and mining conditions, as the results obtained in this research are specific to the Belgian mining site. Moreover, the long-term behavior of the goaf, particularly the effects of thermal and fluid flow dynamics, remains an area that requires further investigation. Understanding how these factors influence the stability and usability of the goaf over time is crucial for evaluating the feasibility of using these areas for long-term geothermal energy storage.

Additionally, while the study has focused on the geomechanical properties of the goaf, it is essential to consider other factors, such as the economic feasibility and environmental impact of converting mined-out areas into geothermal energy storage spaces. Interdisciplinary research will be necessary to assess the full potential of this approach, including the costs, benefits, and environmental implications of such a transition. Advancements in modeling techniques and computational power will allow for more detailed simulations, accounting for long-term behavior and providing more accurate predictions for the use of goafs as energy storage sites.

In summary, this research lays the foundation for future studies that could transform both coal extraction and energy storage practices. By combining geomechanical modeling with innovative energy solutions, this study offers a fresh perspective on how mining operations can contribute to the renewable energy transition. Longwall mining, traditionally seen solely as a method for coal extraction, has the potential to play a pivotal role in sustainable energy solutions. The insights gained from this research will help guide future efforts to optimize mining operations, repurpose mined-out spaces, and integrate geothermal energy systems, ultimately contributing to more sustainable practices in the mining and energy sectors.

A Appendixes

A.1 Displacement and Stress in Case 1

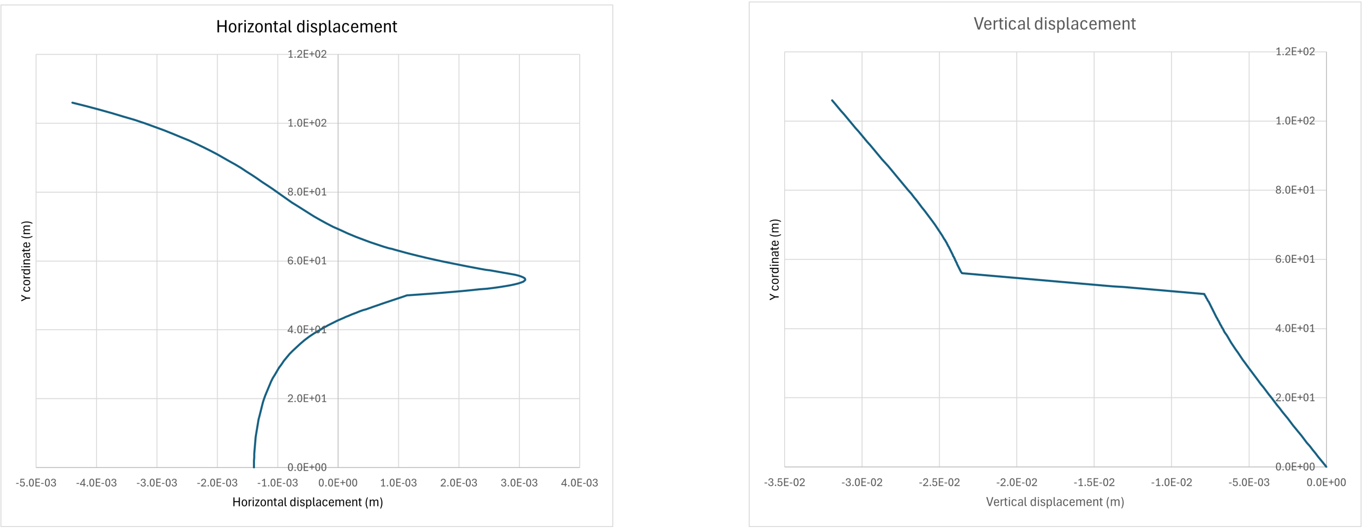

(a) Horizontal Displacement

(b) Vertical Displacement

Figure 60: Displacements Case 1 Section X40

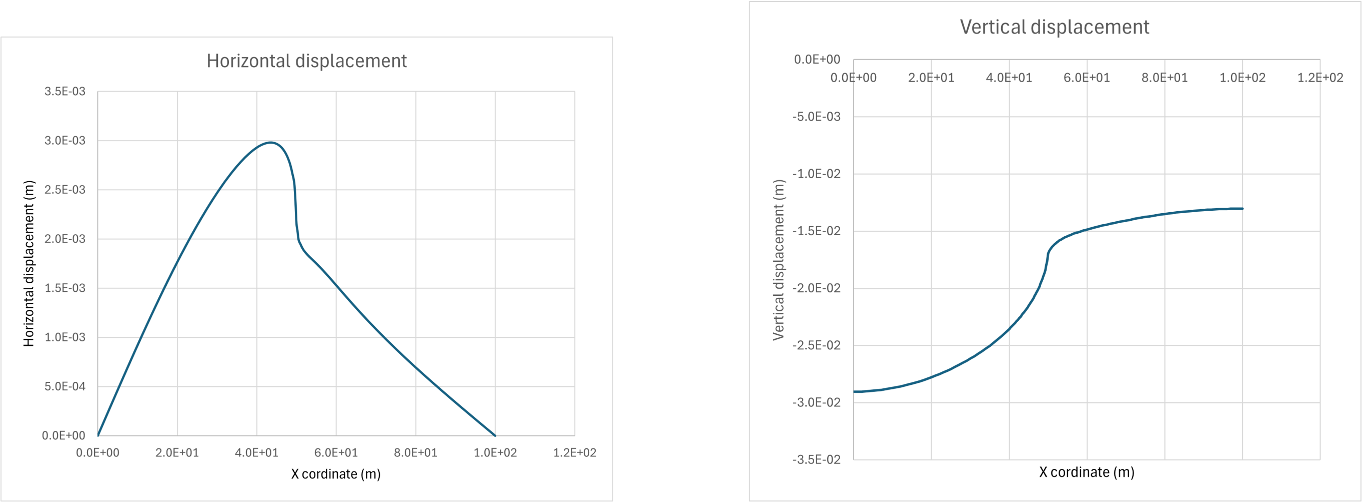

(a) Horizontal Displacement

(b) Vertical Displacement

Figure 61: Displacements Case 1 Section Y56

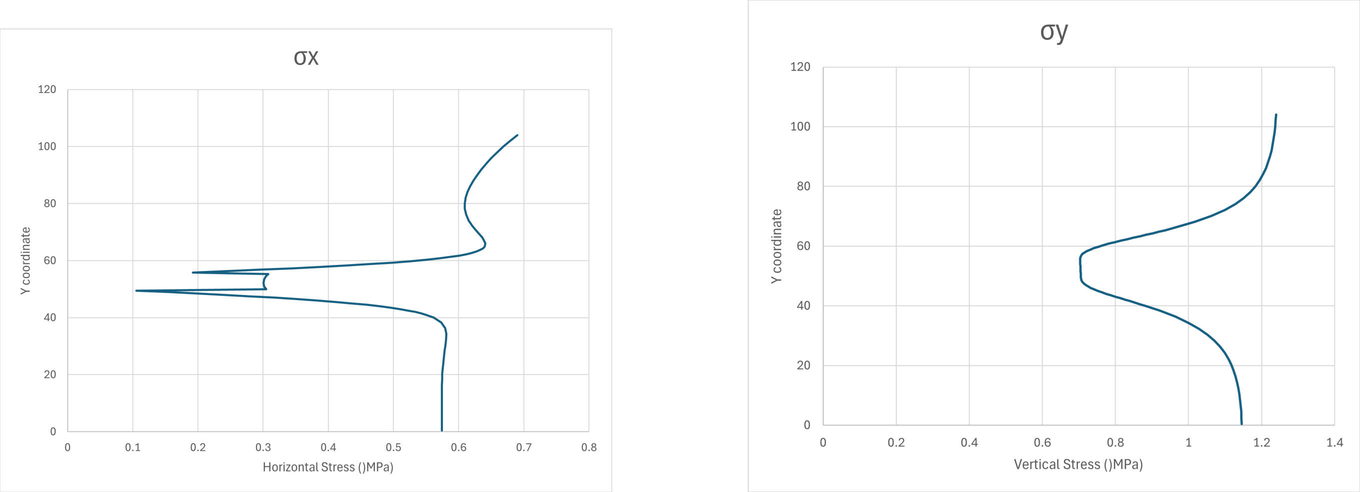

(a) Horizontal Stress

(b) Vertical Stress

Figure 62: Stresses Case 1 Section X40

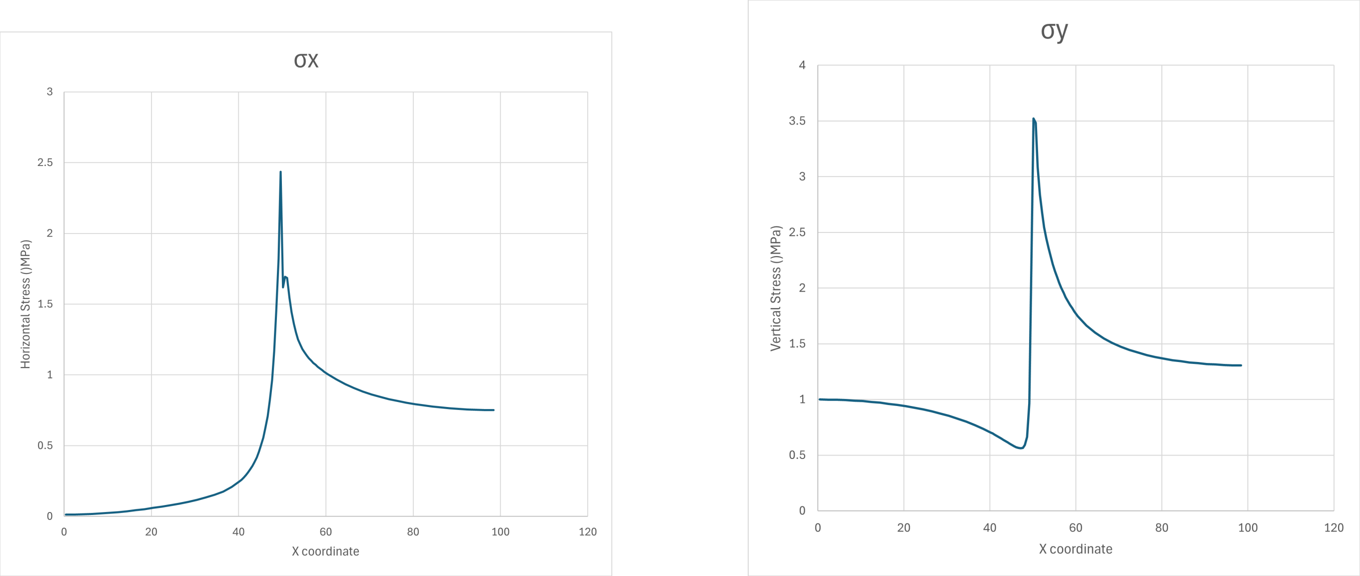

(a) Horizontal Stress

(b) Vertical Stress

Figure 63: Stresses Case 1 Section Y56

A.2 Displacement and Stress in Case 2

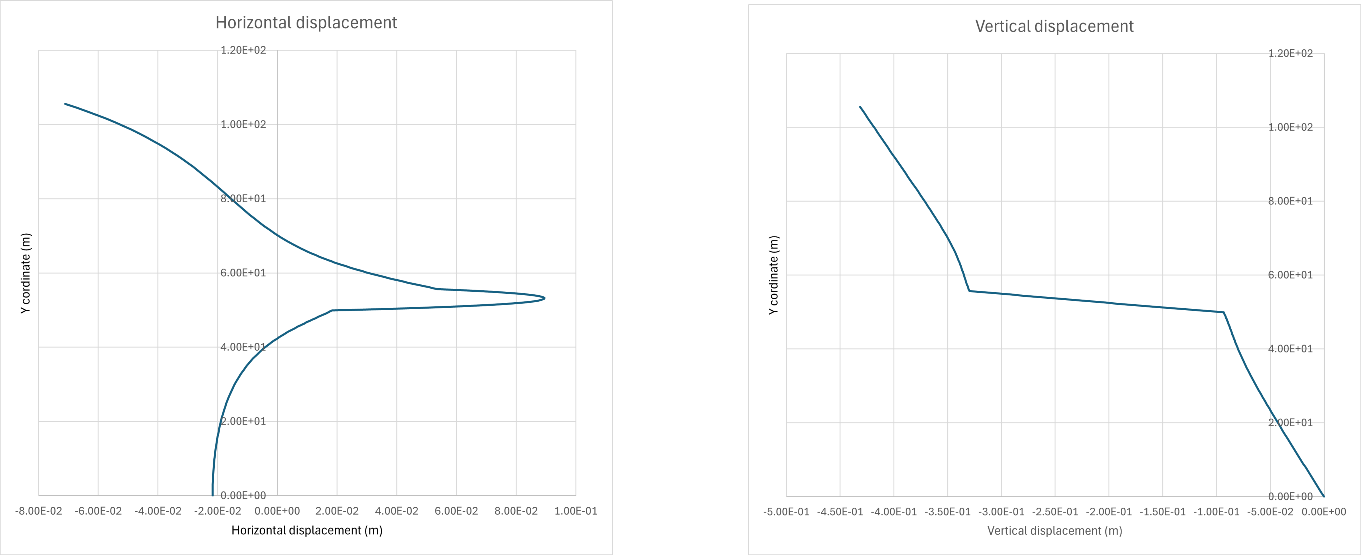

(a) Horizontal Displacement

(b) Vertical Displacement

Figure 64: Displacements Case 2 Section X40

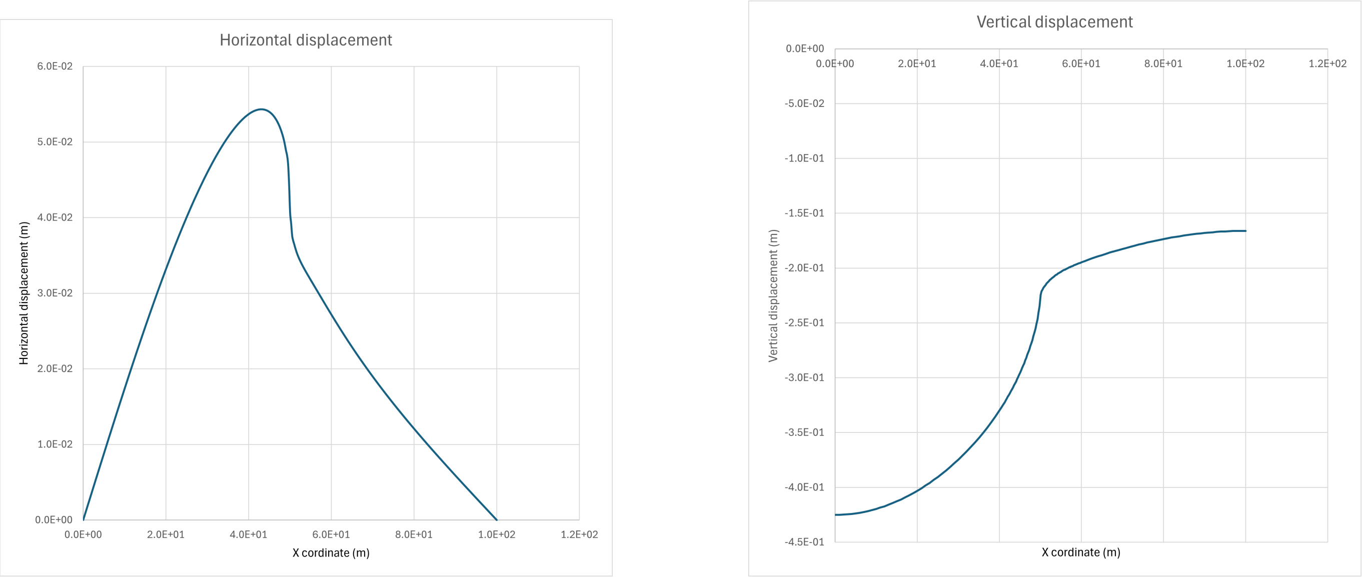

(a) Horizontal Displacement

(b) Vertical Displacement

Figure 65: Displacements Case 2 Section Y56

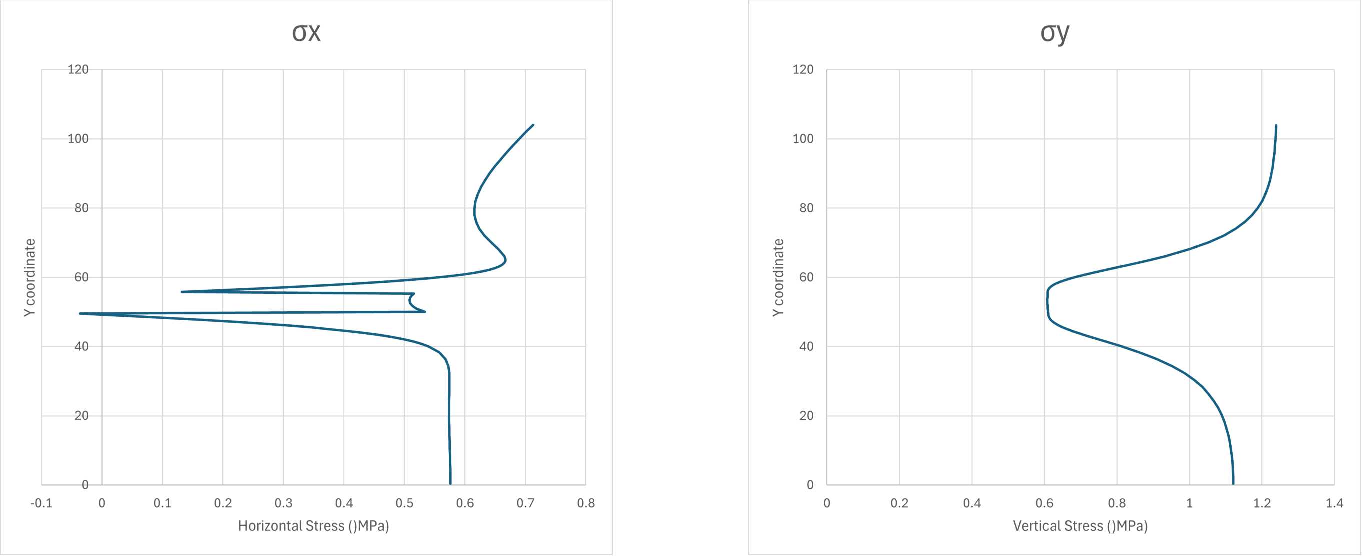

(a) Horizontal Stress (b) Vertical Stress

Figure 66: Stresses Case 2 Section X40

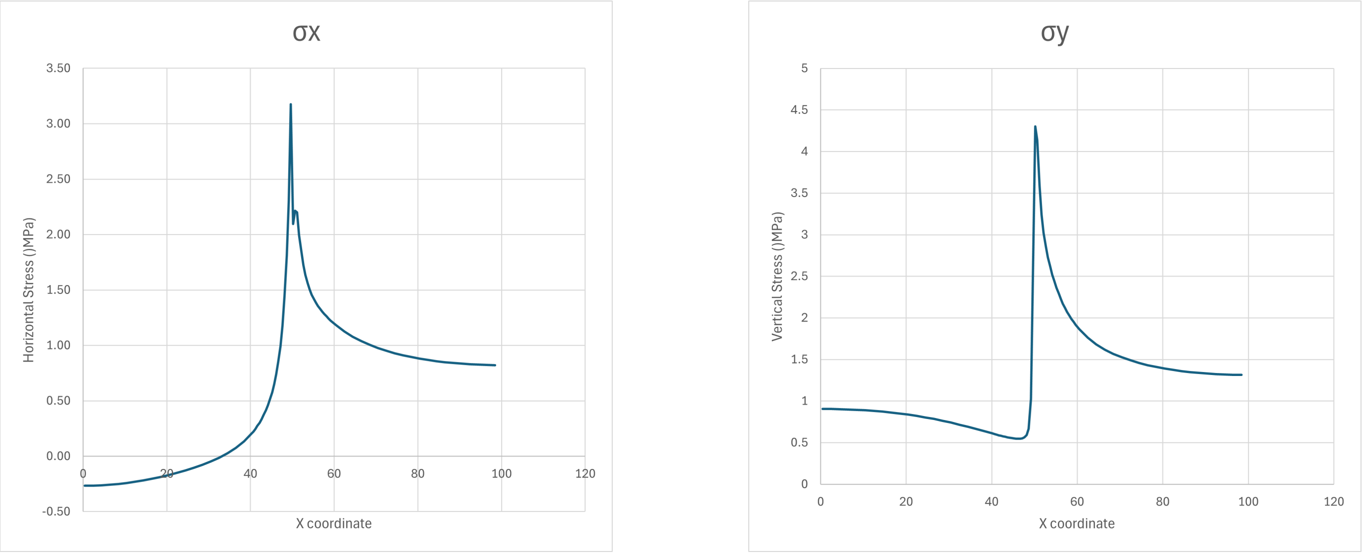

(a) Horizontal Stress (b) Vertical Stress

Figure 67: Stresses Case 2 Section Y56

A.3 Displacement and Stress in Case 3

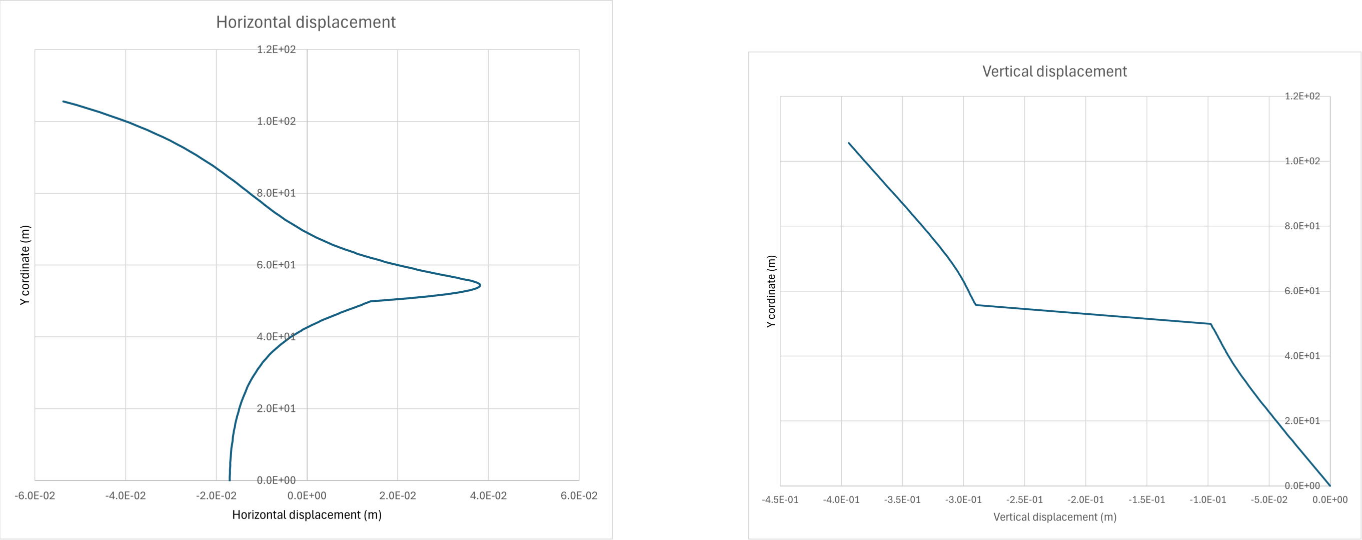

(a) Horizontal Displacement

(b) Vertical Displacement

Figure 68: Displacements Case 3 Section X40

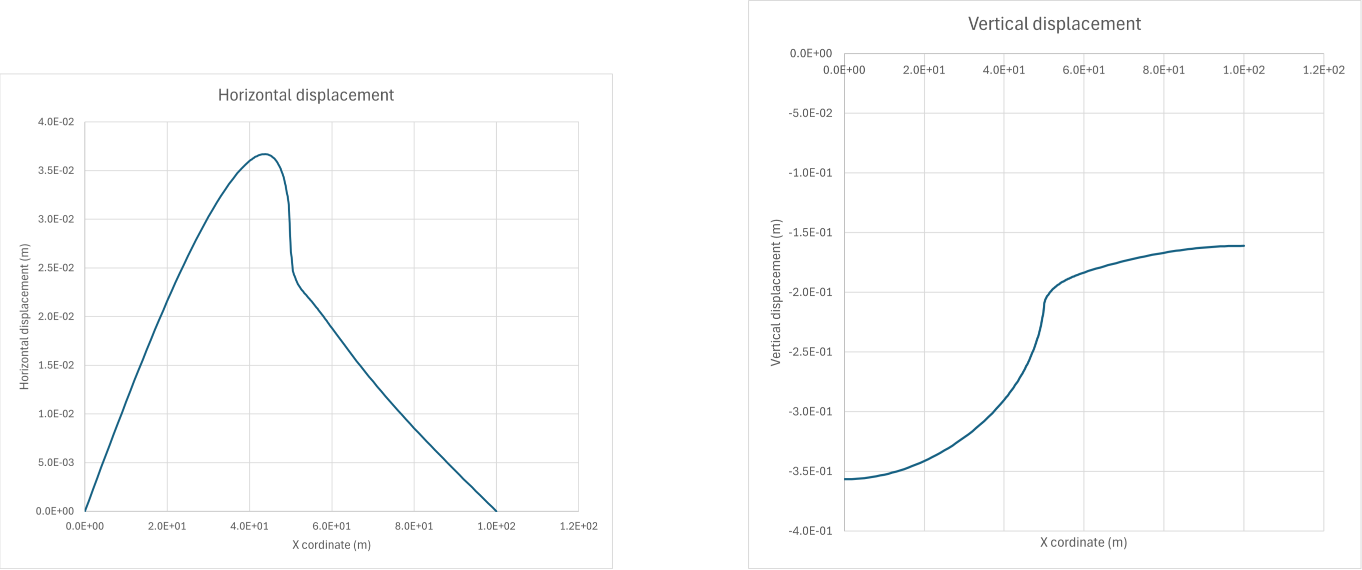

(a) Horizontal Displacement

(b) Vertical Displacement

Figure 69: Displacements Case 3 Section Y56

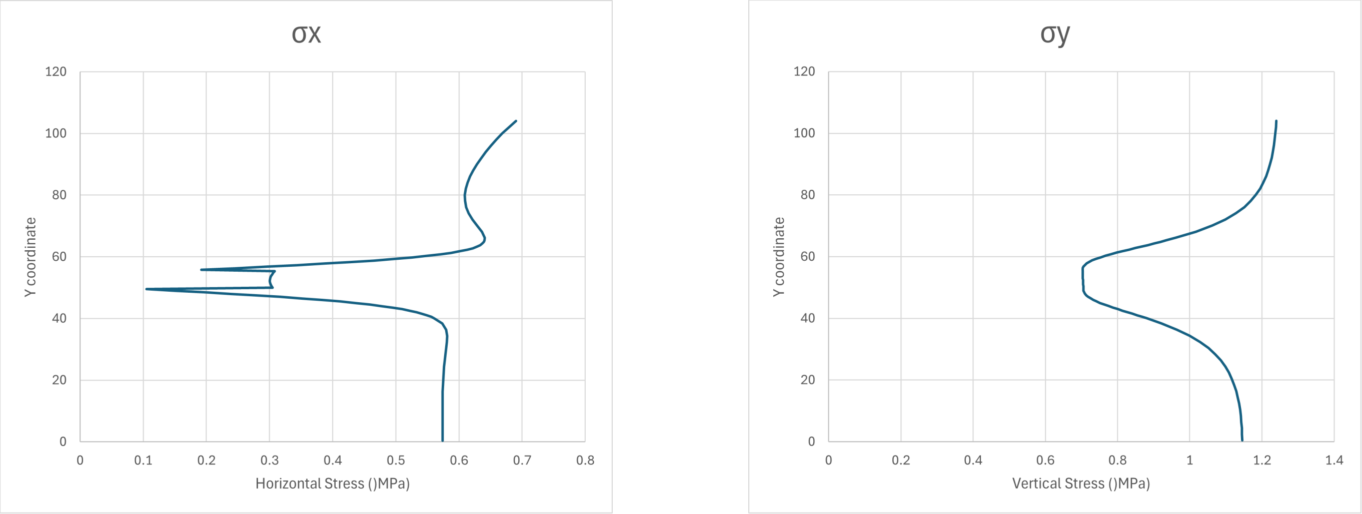

(a) Horizontal Stress (b) Vertical Stress

Figure 70: Stresses Case 3 Section X40

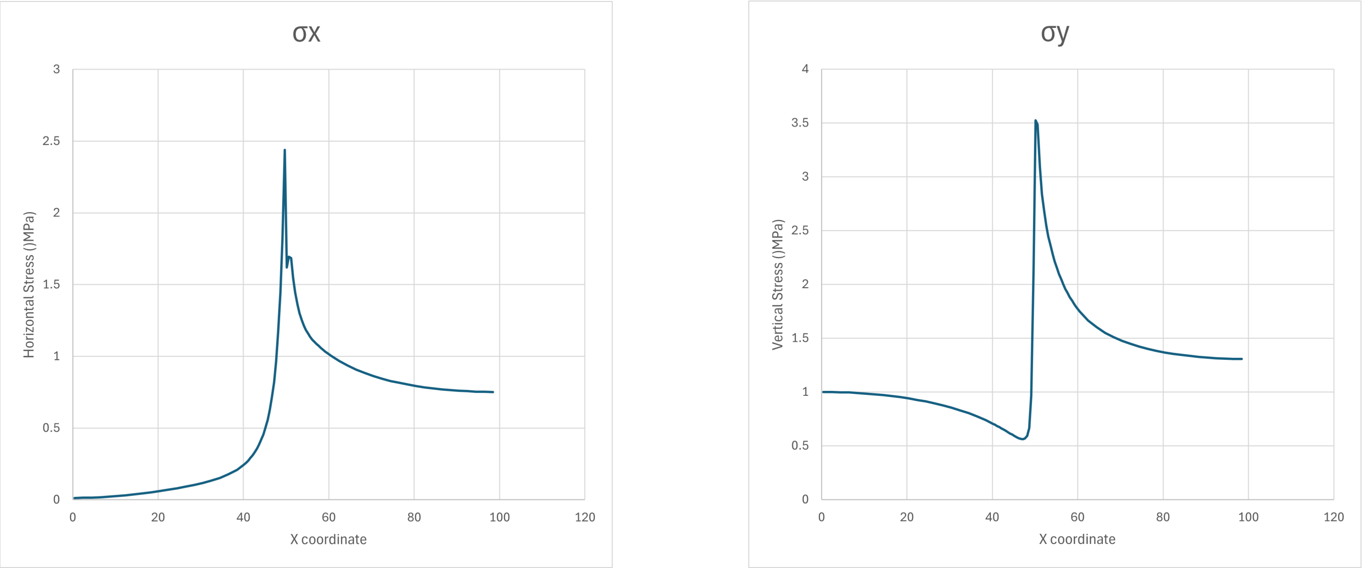

(a) Horizontal Stress (b) Vertical Stress

Figure 71: Stresses Case 3 Section Y56

A.4 Displacement and Stress in Case 4

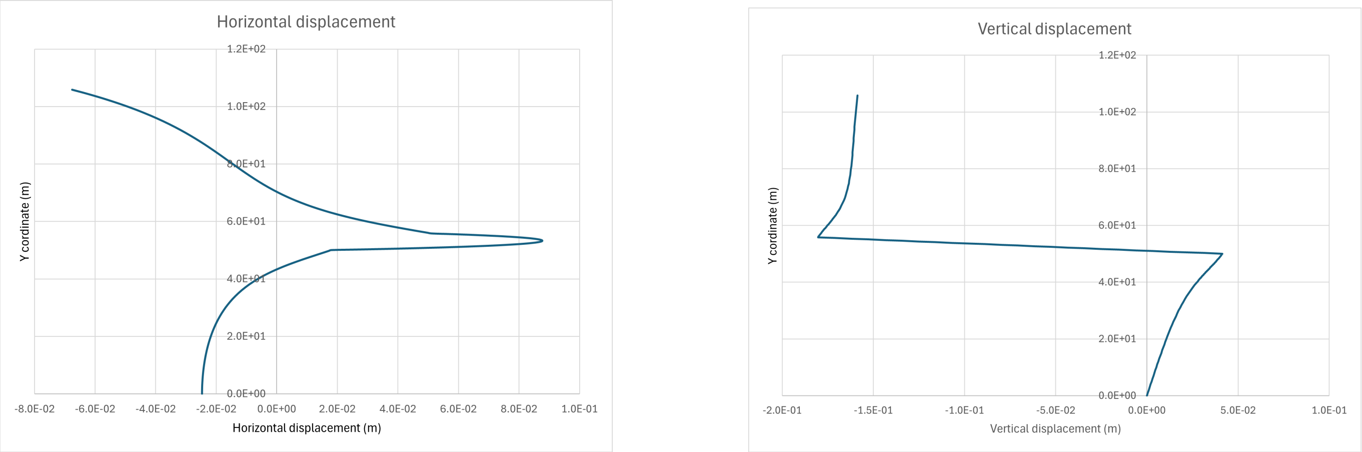

(a) Horizontal Displacement

(b) Vertical Displacement

Figure 72: Displacements Case 4 Section X40

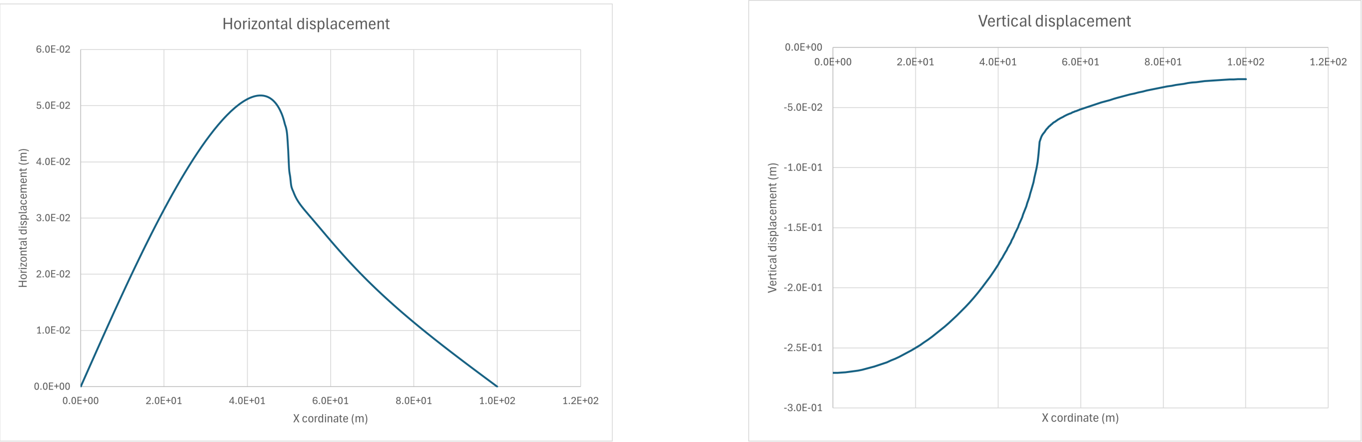

(a) Horizontal Displacement

(b) Vertical Displacement

Figure 73: Displacements Case 4 Section Y56

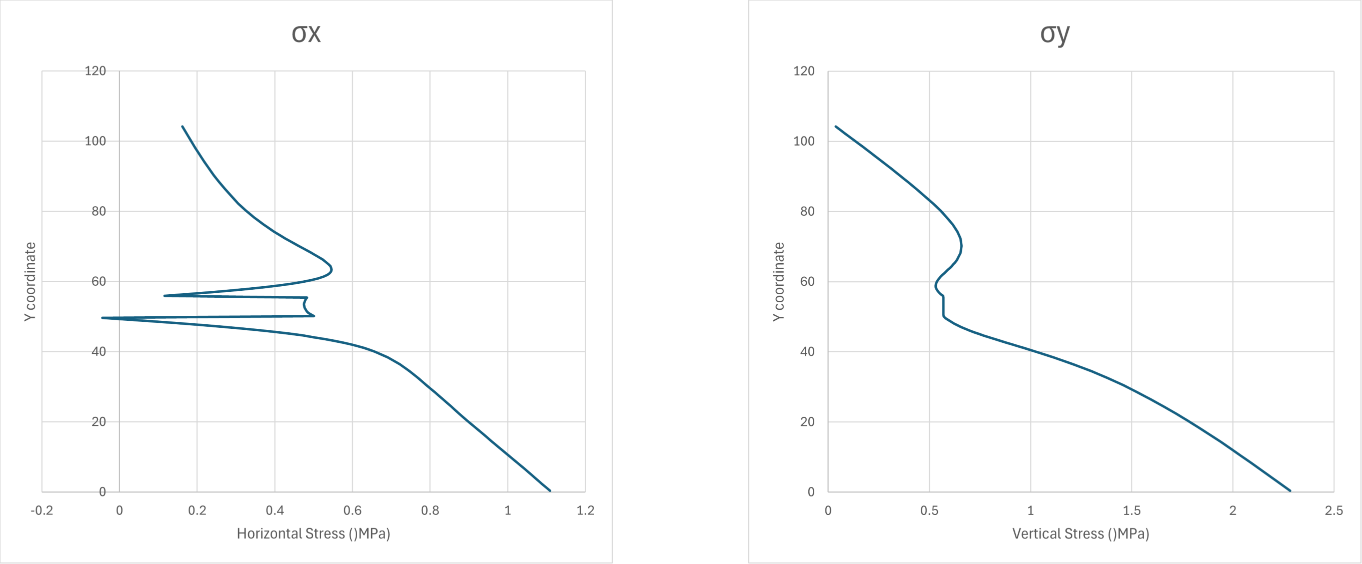

(a) Horizontal Stress (b) Vertical Stress

Figure 74: Stresses Case 4 Section X40

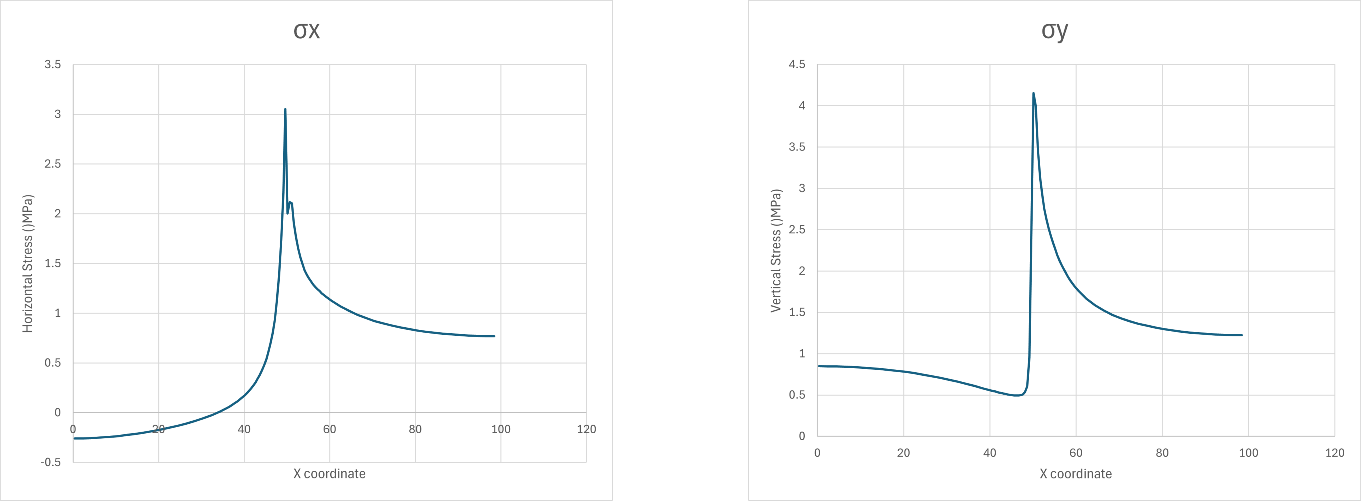

(a) Horizontal Stress (b) Vertical Stress

Figure 75: Stresses Case 4 Section Y56

A.5 Displacement and Stress in Case 5

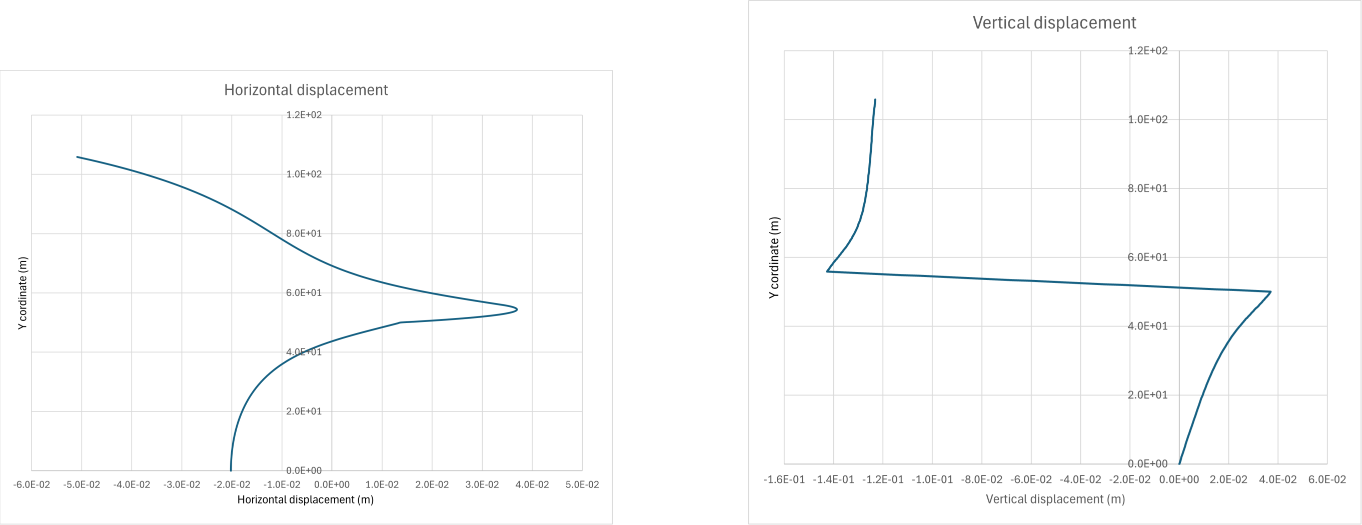

(a) Horizontal Displacement

(b) Vertical Displacement

Figure 76: Displacements Case 5 Section X40

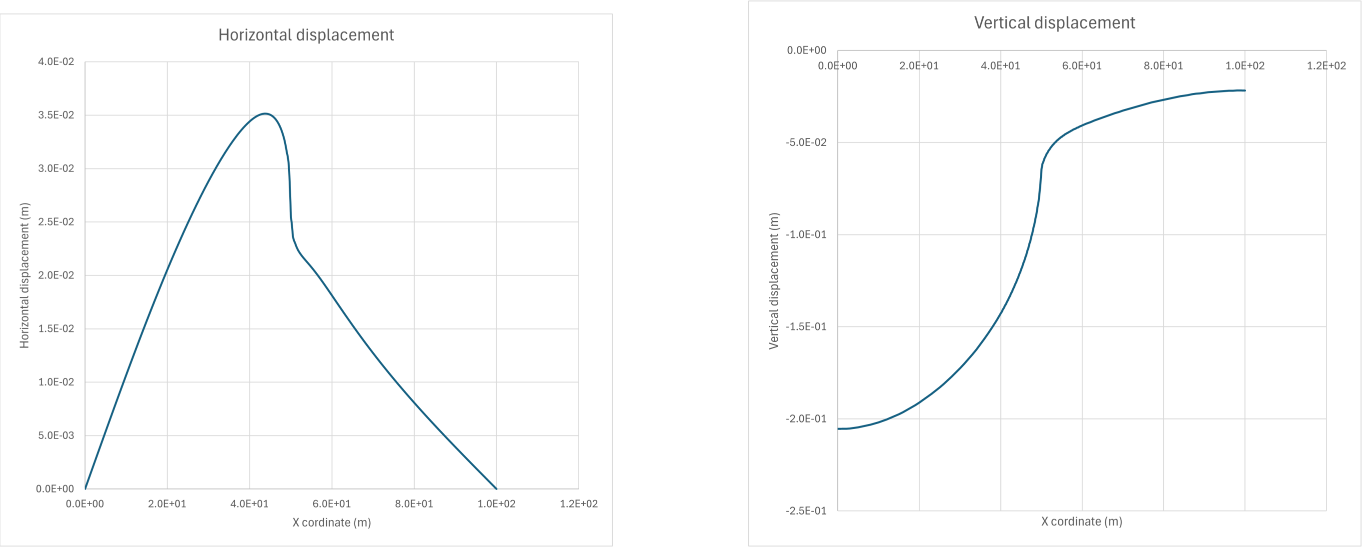

(a) Horizontal Displacement

(b) Vertical Displacement

Figure 77: Displacements Case 5 Section Y56

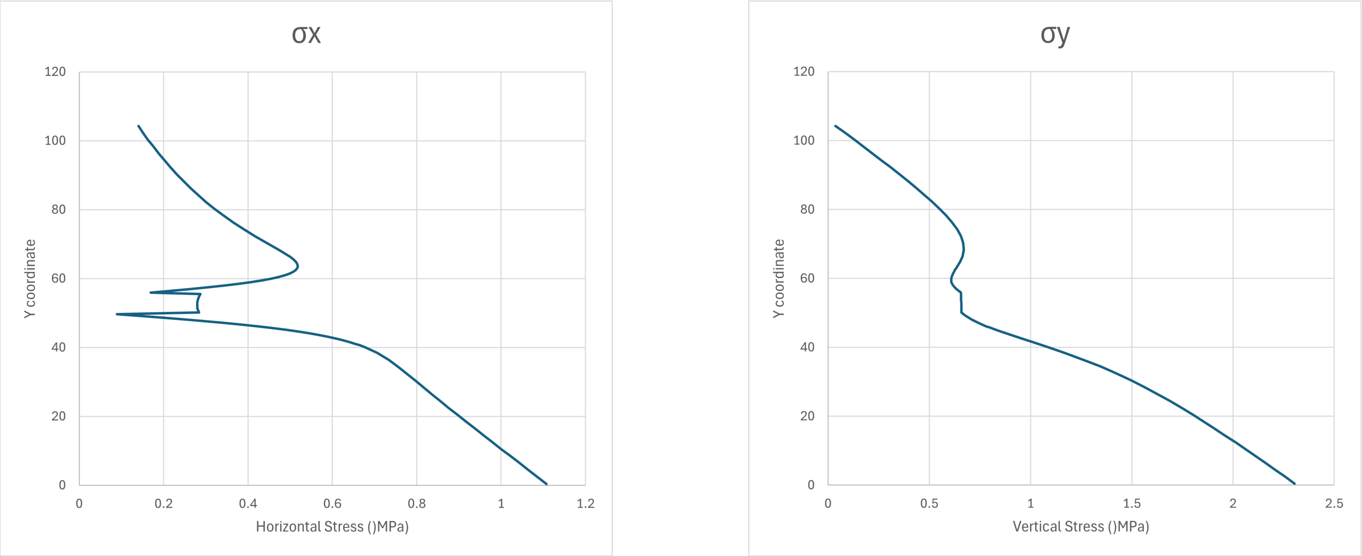

(a) Horizontal Stress

(b) Vertical Stress

Figure 78: Stresses Case 5 Section X40

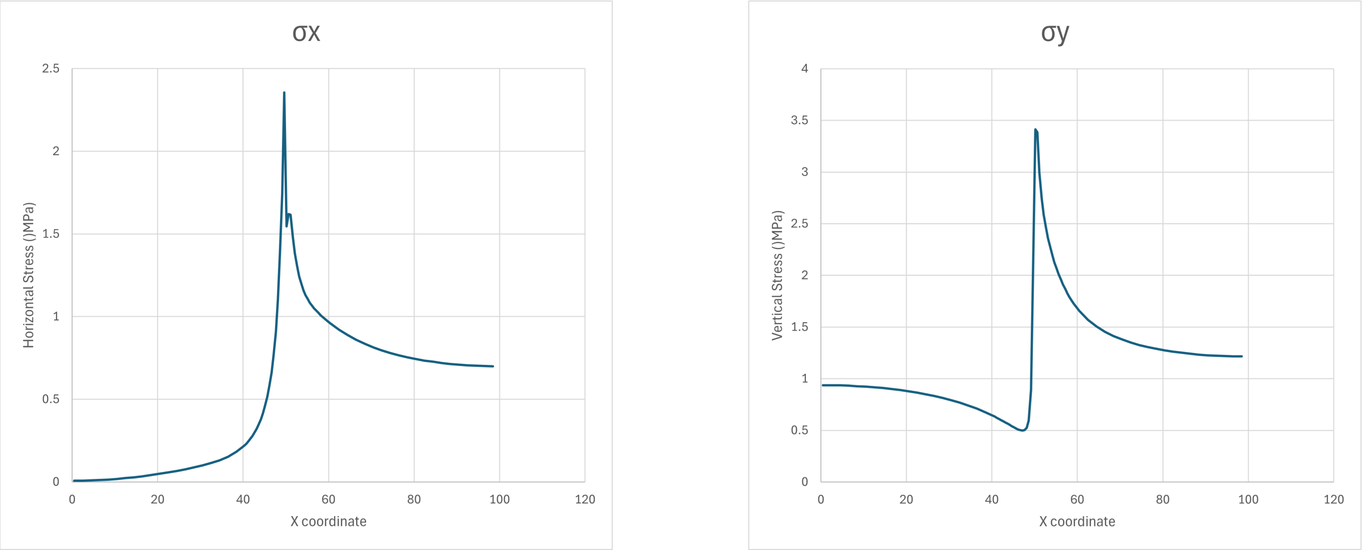

(a) Horizontal Stress

(b) Vertical Stress

Figure 79: Stresses Case 5 Section Y56

List of Figures

List of Tables

References

[1] Arch Coal Inc. (2010). *Annual Report Pursuant To Section 13 Or 15(D) Of The Securities Exchange Act Of 1934, Form 10-K.* United States Securities And Exchange Commission.

[2] B. François (2008) *Thermo-Plasticity of Fine-Grained Soils at Various Saturation States: Application to Nuclear Waste Disposal*, PhD Thesis No. 4188, Ecole Polytechnique Fédérale de Lausanne (EPFL), 2008.

[3] B. N. Whittaker (1974) *An appraisal of strata control practice*, Min. Engr, 134: 9–24.

[4] Carte géotechnique 42-2-8 Jupille, Bonnechere, F., Bolle, A., & Dehard, J. (Université de Liège, Laboratoires d'Infrastructures et de Géomécanique), Monjoie, A., Polo-Chiapolini, C., Barnich, M.-P., & Zeimet, M.-J. (Université de Liège, Laboratoires de Géologie de l'Ingénieur et d'Hydrogéologie).

[5] C. Haycocks, M. Karmis, and B. Ehgartner (1982). *Multiple Seam Mine Design*. In *State-of-the-Art of Ground Control in Longwall Mining and Mine Subsidence*, SME, AIME, pp. 59–65.

[6] Chen, L. F., Zhu, J. G., & Yin, J. H. (2015b). Numerical simulations of mechanical characteristics of coarse-grained soil with different aspect ratios in tri-axial tests. *Journal of Central South University*, 46(7), 2643–2649. *Journal of Central South University*, 46(7), 2643–2649.

[7] Davis, R.O., and Selvadurai, A.P.S. (1996) *Elasticity and Geomechanics.* University of Canterbury, Christchurch, New Zealand; McGill University, Montréal.

[8] Esterhuizen, G. S., & Karacan, C. O. (2005). Development of numerical models to investigate permeability changes and gas emission around longwall mining panel. In *Alaska Rocks 2005, The 40th US symposium on rock mechanics (USRMS).* American Rock Mechanics Association.

[9] G. Bräuner. (1992) *Gebirgsschläge und ihre Verhütung im Ruhrbergbau*, 2nd Edition, Verlag Glückauf GmbH, Essen, 1992.

[10] Guo, H., Adhikary, D. P., & Craig, M. S. (2009). Simulation of mine water inflow and gas emission during longwall mining. *Rock Mechanics and Rock Engineering*, 42(1), 25–51.

[11] Hajal, T. (1984). *Modélisation élasto-plastique des sols par une loi multimécanismes: application au calcul pressiométrique*. PhD Thesis, École Centrale, Paris.

[12] H. Arasteh, G. Saeedi, M. A. Ebrahimi Farsangi, K. Esmaeili (2020) *A New Model for Calculation of the Plastic Compression Index and Porosity and Permeability of Gob Materials in Longwall Mining*, published online on 6 July 2020.

[13] Hujeux, J.C. (1979). *Calcul numérique de problèmes de consolidation élastoplastique*. PhD Thesis, École Centrale, Paris.

[14] Jozefowicz, R. R. (1997). *The post-failure stress-permeability behaviour of coal measure rocks* (Doctoral dissertation, University of Nottingham).

[15] H. Konietzky and C. Lehmann (Editors) (2015) *Geomechanical Issues in Longwall Mining – An Introduction*, July 2015.

[16] *Introduction to the Finite Element Code LAGAMINE.*

[17] M. Juncker, et al.(2006) *Gebirgsbeherrschung von Flözstrecken*, Verlag Glückauf GmbH, Essen, 2006.

[18] M. Kelly, X. Luo, and S. Craig (2002) *Integrating tools for longwall geomechanics*, International Journal of Rock Mechanics and Mining Sciences, 39(5): 661–676.

[19] MESC (2007) *Introduction to longwall mining and subsidence.* Retrieved from www.minesubsidence.com (accessed on 09.07.2015).

[20] Michalski, E., and Rahma, A. (1989). *Modélisation du comportement des sols en élasticité: définition des paramètres des modèles Hujeux-Cyclade et recherche des valeurs des paramètres pour différents sols*. Vol. 1 and 2. Rapport BRGM, 89 SGN 117 GEG.

[21] Pappas, D. M., & Mark, C. (1993). Behavior of simulated longwall gob material (Vol. 9458). U.S. Department of the Interior, Bureau of Mines, pp. 25–27.

[22] P. Konicek, et al.(2011) *Destress Blasting in Coal Mining – State-of-the-Art Review*, Procedia Engineering, Vol. 26, 2011, pp. 179-194.

[23] R.O. Davis and A.P.S. Selvadurai. *Plasticity and Geomechanics.* Cambridge University Press, 2002.

[24] S. Peng, H.S. Chiang (1984) *Longwall Mining*, Wiley, New York, 1984, 708p, ISBN 0471868817.

[25] S. Peng. (2006) *Longwall Mining*, 2nd Ed., Department of Mining Engineering, West Virginia University, Morgantown, 2006, ISBN 9780978938307.

[26] T.M. Barczak (1992) *Examination of Design and Operation Practices for Longwall Shields*, U.S. Department of the Interior, Bureau of Mines, Information Circular, 1992.

[27] Wenzel, A. (2012) *Simulation options for the shield support for longwall coal mining with the software UDEC*, TU Bergakademie Freiberg, Department of Rock Mechanics, Unpublished diploma thesis.

[28] Yavuz, H. (2004). *An estimation method for cover pressure re-establishment distance and pressure distribution in the goaf of longwall coal mines.* International Journal of Rock Mechanics and Mining Sciences, 41, 193–205.